A&A 541, A160 (2012)
DOI: 10.1051/0004-6361/201117825

Astronomy & Astrophysics

Simultaneous *Planck*, *Swift*, and *Fermi* observations of X-ray and γ-ray selected blazars

P. Giommi[2,3], G. Polenta[2,23], A. Lähteenmäki[1,19], D. J. Thompson[5], M. Capalbi[2], S. Cutini[2], D. Gasparrini[2], J. González-Nuevo[43], J. León-Tavares[1], M. López-Caniego[32], M. N. Mazziotta[33], C. Monte[14,33], M. Perri[2], S. Rainò[14,33], G. Tosti[35,15], A. Tramacere[28], F. Verrecchia[2], H. D. Aller[4], M. F. Aller[4], E. Angelakis[41], D. Bastieri[13,34], A. Berdyugin[45], A. Bonaldi[37], L. Bonavera[43,7], C. Burigana[26], D. N. Burrows[10], S. Buson[34], E. Cavazzuti[2], G. Chincarini[46], S. Colafrancesco[23], L. Costamante[47], F. Cuttaia[26], F. D'Ammando[27], G. de Zotti[22,43], M. Frailis[24], L. Fuhrmann[41], S. Galeotta[24], F. Gargano[33], N. Gehrels[5], N. Giglietto[14,33], F. Giordano[14], M. Giroletti[25], E. Keihänen[12], O. King[42], T. P. Krichbaum[41], A. Lasenby[6,38], N. Lavonen[1], C. R. Lawrence[36], C. Leto[2], E. Lindfors[45], N. Mandolesi[26], M. Massardi[22], W. Max-Moerbeck[42], P. F. Michelson[47], M. Mingaliev[44], P. Natoli[16,2,26], I. Nestoras[41], E. Nieppola[1,17], K. Nilsson[17], B. Partridge[18], V. Pavlidou[42], T. J. Pearson[8,29], P. Procopio[26], J. P. Rachen[40], A. Readhead[42], R. Reeves[42], A. Reimer[31,47], R. Reinthal[45], S. Ricciardi[26], J. Richards[42], D. Riquelme[30], J. Saarinen[45], A. Sajina[11], M. Sandri[26], P. Savolainen[1], A. Sievers[30], A. Sillanpää[45], Y. Sotnikova[44], M. Stevenson[42], G. Tagliaferri[21], L. Takalo[45], J. Tammi[1], D. Tavagnacco[24], L. Terenzi[26], L. Toffolatti[9], M. Tornikoski[1], C. Trigilio[20], M. Turunen[1], G. Umana[20], H. Ungerechts[30], F. Villa[26], J. Wu[39], A. Zacchei[24], J. A. Zensus[41], and X. Zhou[39]

(Affiliations can be found after the references)

Received 4 August 2011 / Accepted 31 January 2012

ABSTRACT

We present simultaneous *Planck*, *Swift*, *Fermi*, and ground-based data for 105 blazars belonging to three samples with flux limits in the soft X-ray, hard X-ray, and γ-ray bands, with additional 5 GHz flux-density limits to ensure a good probability of a *Planck* detection. We compare our results to those of a companion paper presenting simultaneous *Planck* and multi-frequency observations of 104 radio-loud northern active galactic nuclei selected at radio frequencies. While we confirm several previous results, our unique data set allows us to demonstrate that the selection method strongly influences the results, producing biases that cannot be ignored. Almost all the BL Lac objects have been detected by the *Fermi* Large Area Telescope (LAT), whereas 30% to 40% of the flat-spectrum radio quasars (FSRQs) in the radio, soft X-ray, and hard X-ray selected samples are still below the γ-ray detection limit even after integrating 27 months of *Fermi*-LAT data. The radio to sub-millimetre spectral slope of blazars is quite flat, with $\langle\alpha\rangle \sim 0$ up to about 70 GHz, above which it steepens to $\langle\alpha\rangle \sim -0.65$. The BL Lacs have significantly flatter spectra than FSRQs at higher frequencies. The distribution of the rest-frame synchrotron peak frequency ($\nu^{\rm S}_{\rm peak}$) in the spectral energy distribution (SED) of FSRQs is the same in *all* the blazar samples with $\langle\nu^{\rm S}_{\rm peak}\rangle = 10^{13.1\pm0.1}$ Hz, while the mean inverse Compton peak frequency, $\langle\nu^{\rm IC}_{\rm peak}\rangle$, ranges from 10^{21} to 10^{22} Hz. The distributions of $\nu^{\rm S}_{\rm peak}$ and $\nu^{\rm IC}_{\rm peak}$ of BL Lacs are much broader and are shifted to higher energies than those of FSRQs; their shapes strongly depend on the selection method. The Compton dominance of blazars, defined as the ratio of the inverse Compton to synchrotron peak luminosities, ranges from less than 0.2 to nearly 100, with only FSRQs reaching values larger than about 3. Its distribution is broad and depends strongly on the selection method, with γ-ray selected blazars peaking at ~7 or more, and radio-selected blazars at values close to 1, thus implying that the common assumption that the blazar power budget is largely dominated by high-energy emission is a selection effect. A comparison of our multi-frequency data with theoretical predictions shows that simple homogeneous SSC models cannot explain the simultaneous SEDs of most of the γ-ray detected blazars in all samples. The SED of the blazars that were not detected by *Fermi*-LAT may instead be consistent with SSC emission. Our data challenge the correlation between bolometric luminosity and $\nu^{\rm S}_{\rm peak}$ predicted by the blazar sequence.

Key words. relativistic processes – BL Lacertae objects: general – quasars: general – galaxies: active

1. Introduction

Blazars are jet-dominated extragalactic objects characterized by the emission of strongly variable and polarized non-thermal radiation across the entire electromagnetic spectrum, from radio waves to γ-rays (e.g., Urry & Padovani 1995). As the extreme properties of these sources are due to the relativistic amplification of radiation emitted along a jet pointing very close to the line of sight (e.g., Blandford & Rees 1978; Urry & Padovani 1995), they are rare compared to both objects pointing their jets at random angles and radio quiet quasi stellar objects (QSOs) where the emitted radiation is due to thermal or reflection mechanisms ultimately powered by accretion onto a supermassive black hole (e.g., Abdo et al. 2010a). Despite that, the strong emission of blazars at all wavelengths makes them the dominant type of extragalactic sources in the radio, microwave, γ-ray, and TeV bands where accretion and other thermal emission processes do not produce significant amounts of radiation (Toffolatti et al. 1998; Giommi & Colafrancesco 2004; Hartman et al. 1999; Abdo et al. 2010a; Costamante & Ghisellini 2002; Colafrancesco & Giommi 2006; Weekes 2008). For these reasons, blazars are hard to distinguish from other sources at optical and X-ray frequencies, while they dominate the microwave and γ-ray sky at high Galactic latitudes. The advent

of the *Fermi* (Atwood et al. 2009) and *Planck*[1] (Tauber et al. 2010; Planck Collaboration 2011a) satellites, which are surveying these two observing windows, combined with the versatility of the *Swift* observatory (Gehrels et al. 2004), is giving us the unprecedented opportunity to collect multi-frequency data for very large samples of blazars and open the way to a potentially much deeper understanding of the physics and demographics of these still puzzling objects.

Blazars can be categorized by their optical properties and the shape of their broad-band spectral energy distributions (SEDs). Blazar SEDs always show two broad bumps in the $\log \nu$ – $\log \nu F_\nu$ space; the lower energy one is usually attributed to synchrotron radiation, while the more energetic one is attributed to inverse Compton scattering. Blazars displaying strong and broad optical emission lines are usually called flat-spectrum radio quasars (FSRQs), while objects with no broad emission lines (i.e., rest-frame equivalent width, EW, <5 Å) are called BL Lac objects. Padovani & Giommi (1995) introduced the terms LBL and HBL to distinguish between BL Lacs with low and high values of the peak frequency of the synchrotron bump ($\nu^{\rm S}_{\rm peak}$). Abdo et al. (2010a) extended this definition to all types of blazars and defined the terms LSP, ISP, and HSP (corresponding to low, intermediate, and high synchrotron peaked blazars) for the cases where $\nu^{\rm S}_{\rm peak} < 10^{14}$ Hz, 10^{14} Hz $< \nu^{\rm S}_{\rm peak} < 10^{15}$ Hz, and $\nu^{\rm S}_{\rm peak} > 10^{15}$ Hz, respectively. In the rest of this paper, we use the LSP/ISP/HSP nomenclature.

It is widely recognized that one of the most effective ways of studying the physics of blazars is through the use of multi-frequency data that is ideally simultaneous. There are several examples of studies following this approach (e.g., Giommi et al. 1995; von Montigny et al. 1995; Sambruna et al. 1996; Fossati et al. 1998; Giommi et al. 2002; Nieppola et al. 2006; Padovani et al. 2006), but in most cases the samples are heterogeneous and the data are sparse and non-simultaneous.

The compilation of simultaneous and well-sampled SEDs requires the organization of complex multi-frequency observation campaigns, involving the coordination of observations from several observatories. Such large efforts have been carried out only rarely, and almost exclusively on the occasion of large flaring events in a few bright and well-known blazars, e.g., 3C 454.3 (Giommi et al. 2006; Abdo et al. 2009a; Vercellone et al. 2009), Mkn 421, (Donnarumma et al. 2009; Abdo et al. 2011), and PKS 2155−304 (Aharonian et al. 2009).

Significant progress has been made with the publication of a compilation of quasi-simultaneous SEDs of a large sample of γ-ray bright blazars (Abdo et al. 2010a). This is an important step forward from previous compilations, as the sample presented is statistically representative of the population of bright γ-ray selected blazars, and the data were quasi-simultaneous, that is collected within three months of the *Fermi*-LAT observations.

With *Planck*, *Swift*, and *Fermi*-LAT simultaneously in orbit, complemented by other space and ground-based observatories, it is now possible to assemble high-quality multi-frequency datasets that allow us to build simultaneous and well-sampled broad-band spectra of large and statistically well-defined samples of active galactic nuclei (AGNs).

[1] *Planck* (http://www.esa.int/Planck) is a project of the European Space Agency – ESA – with instruments provided by two scientific consortia funded by ESA member states (in particular the lead countries: France and Italy) with contributions from NASA (USA), and telescope reflectors provided in a collaboration between ESA and a scientific consortium led and funded by Denmark.

In this and a companion paper (Planck Collaboration 2011e), we present the first results of a large cooperative program between the *Planck*, *Fermi*-LAT, and *Swift* satellites and a number of ground-based observatories, carried out to collect multi-frequency data on large samples of blazars selected using different criteria and observed when the sources lie in the field of view of *Planck*.

In this paper, we concentrate on blazars selected in the soft X-ray, hard X-ray, and γ-ray bands. We present the simultaneous data, test for flux correlations, and estimate some key parameters characterizing the SEDs. We then compare the results obtained for the different samples. Detailed fits to models, variability studies, and more complete theoretical interpretations will be presented elsewhere.

Throughout this paper, we define the radio-to-submillimetre spectral index α by $S(\nu) \propto \nu^{\alpha}$, and we adopt a ΛCDM cosmology with $H_0 = 70\,{\rm km\,s^{-1}\,Mpc^{-1}}$, $\Omega_{\rm m} = 0.27$, and $\Omega_\Lambda = 0.73$ (Komatsu et al. 2011).

2. Sample selection

To explore the blazar parameter space from different viewpoints, we used several different criteria to select the blazars to be observed simultaneously by *Planck*, *Swift*, and *Fermi*. In this paper, we considered three samples of blazars that are flux-limited in the high-energy part of the electromagnetic spectrum: soft X-ray (0.1–2.4 keV) sources from the ROSAT All-Sky Survey Bright Source Catalog (1RXS, Voges et al. 1999, hereafter RASS sample), hard X-ray (15–150 keV) sources from the *Swift*-BAT 54-month source catalog (Cusumano et al. 2010, hereafter BAT sample), and γ-ray sources from the *Fermi*-LAT 3-month bright AGN source list (Abdo et al. 2009b, hereafter *Fermi*-LAT sample).

These high-energy-selected samples were complemented by a radio flux-limited sample of northern sources (hereafter radio sample), which is presented in the companion paper (Planck Collaboration 2011e). We used these four samples, defined in widely different parts of the electromagnetic spectrum, to try to disentangle the intrinsic properties of blazars from the heavy selection effects that often afflict blazar samples. In total we considered 175 sources.

We based our classification of different blazar types on the Roma-BZCAT catalog (Massaro et al. 2010), which is a compilation of known blazars that were carefully checked to determine their blazar type in a uniform and reliable way. Massaro et al. (2010) divided blazars into three categories: BZQ/FSRQ, in which the optical spectrum has broad emission lines; BZB/BL Lac objects, in which the optical spectrum is featureless or contains only absorption lines from the host galaxy; BZU/uncertain type, comprising objects for which the authors could not find sufficient data to safely determine the source classification, and objects that have peculiar characteristics (see Massaro et al. 2010, for details). According to this classification, 96 of our objects are of the FSRQ type, 40 are BL Lacs, and the rest are of uncertain type. About 160 were observed by *Swift* simultaneously with *Planck*, mostly by means of dedicated target of opportunity (ToO) pointings. In the following we describe the selection criteria for each high-energy selected sample. Details of the radio-selected sample are given in Planck Collaboration (2011e).

2.1. The issue of blazar classification

The classification of blazars as either featureless (BL Lacs) or broad-lined objects (FSRQs), although very simple in principle,

is neither unambiguous, nor robust. The borderline between the two blazar subclasses, namely 5 Å in the source rest-frame for the EW of any emission line, was originally defined as a result of the optical identification campaigns of the sources discovered in the first well-defined and complete samples of (bright) radio and X-ray selected objects (Stickel et al. 1991; Stocke et al. 1991). However, we now know that well-known BL Lac objects such as OJ 287 – and BL Lac itself – exhibit emission lines with EWs well above the 5 Å limit on some occasions (Vermeulen et al. 1995; Corbett et al. 1996). Several other BL Lac objects have strong emission lines with EWs just below, and sometimes above the 5 Å threshold, depending on the variable continuum level (see e.g. Lawrence et al. 1996; Ghisellini et al. 2011, and references therein). Well-known FSRQs such as 3C 279 also appear nearly featureless during bright states (Pian et al. 1999). The detection of broad Lyman-α emission in the UV spectrum of classical BL Lacs such as Mkn 421 and Mkn 501 (Stocke et al. 2011) contributes to the blurring of the distinction between the two types of blazars.

It is difficult to differentiate between BL Lac objects and radio galaxies as BL Lacs have been defined as sources for which the 4000 Å Ca H&K break (a stellar absorption feature in the host galaxy) is diluted by non-thermal radiation more than a certain amount that was first quantified by Stocke et al. (1991) and then revised by Marcha et al. (1996), Landt et al. (2002), and Landt et al. (2004). The level of non-thermal blazar light around 4000 Å reflects the intrinsic radio power of the jet; it can be highly variable and depends strongly on the position of the peak of the synchrotron emission, thus ensuring that the border between BL Lacs and radio galaxies is quite uncertain. Giommi et al. (2012) tackled the problem of blazar classification using extensive Monte Carlo simulations and showed that the observed differences can be interpreted within a simple scenario where FSRQs and BL Lacs share the basic non-thermal emission properties.

In the present study, we relied on the blazar classification given in the Roma-BZCAT catalog (Massaro et al. 2010), which re-assessed the blazar subclass of each object after a critical review of the optical data available in the literature and in large public databases such as the SDSS (York et al. 2000). Despite that, some uncertainties remain, which may in turn influence our conclusions about the differences between BL Lacs and FSRQs. However, the large size of our samples ensures that a few misclassifications should not significantly affect our results. To assess the impact of both blazar misclassification and transitional objects in a quantitative way, it is necessary to perform detailed simulations.

2.2. The Fermi-LAT (γ-ray flux-limited) sample

Our γ-ray flux-limited sample was created from the *Fermi*-LAT Bright Source List[2] (Abdo et al. 2009b). We selected all the high Galactic latitude ($|b| > 10°$) blazars detected with high significance (TS > 100)[3]. To reduce the size of the sample and ensure that all the sources are well above the *Planck* sensitivity limit for one survey, we considered only the sources with radio flux density (taken from BZCAT) $S_{5\,\mathrm{GHz}} > 1$ Jy. We realized that this is a double cut, with a TS limit at γ-ray energies and a flux-density limit in the radio band. A TS limit translates into different γ-ray flux limits depending on the γ-ray spectral slope, with higher sensitivity to flat-spectrum sources (see Fig. 7 of Abdo et al. 2009b). Hence, for our statistical considerations we also considered the subsample with a flux cut of $F(E > 100\ \mathrm{MeV}) > 8 \times 10^{-8}$ ph cm^{-2} s^{-1}, which removed this dependence on the spectral slope.

The sample so defined includes 50 sources, 40 of which are brighter than the γ-ray flux limit of 8×10^{-8} ph cm^{-2} s^{-1}. Relaxing the radio flux density cut would have provided a purely γ-ray flux-limited sample and increased the number of sources to ≈70, but with about 40–50% of the objects with $S_{5\,\mathrm{GHz}} < 1$ Jy being undetected by *Planck*.

Details are presented in Table 1, where Col. 1 gives the source common name, Col. 2 gives the *Fermi*-LAT name as it appears in Abdo et al. (2010b), Cols. 3 and 4 give the source position in equatorial coordinates, Cols. 5–7 give the redshift, V magnitude, and X-ray flux (0.1–2.4 keV) from BZCAT (Massaro et al. 2010), Col. 8 gives the 1.4 GHz or 843 MHz flux density from NVSS (Condon et al. 1998) or from SUMSS (Mauch et al. 2003) with Dec $< -40°$, Col. 9 gives the γ-ray flux from Abdo et al. (2010b)[4], and Col. 10 gives the date of the *Swift* ToO observation made when the source was within the *Planck* field of view.

2.3. The Swift/BAT (hard X-ray flux-limited) sample

We defined our hard X-ray flux-limited sample starting from the *Swift*-BAT 54 month source catalog[5] (Cusumano et al. 2010), and selecting all the sources identified with blazars with X-ray flux $>10^{-11}$ erg cm^{-2} s^{-1} in the 15–150 keV energy band. The BAT catalog includes 70 known blazars that satisfy the X-ray flux condition, but many of them are too faint to be detected at millimetre wavelengths by *Planck*. Therefore, although a pure X-ray selection would be preferable, we have decided to add a mild radio flux-density constraint ($S_{5\,\mathrm{GHz}} > 100$ mJy, with $S_{5\,\mathrm{GHz}}$ taken from BZCAT) to select only sources that can be detected by *Planck* or for which *Planck* will be able to provide meaningful upper limits, leaving enough sources to build a statistically sizable sample. The list of the 34 sources included in this sample is given in Table 2. The column description is the same as for Table 1.

2.4. The ROSAT/RASS (soft X-ray flux-limited) sample

The soft X-ray flux-limited sample was defined starting from the RASS catalog (1RXS) (Voges et al. 1999), and selecting all the sources identified with blazars with count rates higher than 0.3 counts/s in the 0.1–2.4 keV energy band, and radio flux densities (taken from BZCAT) of $S_{5\,\mathrm{GHz}} > 200$ mJy. The reasons for using an additional radio flux constraint are the same as for the hard X-ray flux-limited sample, where, however, we chose 200 mJy to reduce the size of the sample to be comparable to those of the γ-ray and hard X-ray samples. We realize that this is a stringent cut that removes about two thirds of the sources from the purely soft X-ray selected sample. However, all the sources below the radio threshold *are HSP BL Lacs*, thus implying that the subsample of LBL sources remains purely X-ray flux-limited and, consequently, that high $\nu^{\mathrm{S}}_{\mathrm{peak}}$ objects are strongly underrepresented. The list of the 43 sources included in this sample

[2] http://www.asdc.asi.it/fermibsl/

[3] The test statistic (TS) is defined as TS $= -2\ln(L_0/L_1)$ with L_0 the likelihood of the null-hypothesis model and L_1 the likelihood of a competitive model (see e.g. Abdo et al. 2010c).

[4] We give average γ-ray fluxes from the 1-year *Fermi* catalog rather than the three-month fluxes that were used to define the sample for consistency with Tables 2 and 3.

[5] http://www.asdc.asi.it/bat54/

Table 1. The *Fermi*-LAT (γ-ray TS/flux-limited) sample.

Source name	*Fermi*-LAT name (1FGL)	RA (J2000)	Dec (J2000)	z	$R_{\rm mag}$	X-ray flux 0.1–2.4 keV [b]	Flux density 1.4 GHz[a] mJy	*Fermi* flux 1–100 GeV [c]	Swift obs. date	Blazar type
1Jy 0118−272	1FGLJ 0120.5−2700	01 20 31.6	−27 01 24	0.557	15.5	0.72	934	3.7 ± 0.4	[d]	BL Lac - LSP
S4 0133+47	1FGLJ 0137.0+4751	01 36 58.5	47 51 29	0.859	17.6	1.04	1138	9.6 ± 0.6	2010-02-05	FSRQ - LSP
PKS 0202−17	1FGLJ 0205.0−1702	02 04 57.6	−17 01 18	1.740	17.3	0.57	1220	1.5 ± 0.3	2010-01-08	FSRQ - LSP
PKS 0208−512	1FGLJ 0210.6−5101	02 10 46.2	−51 01 01	1.003	14.8	0.75	3493	7.1 ± 0.6	2009-11-26	Uncertain - LSP
PKS 0215+015	1FGLJ 0217.9+0144	02 17 48.9	01 44 49	1.715	18.7	2.56	751	6.0 ± 0.5	[d]	FSRQ - LSP
1Jy 0218+357	1FGLJ 0221.0+3555	02 21 05.5	35 56 14	0.944	20.0	0.85	1707	6.4 ± 0.5	2010-08-19	Uncertain - LSP
4C 28.07	1FGLJ 0237.9+2848	02 37 52.4	28 48 09	1.213	18.8	0.58	2197	3.7 ± 0.4	2010-02-05	FSRQ - LSP
PKS 0235+164	1FGLJ 0238.6+1637	02 38 38.9	16 36 59	0.940	18.5	1.24	1941	32.7 ± 1.1	2010-01-30	BL Lac - LSP
PKS 0332−403	1FGLJ 0334.2−4010	03 34 13.6	−40 08 25	[e]	17.5	0.73	1042	3.8 ± 0.4	2010-01-17	BL Lac - LSP
PKS 0420−01	1FGLJ 0423.2−0118	04 23 15.8	−01 20 33	0.916	16.7	1.39	2726	5.6 ± 0.5	2009-08-27	FSRQ - LSP
PKS 0426−380	1FGLJ 0428.6−3756	04 28 40.4	−37 56 19	1.030	16.3	0.42	753	25.7 ± 1.0	2010-08-17	BL Lac - LSP
PKS 0454−234	1FGLJ 0457.0−2325	04 57 03.1	−23 24 52	1.003	17.9	0.91	1727	32.5 ± 1.1	2010-02-25	FSRQ - LSP
PKS 0528+134	1FGLJ 0531.0+1331	05 30 56.4	13 31 55	2.070	18.9	0.80	1556	4.0 ± 0.5	2009-09-24	FSRQ - LSP
PKS 0537−441	1FGLJ 0538.8−4404	05 38 50.3	−44 05 08	0.892	16.0	2.10	3729	21.3 ± 0.9	2010-03-03	BL Lac - LSP
PKS 0735+17	1FGLJ 0738.2+1741	07 38 07.3	17 42 19	0.424	14.5	0.97	2258	4.4 ± 0.5	2010-10-07	BL Lac - ISP
S4 0814+425	1FGLJ 0818.2+4222	08 18 16.0	42 22 45	0.530	19.6	0.32	1091	8.7 ± 0.6	2010-10-15	BL Lac - LSP
OJ 535	1FGLJ 0825.0+5555	08 24 47.2	55 52 42	1.417	18.1	0.64	1449	0.9 ± 0.3	2010-03-28	FSRQ - LSP
PKS 0851+202	1FGLJ 0854.8+2006	08 54 48.8	20 06 30	0.306	14.4	1.72	1512	2.7 ± 0.4	2010-04-10	BL Lac - LSP
S4 0917+44	1FGLJ 0920.9+4441	09 20 58.4	44 41 54	2.190	19.2	1.04	1017	14.0 ± 0.7	2009-10-29	FSRQ - LSP
4C 55.17	1FGLJ 0957.7+5523	09 57 38.1	55 22 57	0.896	16.8	0.51	3079	10.5 ± 0.6	2009-11-01	FSRQ - LSP
4C 01.28	1FGLJ 1058.4+0134	10 58 29.6	01 33 58	0.888	17.6	1.08	3220	7.1 ± 0.6	2009-12-03	Uncertain - LSP
PKS 1057−79	1FGLJ 1058.1−8006	10 58 43.3	−80 03 54	0.581	17.3	0.43	534	2.2 ± 0.4	2010-08-30	BL Lac - LSP
PKS 1127−145	1FGLJ 1130.2−1447	11 30 07.0	−14 49 27	1.184	16.0	1.39	5622	2.4 ± 0.4	2009-12-28	FSRQ - LSP
PKS 1144−379	1FGLJ 1146.9−3812	11 47 01.3	−38 12 11	1.048	15.7	0.91	1804	2.4 ± 0.4	2010-06-24	BL Lac - LSP
4C 29.45	1FGLJ 1159.4+2914	11 59 31.8	29 14 44	0.729	16.4	0.84	2031	5.3 ± 0.5	2010-05-28	FSRQ - LSP
ON 231	1FGLJ 1221.5+2814	12 21 31.6	28 13 58	0.102	14.3	1.30	732	6.9 ± 0.5	2009-12-10	BL Lac - ISP
3C 273	1FGLJ 1229.1+0203	12 29 06.7	02 03 08	0.158	14.1	63.11	54 991	9.6 ± 0.6	2010-01-11	FSRQ - LSP
PKS 1244−255	1FGLJ 1246.7−2545	12 46 46.8	−25 47 49	0.635	16.7	1.30	1165	8.1 ± 0.6	2010-01-25	FSRQ - LSP
3C 279	1FGLJ 1256.2−0547	12 56 11.1	−05 47 21	0.536	15.0	20.90	9711	32.4 ± 1.1	2010-01-15	FSRQ - LSP
1Jy 1308+326	1FGLJ 1310.6+3222	13 10 28.6	32 20 43	0.997	19.6	0.53	1687	6.8 ± 0.5	2009-12-12	Uncertain - LSP
PKS 1502+106	1FGLJ 1504.4+1029	15 04 24.9	10 29 39	1.839	19.5	0.16	1774	67.0 ± 1.6	2010-07-29	FSRQ - LSP
4C −05.64	1FGLJ 1511.1−0545	15 10 53.5	−05 43 07	1.191	16.9	1.16	3569	2.1 ± 0.4	[d]	FSRQ - LSP
AP Lib	1FGLJ 1517.8−2423	15 17 41.8	−24 22 19	0.048	12.6	1.05	2042	5.6 ± 0.5	2010-02-20	BL Lac - LSP
OS −237.8	1FGLJ 1625.7−2524	16 25 46.8	−25 27 38	0.786	20.6	..	2521	4.4 ± 0.6	2010-08-26	Uncertain - LSP
4C 38.41	1FGLJ 1635.0+3808	16 35 15.4	38 08 04	1.814	17.3	0.17	2726	6.8 ± 0.5	2010-03-07	FSRQ - LSP
NRAO 512	1FGLJ 1642.5+3947	16 40 29.6	39 46 46	1.660	17.5	0.15	976	5.6 ± 0.5	2010-08-06	FSRQ - LSP
Mkn 501	1FGLJ 1653.9+3945	16 53 52.2	39 45 36	0.033	8.3	36.90	1558	8.3 ± 0.6	2010-03-21	BL Lac - HSP
OT 081	1FGLJ 1751.5+0937	17 51 32.8	09 39 00	0.322	17.0	1.18	623	6.4 ± 0.6	2010-04-01	Uncertain - LSP
S5 1803+784	1FGLJ 1800.4+7827	18 00 45.6	78 28 04	0.680	14.7	0.79	2223	3.0 ± 0.4	2009-10-13	BL Lac - LSP
2E 1908.2−2011	1FGLJ 1911.2−2007	19 11 09.6	−20 06 55	1.119	18.9	1.77	2714	4.5 ± 0.5	2009-10-04	FSRQ - LSP
PMNJ 1923−2104	1FGLJ 1923.5−2104	19 23 32.1	−21 04 33	0.874	16.6	0.77	3167	11.9 ± 0.7	2010-09-30	FSRQ - LSP
1Jy 2005−489	1FGLJ 2009.5−4849	20 09 25.3	−48 49 53	0.071	11.0	33.24	1282	5.0 ± 0.5	2009-10-05	BL Lac - HSP
PKS 2052−47	1FGLJ 2056.3−4714	20 56 16.3	−47 14 47	1.491	18.3	0.56	2223	4.6 ± 0.5	2010-10-18	FSRQ - LSP
S3 2141+17	1FGLJ 2143.4+1742	21 43 35.5	17 43 48	0.213	14.4	0.63	651	4.9 ± 0.5	2009-11-20	FSRQ - LSP
1Jy 2144+092	1FGLJ 2147.2+0929	21 47 10.1	09 29 46	1.113	16.9	1.49	934	4.1 ± 0.4	[d]	FSRQ - LSP
BL Lac	1FGLJ 2202.8+4216	22 02 43.2	42 16 40	0.069	12.5	1.58	6051	7.1 ± 0.6	2009-12-23	BL Lac - LSP
PKS 2204−54	1FGLJ 2207.8−5344	22 07 43.7	−53 46 33	1.215	18.2	0.52	1526	1.6 ± 0.3	2010-05-03	FSRQ - LSP
PKS 2227−08	1FGLJ 2229.7−0832	22 29 40.0	−08 32 54	1.560	16.8	8.74	968	4.6 ± 0.5	2009-11-19	FSRQ - LSP
4C 11.69	1FGLJ 2232.5+1144	22 32 36.4	11 43 50	1.037	16.5	1.26	7202	4.1 ± 0.4	2009-11-29	FSRQ - LSP
3C 454.3	1FGLJ 2253.9+1608	22 53 57.7	16 08 53	0.859	13.2	7.80	12 657	46.2 ± 1.3	2009-12-14	FSRQ - LSP

Notes. [a] 843 MHz flux is reported for sources with Dec < −40°. [b] Units of 10^{-12} erg cm^{-2} s^{-1}. [c] Units of 10^{-10} ph cm^{-2} s^{-1}. [d] *Swift* simultaneous observation not available. [e] Optical spectrum completely featureless or not available, redshift unknown.

is given in Table 3. The column description is the same as for Tables 1 and 2.

2.5. The radio flux-density limited sample

The radio flux-density limited sample is presented in the companion *Planck* paper (Planck Collaboration 2011e), where all the observational details are given. The sample consists of 104 bright northern and equatorial radio-loud AGN characterized by $S_{37\,\rm GHz} > 1$ Jy as measured with the Metsähovi radio telescope.

Although the samples are defined by different criteria, four sources are common to all samples. These are the well-known objects 3C 273, 3C 279, Mkn 501, and 3C 454.3, which are among the brightest objects across the entire electromagnetic spectrum. A summary of the number of sources common to more than one sample is given in Table 4.

3. Data analysis

3.1. Ground-based follow-up data

Following the launch of *Planck*, several follow-up programs with ground-based facilities started collecting simultaneous radio and optical data. In this paper, we used data from the observatories listed in Table 5.

3.1.1. APEX

Some sources from our sample were observed in the submillimetre domain with the 12-m Atacama Pathfinder Experiment

Table 2. The *Swift*-BAT (hard X-ray flux-limited) sample.

Source name	*Fermi*-LAT name	RA (J2000)	Dec (J2000)	z	$R_{\rm mag}$	X-ray flux 0.1–2.4 keV [b]	Flux density 1.4 GHz[a] mJy	*Fermi*-LAT flux 1–100 GeV [c]	Swift obs. date	Blazar type
III ZW 2	...	00 10 31.0	10 58 29	0.089	13.9	6.14	98	...	2010-07-08	FSRQ - LSP
S5 0014+813	...	00 17 08.4	81 35 08	3.387	15.9	0.77	693	...	2010-09-21	FSRQ - ISP
1ES 0033+595	1FGLJ 0035.9+5951	00 35 52.6	59 50 03	[e]	17.2	5.41	147	3.2 ± 0.5	[d]	BL Lac - HSP
Mkn 348	...	00 48 47.1	31 57 25	0.015	9.3	0.12	292	...	[d]	BL Lac - LSP
1Jy 0212+735	1FGLJ 0217.8+7353	02 17 30.8	73 49 32	2.367	18.8	0.54	2272	1.0 ± 0.4	2010-09-11	Uncertain - LSP
NGC 1275	1FGLJ 0319.7+4130	03 19 48.1	41 30 42	0.018	12.3	197.92	22 830	17.3 ± 0.8	2010-08-09	FSRQ - LSP
NRAO 140	1FGLJ 0334.2+3233	03 36 30.1	32 18 29	1.259	16.6	2.80	2677	1.0 ± 0.4	2010-08-25	Uncertain - LSP
3C 120	...	04 33 11.0	05 21 15	0.033	13.8	22.68	3440	...	2010-02-25	Uncertain - LSP
PKS 0521−36	1FGLJ 0522.8−3632	05 22 57.9	−36 27 30	0.055	11.6	10.42	15 620	2.9 ± 0.4	2010-03-05	Uncertain - LSP
PKS 0528+134	1FGLJ 0531.0+1331	05 30 56.4	13 31 55	2.070	18.9	0.80	1556	4.0 ± 0.5	2009-09-24	FSRQ - LSP
1Jy 0537−286	1FGLJ 0539.1−2847	05 39 54.2	−28 39 55	3.104	19.0	0.83	862	0.9 ± 0.0	2010-03-12	FSRQ - LSP
PKS 0548−322	...	05 50 40.6	−32 16 20	0.069	13.1	26.34	344	...	2010-03-12	BL Lac - HSP
B2.2 0743+25	1FGLJ 0746.6+2548	07 46 25.8	25 49 02	2.979	19.2	0.38	417	0.7 ± 0.2	2010-10-15	FSRQ - LSP
4C 71.07	1FGLJ 0842.2+7054	08 41 24.3	70 53 42	2.218	16.8	5.52	3823	1.2 ± 0.3	2010-03-21	FSRQ - LSP
Mkn 421	1FGLJ 1104.4+3812	11 04 27.3	38 12 31	0.030	8.3	180.94	767	26.1 ± 1.0	2009-11-17	BL Lac - HSP
PKS 1127−145	1FGLJ 1130.2−1447	11 30 07.0	−14 49 27	1.184	16.0	1.39	5622	2.4 ± 0.4	2009-12-28	FSRQ - LSP
PKS 1219+04	1FGLJ 1222.5+0415	12 22 22.5	04 13 15	0.967	17.1	0.91	800	0.9 ± 0.3	2010-07-17	FSRQ - LSP
3C 273	1FGLJ 1229.1+0203	12 29 06.7	02 03 08	0.158	14.1	63.11	54 991	9.6 ± 0.6	2010-01-11	FSRQ - LSP
3C 279	1FGLJ 1256.2−0547	12 56 11.1	−05 47 21	0.536	15.0	20.85	9711	32.4 ± 1.1	2010-01-15	FSRQ - LSP
AP Lib	1FGLJ 1517.8−2423	15 17 41.8	−24 22 19	0.048	12.6	1.05	2042	5.7 ± 0.5	2010-02-20	BL Lac - LSP
Mkn 501	1FGLJ 1653.9+3945	16 53 52.2	39 45 36	0.033	8.3	36.93	1558	8.3 ± 0.6	2010-03-21	BL Lac - HSP
ARP 102B	...	17 19 14.4	48 58 49	0.024	9.4	0.59	145	...	2010-03-31	Uncertain - ISP
PKSB 1830−210	1FGLJ 1833.6−2103	18 33 39.8	−21 03 39	2.507	16.6	0.69	10 896	10.7 ± 0.8	2010-09-23	FSRQ - LSP
OV −236	1FGLJ 1925.2−2919	19 24 51.0	−29 14 30	0.352	17.3	2.42	13 387	1.4 ± 0.4	2010-09-30	FSRQ - LSP
1ES 1959+650	1FGLJ 2000.0+6508	19 59 59.8	65 08 54	0.047	11.9	35.28	250.	6.0 ± 0.5	2009-09-26	BL Lac - HSP
1Jy 2126−158	...	21 29 12.1	−15 38 41	3.268	16.5	1.54	590.	...	2010-05-03	FSRQ - ISP
4C 06.69	1FGLJ 2148.5+0654	21 48 05.4	06 57 38	0.999	15.1	1.46	2589.	0.7 ± 0.3	2009-11-21	FSRQ - LSP
PKS 2149−307	...	21 51 55.5	−30 27 53	2.345	17.4	4.80	1243.	...	2010-05-11	FSRQ - LSP
BL Lac	1FGLJ 2202.8+4216	22 02 43.2	42 16 40	0.069	12.5	1.57	6051.	7.1 ± 0.6	2009-12-23	BL Lac - LSP
4C 31.63	...	22 03 14.9	31 45 38	0.295	14.3	3.22	2878.	...	2009-11-27	FSRQ - LSP
NGC 7213	...	22 09 16.2	−47 10 00	0.006	10.3	35.34	98.	...	2010-10-23	Uncertain
4C 11.69	1FGLJ 2232.5+1144	22 32 36.4	11 43 50	1.037	16.5	1.26	7202.	4.1 ± 0.4	2009-11-29	FSRQ - LSP
3C 454.3	1FGLJ 2253.9+1608	22 53 57.7	16 08 53	0.859	13.2	7.80	12 657.	46.2 ± 1.3	2009-12-14	FSRQ - LSP
PKS 2325+093	1FGLJ 2327.7+0943	23 27 33.5	09 40 09	1.843	18.8	0.73	741.	3.0 ± 0.4	2010-07-18	FSRQ - LSP

Notes. [a] 843 MHz flux is reported for sources with Dec < −40°. [b] Units of 10^{-12} erg cm^{-2} s^{-1}. [c] Units of 10^{-10} ph cm^{-2} s^{-1}. [d] *Swift* simultaneous observation not available. [e] Optical spectrum completely featureless or not available, redshift unknown.

(APEX) in Chile. The observations were made using the LABOCA bolometer array centered at 345 GHz. Data were taken at two epochs: September 3–4, 2009, and November 12, 2009. The data were reduced using the script package *minicrush*[6], version 30-Oct.-2009. Uranus was used as a calibrator of the flux densities.

3.1.2. ATCA-PACO

The *Planck*-ATCA Co-eval Observations (PACO) project (Massardi et al. 2011a; Bonavera et al. 2011) observed 480 sources selected from the Australia Telescope 20 GHz catalogue (AT20G, Massardi et al. 2011b), with the Australia Telescope Compact Array (ATCA) in the frequency range 4.5−40 GHz, at several epochs close in time to the *Planck* observations in the period July 2009 to August 2010. The PACO sample is a complete, flux-density limited, and spectrally selected sample of southern sources, with the exception of the region with Galactic latitude $|b| < 5°$. A total of 147 PACO point-like sources have at least one observation within ten days of the *Planck* observations.

3.1.3. Effelsberg and IRAM

Quasi-simultaneous cm/mm radio spectra for a larger number of *Planck* blazars were obtained within the framework of a *Fermi* monitoring program of γ-ray blazars (F-GAMMA: Fuhrmann et al. 2007; Angelakis et al. 2008) on the Effelsberg 100-m and IRAM 30-m telescopes. The frequency range was 2.64−142 GHz.

The Effelsberg measurements were conducted with the secondary focus heterodyne receivers at 2.64, 4.85, 8.35, 10.45, 14.60, 23.05, 32.00, and 43.00 GHz. The observations were performed quasi-simultaneously with cross-scans, that is by slewing over the source position in azimuth and elevation with the number of sub-scans chosen to reach the desired sensitivity (for details, see Fuhrmann et al. 2008; Angelakis et al. 2008). Pointing offset, gain, atmospheric opacity, and sensitivity corrections were applied to the data.

The IRAM 30-m observations were carried out with calibrated cross-scans using the EMIR horizontal and vertical polarization receivers operating at 86.2 GHz and 142.3 GHz. The opacity-corrected intensities were converted into the standard temperature scale and finally corrected for small remaining pointing offsets and systematic gain-elevation effects. Conversion to a standard flux density scale was based on frequent observations of primary calibrators (Mars, Uranus) and secondary calibrators (W3(OH), K3-50A, NGC 7027).

From this program, radio spectra measured quasi-simultaneously with the *Planck* observations were collected for a total of 37 *Planck* blazars during the period August 2009 to June 2010. Results are reported in Tables 6 and 7.

[6] http://www.submm.caltech.edu/~sharc/crush/

Table 3. The ROSAT/RASS (soft X-ray flux-limited) sample.

Source name	*Fermi*-LAT name	RA (J2000)	Dec (J2000)	z	R_{mag}	X-ray flux 0.1–2.4 keV [b]	Flux density 1.4 GHz[a] mJy	*Fermi*-LAT flux 1–100 GeV [c]	Swift obs. date	Blazar type
III ZW 2	...	00 10 31.0	10 58 29	0.089	13.9	6.14	98.	...	2010-07-08	FSRQ - LSP
GB6J 0214+5145	...	02 14 17.9	51 44 52	0.049	16.5	4.58	294.	...	[d]	BL Lac - HSP
3C 120	...	04 33 11.0	05 21 15	0.033	13.8	22.68	3440.	...	2010-02-25	Uncertain - LSP
PKS 0521−36	1FGLJ 0522.8−3632	05 22 57.9	−36 27 30	0.055	11.6	10.42	15 620.	2.9 ± 0.4	2010-03-05	Uncertain - LSP
PKS 0548−322	...	05 50 40.6	−32 16 20	0.069	13.1	26.34	344.	...	2010-03-12	BL Lac - HSP
IRAS-L 06229−643	...	06 23 07.6	−64 36 20	0.129	13.7	5.34	274.	...	2010-08-18	FSRQ - LSP
4C 71.07	1FGLJ 0842.2+7054	08 41 24.3	70 53 42	2.218	16.8	5.52	3823.	1.2 ± 0.3	2010-03-21	FSRQ - LSP
B2 0912+29	1FGLJ 0915.7+2931	09 15 52.4	29 33 24	[e]	15.0	6.25	342.	2.1 ± 0.3	2010-10-28	BL Lac - HSP
PKS 0921−213	...	09 23 38.8	−21 35 47	0.053	12.8	4.80	268.	...	2010-05-02	Uncertain - LSP
1H 1013+498	1FGLJ 1015.1+4927	10 15 04.1	49 26 00	0.212	15.1	13.23	378.	8.7 ± 0.6	2010-04-24	BL Lac - HSP
1RXSJ 105837.5+562816	1FGLJ 1058.6+5628	10 58 37.7	56 28 11	0.143	14.0	3.13	228.	5.7 ± 0.5	2010-04-18	BL Lac - HSP
PKS 1124−186	1FGLJ 1126.8−1854	11 27 04.3	−18 57 17	1.048	19.2	5.33	536.	2.4 ± 0.4	2010-06-10	FSRQ - LSP
B2 1128+31	...	11 31 09.4	31 14 05	0.289	15.8	5.02	370.	...	2009-11-28	FSRQ - HSP
S5 1133+704	1FGLJ 1136.6+7009	11 36 26.4	70 09 27	0.045	11.0	35.08	327.	1.7 ± 0.3	2009-10-27	BL Lac - HSP
4C 49.22	...	11 53 24.4	49 31 08	0.334	16.9	3.31	1572.	...	200911-17	FSRQ - LSP
ON 325	1FGLJ 1217.7+3007	12 17 52.0	30 07 00	0.130	14.5	24.90	572.	6.7 ± 0.6	2009-12-03	BL Lac - HSP
PKS 1217+02	...	12 20 11.8	02 03 42	0.241	15.6	2.78	672.	...	2010-06-24	FSRQ - LSP
3C 273	1FGLJ 1229.1+0203	12 29 06.7	02 03 08	0.158	14.1	63.11	54 991.	9.6 ± 0.6	2010-01-11	FSRQ - LSP
PG 1246+586	1FGLJ 1248.2+5820	12 48 18.7	58 20 28	[e]	14.5	3.99	245.	4.5 ± 0.4	2010-05-20	BL Lac - ISP
3C 279	1FGLJ 1256.2−0547	12 56 11.1	−05 47 21	0.536	15.0	20.85	9711.	32.4 ± 1.1	2010-01-15	FSRQ - LSP
1Jy 1302−102	...	13 05 33.0	−10 33 19	0.286	14.4	4.20	711.	...	[d]	FSRQ - ISP
GB6B 1347+0955	...	13 50 22.1	09 40 10	0.133	13.6	3.74	293.	...	2010-07-18	Uncertain - ISP
1WGAJ 1407.5−2700	...	14 07 29.7	−27 01 04	0.022	9.7	15.28	646.	...	2010-02-12	Uncertain - HSP
3C 298.0	...	14 19 08.1	06 28 34	1.437	16.4	0.00	6100.	...	2010-07-30	Radio Galaxy
BZQJ 1423+5055	...	14 23 14.1	50 55 37	0.286	15.1	3.35	178.	...	2010-07-13	FSRQ - HSP
PG 1424+240	1FGLJ 1426.9+2347	14 27 00.3	23 48 00	[e]	14.5	3.57	430.	10.2 ± 0.6	2010-01-22	BL Lac - ISP
1RXSJ 145603.4+504825	...	14 56 03.6	50 48 25	0.479	18.1	13.02	220.	...	2009-12-25	BL Lac - HSP
BZQJ 1507+0415	...	15 07 59.7	04 15 12	1.701	19.0	6.11	167.	...	2010-08-05	FSRQ - LSP
PG 1553+113	...	15 55 43.0	11 11 24	[e]	14.0	17.85	312.	...	2010-02-05	BL Lac - ISP
WE 1601+16W3	...	16 03 38.0	15 54 02	0.110	13.4	4.14	97.	...	2010-08-14	Uncertain - HSP
3C 345	1FGLJ 1642.5+3947	16 42 58.8	39 48 37	0.593	15.0	2.52	7099.	5.6 ± 0.5	2010-03-06	FSRQ - LSP
Mkn 501	1FGLJ 1653.9+3945	16 53 52.2	39 45 36	0.033	8.3	36.93	1558.	8.3 ± 0.6	2010-03-21	BL Lac - HSP
1ES 1741+196	1FGLJ 1744.2+1934	17 43 57.8	19 35 09	0.084	12.7	4.23	301.	1.1 ± 0.3	[d]	BL Lac - ISP
PKS 1833−77	...	18 40 38.4	−77 09 28	0.018	8.3	5.93	1108.	...	2010-03-11	Uncertain - ISP
1ES 1959+650	1FGLJ 2000.0+6508	19 59 59.8	65 08 54	0.047	11.9	35.28	250.	6.0 ± 0.5	2009-09-26	BL Lac - HSP
1Jy 2005−489	1FGLJ 2009.5−4849	20 09 25.3	−48 49 53	0.071	11.0	33.24	1282.	5.0 ± 0.5	2009-10-05	BL Lac - HSP
PKS 2149−307	...	21 51 55.5	−30 27 53	2.345	17.4	4.80	1243.	...	2010-05-11	FSRQ - LSP
NGC 7213	...	22 09 16.2	−47 10 00	0.006	10.3	35.34	98.	...	2010-10-23	Uncertain - HSP
PKS 2227−399	...	22 30 40.2	−39 42 52	0.318	16.0	4.23	369.	...	2010-05-09	Uncertain - ISP
3C 454.3	1FGLJ 2253.9+1608	22 53 57.7	16 08 53	0.859	13.2	7.80	12 657.	46.2 ± 1.3	2009-12-14	FSRQ - LSP
PKS 2300−18	...	23 03 02.9	−18 41 25	0.129	15.5	5.16	861.	...	2010-05-30	Uncertain - ISP
PKS 2331−240	...	23 33 55.2	−23 43 40	0.048	11.4	3.92	782.	...	2010-06-05	Uncertain - ISP
1ES 2344+514	1FGLJ 2347.1+5142	23 47 04.8	51 42 17	0.044	10.7	7.71	250.	1.4 ± 0.3	2010-01-17	BL Lac - HSP

Notes. [a] 843 MHz flux is reported for sources with Dec < −40°. [b] Units of 10^{-12} erg cm^{-2} s^{-1}. [c] Units of 10^{-10} ph cm^{-2} s^{-1}. [d] *Swift* simultaneous observation not available. [e] Optical spectrum completely featureless or not available, redshift unknown.

Table 4. Summary of the samples, blazar types, and selection methods considered in this paper.

Sample	Selection band	No. of sources	Blazars FS/BL/Unc.	Other AGN	Sources in common RASS	BAT	*Fermi*-LAT	Radio	All
RASS	Soft X-ray	43	15/16/11	1	...	12	5	9	4
BAT	Hard X-ray	34	21/7/6	...	12	...	9	16	4
Fermi-LAT*	γ-ray	50	28/16/6	...	5	9	...	23	4
Fermi-LAT FL**	γ-ray	40	27/8/5	...	3	7	...	19	3
Total this paper		105	52/32/20	1	...	...	...	...	...
Radio	radio	104	73/18/10	3	9	16	23	...	4

Notes. (*) Total *Fermi*-LAT sample (TS limited), (**) Flux-limited *Fermi*-LAT sample $F(E > 100\,\mathrm{MeV}) > 8 \times 10^{-8}$ ph cm^{-2} s^{-1}.

3.1.4. Medicina

The Simultaneous Medicina *Planck* Experiment (SiMPlE, Procopio et al. 2011) used the 32-m Medicina single dish to make almost simultaneous observations at 5 GHz and 8.3 GHz of the 263 sources of the NEWPS sample (Massardi et al. 2009) with Dec > 0°, and partially overlapping with the PACO observations for −10° < Dec < 0°. The project began in June 2010 and finished in June 2011, observing our sample several times throughout two complete *Planck* surveys. It does not overlap with the *Planck* first survey.

3.1.5. Metsähovi

The 37 GHz observations were made with the 13.7-m Metsähovi radio telescope using a 1 GHz bandwidth, dual-beam receiver

Table 5. Optical and radio observatories participating in the *Planck* multi-frequency campaigns.

Radio observatory	Frequencies [GHz]
APEX, Chile	345
ATCA, Australia	4.7, 5.2, 5.8, 6.3, 8.2, 8.7, 9.3, 9.8, 17.2, 17.7, 18.3, 18.8 23.2, 23.7, 24.3, 24.8, 32.2, 32.7, 33.3, 33.8, 38.2, 38.7, 39.3, 39.8
Effelsberg, Germany	2.64, 4.85, 8.35, 10.45, 14.60, 23.05, 32.00, 43.00
IRAM, Spain	86.2, 142.3
Medicina, Italy	5, 8
Metsahovi, Finland	37
OVRO, USA	15
RATAN, Russia	1.1, 2.3, 4.8, 7.7, 11.2, 21.7
UMRAO, USA	4.8, 8.0, 14.5
VLA, USA	5, 8, 22, 43
Optical observatory	Band
KVA, Spain	*R*
Xinglong, China	*I*

centered at 36.8 GHz. We performed ON-ON observations, by alternating between the source and the sky in each feed horn. A typical integration time for obtaininig one flux density data point was 1200–1400 s. The telescope detection limit at 37 GHz was ~0.2 Jy under optimal conditions. Data points with a signal-to-noise ratio (S/N) smaller than four are handled as non-detections. The flux-density scale was set by observations of DR 21. Sources NGC 7027, 3C 274, and 3C 84 were used as secondary calibrators. A detailed description of the data reduction and analysis is given in Teräsranta et al. (1998). The error estimate in the flux density includes the contribution from the measurement rms and the uncertainty in the absolute calibration.

3.1.6. OVRO

Some of the sources in our samples were monitored at 15 GHz using the 40-m telescope of the Owens Valley Radio Observatory as part of a larger monitoring program (Richards et al. 2011). The flux density of each source was measured approximately twice weekly, with occasional gaps due to poor weather or instrumental problems. The telescope was equipped with a cooled receiver installed at prime focus, with two symmetric off-axis corrugated horn feeds that are sensitive to left circular polarization. The telescope and receiver combination produces a pair of approximately Gaussian beams (157 arcsec *FWHM*), separated in azimuth by 12.95 arcmin. The receiver has a central frequency of 15.0 GHz, a 3.0 GHz bandwidth, and a noise-equivalent reception bandwidth of 2.5 GHz. Measurements were made using a Dicke-switched dual-beam system, with a second level of switching in azimuth where we alternated between source and sky in each of the two horns. Our calibration is referred to 3C 286, for which a flux density of 3.44 Jy at 15 GHz is assumed (Baars et al. 1977). Details of the observations, calibration, and analysis are given by Richards et al. (2011).

3.1.7. RATAN

A six-frequency broadband radio spectrum was obtained with the RATAN-600 radio telescope in transit mode by observing simultaneously at 1.1, 2.3, 4.8, 7.7, 11.2, and 21.7 GHz (Parijskij 1993; Berlin & Friedman 1996). Data were reduced using the RATAN standard software FADPS (Flexible Astronomical Data Processing System) reduction package (Verkhodanov 1997). The flux density measurement procedure at RATAN-600 is described by Aliakberov et al. (1985).

3.1.8. UMRAO

Centimetre-band observations were obtained with the University of Michigan 26-m prime focus paraboloid equipped with radiometers operating at central frequencies of 4.8, 8.0, and 14.5 GHz. Observations at all three frequencies utilized rotating polarimeter systems permitting both total flux density and linear polarization to be measured. A typical measurement consisted of 8 to 16 individual measurements over a 20–40 min time period. Frequent drift scans were made across stronger sources to verify the telescope pointing correction curves; and observations of program sources were intermixed with observations of a grid of calibrator sources to correct for temporal changes in the antenna aperture efficiency. The flux scale was based on observations of Cassiopeia A (Baars et al. 1977). Details of the calibration and analysis techniques are described by Aller et al. (1985).

3.1.9. VLA

The Very Large Array (VLA) and, since Spring 2010, the Expanded VLA (EVLA), observed a subset of the sources as simultaneously as possible. Most of the VLA and EVLA runs were performed in one to two hour chunks of time. We observed during a one-hour chunk of time, in addition to flux calibrators and phase calibrators, typically 5–8 *Planck* sources. In many cases, VLA flux-density and phase calibrators were themselves of interest, since they were bright enough to be detected by *Planck*. For these bright sources, the integration times could be extremely short.

Integration times were about 30 s at 4.86 GHz and 8.46 GHz, 100 s at 22.46 GHz, and 120 s at 43.34 GHz. All VLA/EVLA flux density measurements were calibrated using standard values for one or both of the primary calibrator sources used by NRAO, 3C 48 or 3C 286, and the *u-v* data were flagged, calibrated, and imaged using standard NRAO software (AIPS or CASA). It is important to bear in mind that the VLA and EVLA were in different configurations at different times in the several months duration of the observations. As a consequence, the angular resolution changed, becoming, for a given configuration, much higher at higher frequencies. For that reason, sources that appeared to be resolved in any VLA configuration or at any VLA frequency were carefully flagged.

Table 6. Effelsberg data.

J2000.0 name	Source name	Obs. date	Flux density 2.64 GHz (Jy)	Flux density 4.85 GHz (Jy)	Flux density 8.35 GHz (Jy)	Flux density 10.45 GHz (Jy)	Flux density 14.60 GHz (Jy)	Flux density 23.05 GHz (Jy)	Flux density 32.00 GHz (Jy)
J0217+0144	PKS 0215+015	2010-01-03	0.932 ± 0.011	1.265 ± 0.011	1.649 ± 0.022	1.790 ± 0.028	1.86 ± 0.05	...	...
J0217+0144	PKS 0215+015	2010-01-31	0.964 ± 0.010	1.315 ± 0.011	1.740 ± 0.021	1.878 ± 0.026	1.85 ± 0.07	1.77 ± 0.08	1.47 ± 0.13
J0237+2848	4C 28.07	2010-01-31	2.838 ± 0.029	2.670 ± 0.023	2.53 ± 0.04	2.46 ± 0.04	2.33 ± 0.09	2.17 ± 0.10	...
J0238+1636	PKS 0235+164	2010-01-31	1.254 ± 0.013	1.165 ± 0.010	1.073 ± 0.015	1.037 ± 0.014	0.98 ± 0.04	1.06 ± 0.06	1.23 ± 0.11
J0530+1331	PKS 0528+134	2009-08-29	3.191 ± 0.028	2.886 ± 0.025	2.38 ± 0.07	2.19 ± 0.09	1.73 ± 0.06	1.48 ± 0.09	1.04 ± 0.03
J0530+1331	PKS 0528+134	2009-09-28	...	2.779 ± 0.024	2.34 ± 0.03	2.15 ± 0.03	1.99 ± 0.05	1.62 ± 0.05	1.51 ± 0.05
J0530+1331	PKS 0528+134	2009-11-03	3.219 ± 0.027	2.980 ± 0.027	2.33 ± 0.04	2.15 ± 0.03	1.88 ± 0.05	1.57 ± 0.06	1.32 ± 0.05
J0530+1331	PKS 0528+134	2010-03-01	3.128 ± 0.029	2.639 ± 0.024	2.13 ± 0.03	1.93 ± 0.03	...	...	...
J0530+1331	PKS 0528+134	2010-03-31	...	...	...	...	1.36 ± 0.09	...	...
J0854+2006	PKS 0851+202	2009-11-03	1.448 ± 0.012	2.258 ± 0.020	4.04 ± 0.07	5.14 ± 0.08	6.61 ± 0.19	7.75 ± 0.28	7.71 ± 0.24
J0854+2006	PKS 0851+202	2009-11-16	...	2.475 ± 0.021	...	5.62 ± 0.08	6.86 ± 0.19	8.9 ± 0.3	9.0 ± 0.3
J0854+2006	PKS 0851+202	2010-04-01	2.249 ± 0.021	3.88 ± 0.03	6.31 ± 0.08	7.02 ± 0.12	7.22 ± 0.22	7.2 ± 0.3	6.89 ± 0.27
J0854+2006	PKS 0851+202	2010-05-02	2.19 ± 0.03	3.71 ± 0.04	5.03 ± 0.07	5.22 ± 0.08	5.44 ± 0.14	5.13 ± 0.25	4.66 ± 0.15
J0854+2006	PKS 0851+202	2010-05-24	2.291 ± 0.021	3.56 ± 0.03	4.39 ± 0.06	...	4.20 ± 0.12	2.98 ± 0.10	2.08 ± 0.20
J1104+3812	Mkn 421	2009-11-15	0.680 ± 0.006	0.561 ± 0.005	0.434 ± 0.007	0.383 ± 0.009	...	0.230 ± 0.009	...
J1104+3812	Mkn 421	2009-11-28	0.674 ± 0.006	0.572 ± 0.010	0.473 ± 0.006	0.44 ± 0.04	...	...	...
J1104+3812	Mkn 421	2010-01-04	0.713 ± 0.007	0.573 ± 0.005	0.484 ± 0.007	0.448 ± 0.007	0.418 ± 0.011	0.39 ± 0.05	0.393 ± 0.014
J1104+3812	Mkn 421	2010-02-28	0.73 ± 0.09	0.561 ± 0.005	0.447 ± 0.007	0.426 ± 0.019	...	...	...
J1104+3812	Mkn 421	2010-04-02	0.683 ± 0.007	0.584 ± 0.005	0.498 ± 0.006	0.461 ± 0.010	...	...	...
J1104+3812	Mkn 421	2010-05-02	0.690 ± 0.019	0.575 ± 0.006	0.495 ± 0.006	0.459 ± 0.008	0.418 ± 0.013	...	...
J1104+3812	Mkn 421	2010-05-24	0.701 ± 0.006	0.603 ± 0.006	0.514 ± 0.007	...	0.433 ± 0.013	...	...
J1217+3007	PKS 1217+02	2010-05-24	0.479 ± 0.004	0.425 ± 0.004	0.379 ± 0.005	0.368 ± 0.006	0.327 ± 0.024	...	...
J1217+3007	PKS 1217+02	2010-06-27	0.473 ± 0.005	0.399 ± 0.004	0.357 ± 0.005	0.328 ± 0.015	0.296 ± 0.011	...	0.263 ± 0.013
J1229+0203	3C 273	2010-02-01	46.7 ± 0.5	39.7 ± 0.3	33.6 ± 0.4	31.5 ± 0.5	28.0 ± 0.9	25.7 ± 1.2	25.6 ± 2.3
J1256−0547	3C 279	2010-02-01	8.73 ± 0.09	8.99 ± 0.08	9.72 ± 0.12	10.28 ± 0.20	11.2 ± 0.4	14.0 ± 0.6	15.5 ± 1.4
J1256−0547	3C 279	2010-02-28	8.68 ± 0.08	8.99 ± 0.08	9.71 ± 0.14	10.25 ± 0.17	11.1 ± 0.5	12.4 ± 0.6	15.7 ± 0.6
J1256−0547	3C 279	2010-06-26	8.16 ± 0.08	8.90 ± 0.08	10.30 ± 0.14	10.89 ± 0.16	12.1 ± 0.8	9.8 ± 0.4	...
J1310+3220	1Jy 1308+326	2009-11-28	0.946 ± 0.008	1.391 ± 0.012	1.96 ± 0.06	2.39 ± 0.05	2.57 ± 0.13	...	...
J1635+3808	4C 38.41	2010-02-28	3.048 ± 0.028	3.45 ± 0.03	3.80 ± 0.06	3.95 ± 0.08	4.01 ± 0.17	...	...
J1635+3808	4C 38.41	2010-04-02	3.100 ± 0.029	3.52 ± 0.03	3.63 ± 0.05	3.74 ± 0.11	3.54 ± 0.10	3.06 ± 0.10	...
J1642+3948	3C 345	2010-03-01	6.96 ± 0.06	6.98 ± 0.07	7.44 ± 0.11	7.58 ± 0.13	7.6 ± 0.3	6.17 ± 0.22	...
J1653+3945	Mkn 501	2010-03-01	1.503 ± 0.014	1.435 ± 0.014	1.332 ± 0.020	1.252 ± 0.021	1.15 ± 0.05	...	...
J1653+3945	Mkn 501	2010-05-02	1.543 ± 0.021	1.443 ± 0.014	1.341 ± 0.017	1.258 ± 0.018	1.179 ± 0.029	1.03 ± 0.05	0.89 ± 0.06
J1653+3945	Mkn 501	2010-05-25	1.558 ± 0.014	1.458 ± 0.014	1.333 ± 0.017	...	1.13 ± 0.03	0.774 ± 0.028	0.55 ± 0.07
J1653+3945	Mkn 501	2010-06-27	1.592 ± 0.016	1.504 ± 0.013	1.415 ± 0.019	1.347 ± 0.023	...	0.80 ± 0.03	...
J1800+7828	S5 1803+784	2009-09-28	...	2.069 ± 0.018	2.31 ± 0.03	2.39 ± 0.04	2.43 ± 0.06	2.19 ± 0.08	2.16 ± 0.09
J1800+7828	S5 1803+784	2009-11-04	1.950 ± 0.017	2.111 ± 0.017	2.36 ± 0.03	2.44 ± 0.04	2.56 ± 0.13	...	...
J2202+4216	BL Lac	2009-11-28	3.79 ± 0.04	4.26 ± 0.05	4.40 ± 0.07	4.55 ± 0.14	4.17 ± 0.16	4.21 ± 0.15	...
J2202+4216	BL Lac	2009-11-29	...	...	...	4.36 ± 0.12	4.03 ± 0.13	3.88 ± 0.12	...
J2202+4216	BL Lac	2010-01-03	3.58 ± 0.04	3.76 ± 0.03	3.95 ± 0.05	3.96 ± 0.06	3.86 ± 0.10	3.71 ± 0.19	3.51 ± 0.13
J2202+4216	BL Lac	2010-01-04	...	...	...	3.48 ± 0.17	2.77 ± 0.08	...	...
J2202+4216	BL Lac	2010-05-25	3.31 ± 0.03	3.83 ± 0.04	4.30 ± 0.06	4.31 ± 0.13	3.94 ± 0.14	3.8 ± 0.5	...
J2202+4216	BL Lac	2010-06-27	4.63 ± 0.04	...	4.86 ± 0.06	5.34 ± 0.08	5.17 ± 0.19	4.62 ± 0.29	4.7 ± 0.5
J2203+3145	4C 31.63	2009-11-30	...	2.323 ± 0.020	...	2.64 ± 0.05	2.58 ± 0.06	2.64 ± 0.09	2.75 ± 0.09
J2253+1608	3C 454.3	2009-11-28	11.63 ± 0.10	9.68 ± 0.08	8.13 ± 0.10	8.05 ± 0.13	8.5 ± 0.3	15.1 ± 0.5	...
J2253+1608	3C 454.3	2009-11-29	11.70 ± 0.10	9.69 ± 0.08	...	...	...	...	...
J2253+1608	3C 454.3	2010-01-03	11.53 ± 0.12	9.73 ± 0.08	9.07 ± 0.12	9.28 ± 0.15	10.48 ± 0.27	16.6 ± 0.8	21.2 ± 0.7
J2253+1608	3C 454.3	2010-05-23	11.58 ± 0.13	11.75 ± 0.10	15.6 ± 0.5	18.0 ± 0.9	21.5 ± 2.6	19.6 ± 1.5	21.1 ± 2.0
J2253+1608	3C 454.3	2010-06-27	11.46 ± 0.11	12.22 ± 0.11	16.76 ± 0.22	19.53 ± 0.26	23.4 ± 0.9	26.8 ± 1.7	27.8 ± 1.0

Table 7. IRAM data.

J2000.0 name	Source name	Obs. date	Flux density 86.2 GHz (Jy)	Flux density 142.3 GHz (Jy)
J0217+0144	PKS 0215+015	2010-02-01	1.91 ± 0.18	2.0 ± 0.4
J0237+2848	4C 28.07	2010-02-01	1.491 ± 0.017	1.27 ± 0.08
J0238+1636	PKS 0235+164	2010-02-01	1.87 ± 0.13	1.92 ± 0.27
J0238+1636	PKS 0235+164	2010-07-29	1.46 ± 0.22	1.6 ± 0.4
J0238+1636	PKS 0235+164	2010-08-02	1.45 ± 0.16	1.49 ± 0.27
J0238+1636	PKS 0235+164	2010-08-24	1.39 ± 0.13	1.33 ± 0.13
J0433+0521	3C 120	2010-03-01	1.864 ± 0.016	1.034 ± 0.001
J0530+1331	PKS 0528+134	2009-08-27	1.58 ± 0.10	1.22 ± 0.10
J0530+1331	PKS 0528+134	2010-03-22	0.81 ± 0.14	0.52 ± 0.09
J0530+1331	PKS 0528+134	2010-09-20	0.88 ± 0.12	0.57 ± 0.06
J0818+4222	S4 0814+425	2010-10-22	0.84 ± 0.10	0.94 ± 0.25
J0854+2006	PKS 0851+202	2010-03-22	6.0 ± 0.6	5.0 ± 0.5
J0854+2006	PKS 0851+202	2010-04-26	3.95 ± 0.17	3.12 ± 0.29
J1104+3812	Mkn 421	2010-04-26	0.6 ± 0.3	0.38 ± 0.05
J1104+3812	Mkn 421	2010-05-31	...	0.50 ± 0.06
J1256−0547	3C 279	2010-01-31	13.7 ± 0.6	12.5 ± 1.8
J1256−0547	3C 279	2010-06-14	16.6 ± 1.1	12.3 ± 1.4
J1256−0547	3C 279	2010-06-17	13.4 ± 0.8	10.4 ± 1.1
J1256−0547	3C 279	2010-07-01	13.9 ± 1.1	11.2 ± 1.6
J1256−0547	3C 279	2010-07-05	14.44 ± 0.22	12.0 ± 0.5
J1504+1029	PKS 1502+106	2010-08-02	0.7 ± 0.3	0.49 ± 0.17
J1504+1029	PKS 1502+106	2010-08-24	0.9 ± 0.4	0.53 ± 0.10
J1635+3808	4C 38.41	2010-03-22	3.31 ± 0.23	2.7 ± 0.4
J1635+3808	4C 38.41	2010-08-02	3.46 ± 0.27	2.9 ± 0.4
J1635+3808	4C 38.41	2010-08-24	3.58 ± 0.18	3.05 ± 0.28
J1642+3948	3C 345	2010-03-22	5.04 ± 0.20	3.9 ± 0.4
J1653+3945	Mkn 501	2009-08-27	...	0.51 ± 0.09
J1653+3945	Mkn 501	2010-03-22	0.70 ± 0.14	0.56 ± 0.10
J1653+3945	Mkn 501	2010-04-28	0.78 ± 0.15	0.579 ± 0.004
J1653+3945	Mkn 501	2010-05-31	0.81 ± 0.07	0.666 ± 0.026
J1653+3945	Mkn 501	2010-07-01	0.94 ± 0.29	0.93 ± 0.04
J1653+3945	Mkn 501	2010-08-02	0.87 ± 0.19	0.72 ± 0.18
J1653+3945	Mkn 501	2010-08-24	1.00 ± 0.25	0.80 ± 0.16
J1653+3945	Mkn 501	2010-10-23	0.789 ± 0.019	0.746 ± 0.018
J2202+4216	BL Lac	2010-05-31	5.0 ± 0.6	4.2 ± 0.8
J2202+4216	BL Lac	2010-07-01	6.5 ± 1.0	7.9 ± 1.8
J2202+4216	BL Lac	2010-06-08	5.58 ± 0.19	5.8 ± 0.5
J2202+4216	BL Lac	2010-06-17	5.7 ± 0.5	5.6 ± 0.7
J2202+4216	BL Lac	2010-06-21	6.8 ± 1.0	7.7 ± 1.2
J2253+1608	3C 454.3	2009-11-21	31.3 ± 0.6	32.4 ± 1.3
J2253+1608	3C 454.3	2010-05-31	31.4 ± 0.9	27.3 ± 2.6
J2253+1608	3C 454.3	2010-06-08	25.66 ± 0.24	19.7 ± 0.4
J2253+1608	3C 454.3	2010-06-17	26.0 ± 1.4	22.2 ± 2.5
J2253+1608	3C 454.3	2010-06-21	28.8 ± 1.1	28.2 ± 2.2
J2253+1608	3C 454.3	2010-07-01	25.11 ± 0.07	26.3 ± 0.9

3.1.10. KVA

Optical observations were made with the 35 cm KVA (Kunliga Vetenskapsakademiet) telescope at La Palma, Canary islands. All observations were made through the *R*-band filter ($\lambda_{\rm eff}$ = 640 nm) using a Santa Barbara ST-8 CCD camera with a gain factor of 2.3 e^-/ADU and readout noise of 14 electrons. Pixels were binned 2×2 pixels giving a plate scale of 0.98 arcsec/pixel. We obtained 3–6 exposures of 180 s per target. The images were reduced in the standard way of subtracting the bias and dark frames and dividing by twilight flat-fields. The fluxes of the target and 3–5 stars in the target field were measured with aperture photometry and the magnitude difference between the target and a primary reference star in the same field was determined. The use of differential mode makes the observations insensitive to variations in atmospheric transparency and accurate measurements can be obtained even in partially cloudy conditions. The *R*-band magnitude of the primary reference star was determined from observations made on photometric nights, using comparison stars in known blazar fields as calibrators (Fiorucci & Tosti 1996; Fiorucci et al. 1998; Raiteri et al. 1998; Villata et al. 1998; Nilsson et al. 2007) and taking into account the color term of the *R*-band filter employed. After the *R*-band magnitude of the primary reference star was determined, the object magnitudes were computed from the magnitude differences. At this phase we assumed $V - R = 0.5$ for the targets. Several stars in the field were used to check the quality of the photometry and stability of the primary reference. The uncertainties in the magnitudes include the contribution from both measurement and calibration errors.

3.1.11. Xinglong

The monitoring at Xinglong Station, National Astronomical Observatories of China, was performed with a 60/90 cm

$f/3$ Schmidt telescope. The telescope is equipped with a 4096×4096 E2V CCD, which has a pixel size of $12\,\mu$m and a spatial resolution of $1\farcs3$ pixel^{-1} . The observations were made with an intermediate-band filter, the *I* filter. Its central wavelength and passband width are 6685 Å and 514 Å, respectively. The exposure times were mostly 120 s but ranged from 60 s to 180 s, depending on weather and lunar phase.

3.2. Planck microwave data

Planck (Tauber et al. 2010; Planck Collaboration 2011a) is the third generation space mission to measure the anisotropy of the cosmic microwave background (CMB). It observes the sky in nine frequency bands covering 30–857 GHz with high sensitivity and angular resolution from $31'$ to $5'$. Full sky coverage is attained in about seven months. The Low Frequency Instrument (LFI; Mandolesi et al. 2010; Bersanelli et al. 2010; Mennella et al. 2011) covers the 30, 44, and 70 GHz bands with amplifiers cooled to 20 K. The High Frequency Instrument (HFI; Lamarre et al. 2010; Planck HFI Core Team 2011a) covers the 100, 143, 217, 353, 545, and 857 GHz bands with bolometers cooled to 0.1 K. Polarization is measured in all but the highest two bands (Leahy et al. 2010; Rosset et al. 2010). A combination of radiative cooling and three mechanical coolers produces the temperatures needed for the detectors and optics (Planck Collaboration 2011b). Two data processing centers (DPCs) check and calibrate the data and make maps of the sky (Planck HFI Core Team 2011b; Zacchei et al. 2011). *Planck*'s sensitivity, angular resolution, and frequency coverage make it a powerful instrument for Galactic and extragalactic astrophysics as well as cosmology. Early astrophysics results are given in Planck Collaboration (2011h–z).

The Early Release Compact Source Catalog (ERCSC, Planck Collaboration 2011c) contains all sources, both Galactic and extragalactic, detected with high confidence over the full sky during the period between August 12, 2009 and June 6, 2010 (corresponding to *Planck* operational days 91 to 389). The ERCSC only contains average intensity information for the sources. However, many of the sources were observed more than once during the time period spanned by the ERCSC, and some of the *Swift* observations used for this paper were carried out between June and October 2010. Therefore, to have simultaneous data, we produced independent maps for the first (OD 91–274), the second (OD 275–456), and the beginning of the third *Planck* survey (OD 457–550) through the LFI and HFI pipelines described in Zacchei et al. (2011) and Planck HFI Core Team (2011b), and we extracted the flux densities from each map using IFACMEX, which is an implementation of the Mexican Hat Wavelet 2 (MHW2) algorithm available at the LFI DPC. The MHW2 tool has been extensively used to detect point-like objects in astronomical images, both with simulations from various experiments and data from the WMAP, *Planck*, and Herschel satellites (González-Nuevo et al. 2006; López-Caniego et al. 2006, 2007; Massardi et al. 2009). This wavelet is defined as the fourth derivative of the two-dimensional Gaussian function, where the scale of the filter *R* is optimized to look for the maximum in the S/N of the sources in the filtered map. In practice, the IFCAMEX code, our implementation of the MHW algorithm, deals with flexible image transport system (FITS) maps in Healpix format (Górski et al. 2005) and can be used to detect sources in the whole sky or at the position of known objects. For this analysis, we looked for objects above the 4σ level at the positions corresponding to the 105 sources of our sample. For objects with S/N smaller than four we adopted the 4σ level as an upper limit. The results of the analysis of *Planck* simultaneous data are reported in Table 8, where Cols. 1 and 2 give the source name, Cols. 3 and 4 give the observation start and end times, and Cols. 5–13 give the flux densities in units of Jy at 30, 44, 70, 100, 143, 217, 353, 545, and 857 GHz.

Owing to source variability, we do not expect these simultaneous flux densities to be the same as the time-averaged ERCSC measurements, except in the case of the sources that were observed only once during the ERCSC time range and for which we estimated the *Planck* flux densities, measured simultaneously with the *Swift* observation, in the same period. We verified that, for the sources fulfilling these requirements, the flux densities extracted for this paper are in good agreement with those of the ERCSC.

In addition to simultaneous *Planck* data, we also used ERCSC flux densities in both our analysis of flux correlations (Sect. 7.2) and the SED plots described in Sect. 5.

3.3. Swift optical, UV, and X-ray data

The *Swift* Gamma-Ray-Burst (GRB) Explorer (Gehrels et al. 2004) is a multi-frequency space observatory devoted to the discovery and rapid follow-up of GRBs. There are three instruments on board the spacecraft: the UV and Optical Telescope (UVOT, Roming et al. 2005), the X-Ray Telescope (XRT, Burrows et al. 2005) sensitive to the 0.3–10.0 keV band, and the Burst Alert Telescope (BAT, Barthelmy et al. 2005) sensitive to the 15−150 keV band. Although the primary scientific goal of the satellite is the observation of GRBs, the wide frequency coverage is suitable for blazar studies, because it covers the region where the transition between synchrotron and inverse Compton emission usually occurs.

When not engaged in GRB observations, *Swift* is available for target of opportunity (ToO) requests, and the *Swift* team decided to devote an average of three ToO observations per week to this project for simultaneous observations of blazars.

3.3.1. UVOT

The *Swift* UVOT telescope can produce images in each of its six lenticular filters (*V*, *B*, *U*, *UVW*1, *UVM*2, and *UVW*2). However, in an effort to reduce the use of mechanical parts after several years of orbital operations, observations are carried out using only one filter, unless specifically requested by the user. Thus images are not always available for all filters.

The photometry analysis of all our sources was performed using the standard UVOT software distributed within the HEAsoft 6.8.0 package and the calibration included in the latest release of the "Calibration Database". A specific procedure was developed at the ASI Science Data Center (ASDC) to process all ToO observations requested for the blazar sample. Counts were extracted from apertures of $5''$ radius for all filters and converted to fluxes using the standard zero points (Poole et al. 2008). The fluxes were then de-reddened using the appropriate values of $E(B-V)$ for each source taken from Schlegel et al. (1998) with $A_\lambda/E(B-V)$ ratios calculated for UVOT filters using the mean Galactic interstellar extinction curve from Fitzpatrick (1999). No variability was detected within single exposures in any filter. The processing results were carefully validated including checks for possible contamination by nearby objects within the source and background apertures. Some sources, such as 3C 273 and NGC 1275, needed special analysis, and results for some other sources had to be discarded.

Table 8. *Planck* data integrated over a single survey during the *Swift* observations.

J2000.0 name	Source name	Start Obs. date	End Obs. Date	Flux density 30 GHz (Jy)	Flux density 44 GHz (Jy)	Flux density 70 GHz (Jy)	Flux density 100 GHz (Jy)	Flux density 143 GHz (Jy)	Flux density 217 GHz (Jy)	Flux density 353 GHz (Jy)	Flux density 545 GHz (Jy)	Flux density 857 GHz (Jy)
0010+1058	III ZW 2	2010-07-04	2010-07-13	2.59 ± 0.13	2.56 ± 0.21	1.74 ± 0.20	1.58 ± 0.08	1.09 ± 0.05	0.73 ± 0.05	0.54 ± 0.11	1.02 ± 0.20	<1.55
0017+8135	S5 0014+813	2010-09-18	2010-10-01	<0.53	<0.74	<0.64	<0.34	<0.20	<0.19	<1.43	<1.75	<3.17
0035+5950	1ES 0033+595	2010-01-25	2010-02-02	<0.71	<1.14	<0.81	<0.33	<0.19	<0.33	<0.91	<3.28	<8.48
0048+3157	Mkn 348	2010-01-14	2010-01-21	<0.69	<1.04	<0.70	<0.34	<0.22	0.24 ± 0.05	<0.51	<1.04	<0.88
0120−2701	1Jy 0118−272	2009-12-15	2009-12-27	0.75 ± 0.13	<0.88	<0.71	0.65 ± 0.08	0.40 ± 0.05	0.38 ± 0.05	0.41 ± 0.08	<0.59	<0.62
0136+4751	S4 0133+47	2010-01-29	2010-02-05	4.33 ± 0.15	3.80 ± 0.23	3.48 ± 0.17	3.24 ± 0.07	2.40 ± 0.05	2.02 ± 0.04	1.66 ± 0.09	1.45 ± 0.16	<1.03
0204−1701	PKS 0202−17	2010-01-08	2010-01-18	0.91 ± 0.13	<0.89	0.72 ± 0.17	0.58 ± 0.09	0.37 ± 0.05	0.18 ± 0.04	<0.51	<1.04	<1.72
0210−5101	PKS 0208−512	2009-11-23	2009-12-07	2.06 ± 0.12	2.28 ± 0.20	1.94 ± 0.15	1.48 ± 0.07	1.09 ± 0.05	0.78 ± 0.04	0.48 ± 0.08	<0.49	<0.52
0214+5144	GB6J 0214+5145	2010-02-05	2010-02-11	<0.54	<0.85	<0.81	<0.35	<0.17	<0.19	<0.51	<1.04	<1.72
0217+7349	1Jy 0212+735	2010-09-11	2010-09-21	2.84 ± 0.15	2.05 ± 0.21	1.67 ± 0.18	1.30 ± 0.09	0.82 ± 0.06	0.64 ± 0.08	<1.43	<2.15	<3.17
0217+0144	PKS 0215+015	2010-01-22	2010-01-29	1.99 ± 0.14	1.82 ± 0.26	1.92 ± 0.19	1.79 ± 0.11	1.33 ± 0.05	1.23 ± 0.06	0.98 ± 0.09	0.74 ± 0.16	<0.76
0221+3556	1Jy 0218+357	2010-08-16	2010-08-23	1.13 ± 0.13	0.94 ± 0.22	<0.67	0.70 ± 0.10	0.48 ± 0.06	0.37 ± 0.05	0.45 ± 0.11	<1.75	<0.85
0237+2848	4C 28.07	2010-02-03	2010-02-09	2.07 ± 0.14	2.11 ± 0.25	1.54 ± 0.16	1.38 ± 0.08	0.95 ± 0.05	0.59 ± 0.05	0.49 ± 0.09	<0.73	<1.72
0238+1636	PKS 0235+164	2010-02-01	2010-02-07	1.14 ± 0.15	1.21 ± 0.25	1.47 ± 0.19	1.47 ± 0.08	1.05 ± 0.05	0.82 ± 0.05	0.63 ± 0.08	<0.59	<1.08
0319+4130	NGC 1275	2010-08-29	2010-09-04	16.51 ± 0.18	13.27 ± 0.27	9.76 ± 0.26	9.12 ± 0.11	6.75 ± 0.07	4.86 ± 0.09	3.25 ± 0.14	2.67 ± 0.22	2.09 ± 0.30
0334−4008	PKS 0332−403	2010-01-11	2010-02-02	2.16 ± 0.18	2.06 ± 0.20	1.40 ± 0.17	1.52 ± 0.07	1.24 ± 0.04	0.82 ± 0.03	0.65 ± 0.06	0.71 ± 0.11	<0.51
0336+3218	NRAO 140	2010-08-28	2010-09-03	2.08 ± 0.23	2.15 ± 0.31	1.78 ± 0.25	1.46 ± 0.15	1.19 ± 0.09	0.73 ± 0.11	<1.43	<1.75	<3.17
0423−0120	PKS 0420−01	2009-08-28	2009-09-03	7.54 ± 0.18	7.61 ± 0.30	6.04 ± 0.23	6.00 ± 0.11	5.16 ± 0.06	3.69 ± 0.08	2.57 ± 0.14	2.31 ± 0.25	1.84 ± 0.41
0428−3756	PKS 0426−380	2010-08-16	2010-08-26	2.91 ± 0.13	2.67 ± 0.21	1.97 ± 0.19	1.09 ± 0.09	0.96 ± 0.06	0.65 ± 0.05	0.57 ± 0.08	<0.64	<0.65
0433+0521	3C 120	2010-02-24	2010-03-01	2.57 ± 0.15	2.04 ± 0.29	1.35 ± 0.21	1.63 ± 0.10	1.35 ± 0.07	0.83 ± 0.06	<0.55	<1.06	<1.98
0457−2324	PKS 0454−234	2010-02-27	2010-03-05	2.08 ± 0.16	1.96 ± 0.26	1.67 ± 0.21	1.44 ± 0.10	1.19 ± 0.05	0.80 ± 0.05	0.62 ± 0.12	0.72 ± 0.16	<0.71
0522−3627	PKS 0521−36	2010-03-03	2010-03-14	5.31 ± 0.14	4.61 ± 0.23	4.60 ± 0.18	4.70 ± 0.09	3.73 ± 0.05	3.33 ± 0.06	2.20 ± 0.10	2.34 ± 0.15	1.81 ± 0.21
0530+1331	PKS 0528+134	2009-09-15	2009-09-20	1.83 ± 0.24	2.19 ± 0.32	1.29 ± 0.21	1.15 ± 0.14	0.87 ± 0.08	0.60 ± 0.11	<0.51	<1.04	<1.72
0538−4405	PKS 0537−441	2010-03-07	2010-03-22	7.25 ± 0.17	6.78 ± 0.23	7.07 ± 0.17	6.95 ± 0.08	5.13 ± 0.04	4.68 ± 0.06	3.77 ± 0.10	3.37 ± 0.15	2.26 ± 0.29
0539−2839	1Jy 0537−286	2010-03-08	2010-03-19	1.17 ± 0.14	1.19 ± 0.24	<0.70	0.66 ± 0.09	0.37 ± 0.05	0.24 ± 0.05	<0.36	<0.57	<1.72
0550−3216	PKS 0548−322	2010-03-11	2010-03-22	<0.71	<1.04	<0.81	<0.37	<0.19	<0.21	<0.48	<0.57	<0.87
0623−6436	IRAS-L 06229−643	2010-08-13	2010-09-09	0.87 ± 0.09	1.40 ± 0.21	0.67 ± 0.08	0.47 ± 0.05	<0.21	<0.19	<1.43	<1.75	<3.17
0738+1742	PKS 0735+17	2010-10-10	2010-10-17	0.89 ± 0.15	<1.09	<0.88	<0.31	<0.21	<0.19	<1.43	<1.75	<3.17
0746+2549	B2.2 0743+25	2010-10-11	2010-10-17	<0.72	<1.07	<0.81	<0.31	<0.21	<0.19	<1.43	<1.75	<3.17
0818+4222	S4 0814+425	2010-10-15	2010-10-21	1.82 ± 0.17	1.39 ± 0.27	<0.86	<0.31	<0.21	<0.19	<1.43	<1.75	<3.17
0824+5552	OJ 535	2010-03-26	2010-04-03	<0.66	<1.06	<0.81	<0.34	0.30 ± 0.05	<0.23	<0.48	<0.89	<0.87
0841+7053	4C 71.07	2010-03-16	2010-03-27	2.84 ± 0.15	3.25 ± 0.27	2.52 ± 0.21	3.08 ± 0.09	2.09 ± 0.05	1.40 ± 0.05	0.95 ± 0.09	0.76 ± 0.13	<0.70
0854+2006	PKS 0851+202	2010-04-15	2010-04-22	8.48 ± 0.16	8.60 ± 0.31	8.11 ± 0.23	3.54 ± 0.10	2.93 ± 0.06	2.24 ± 0.05	1.81 ± 0.12	1.80 ± 0.15	1.38 ± 0.20
0915+2933	B2 0912+29	2010-10-28	2010-11-04	<0.66	<1.04	<0.81	<0.31	<0.21	<0.19	<1.43	<1.75	<3.17
0920+4441	S4 0917+44	2009-10-25	2009-11-01	2.55 ± 0.16	2.09 ± 0.26	1.89 ± 0.21	1.84 ± 0.09	1.51 ± 0.06	1.16 ± 0.05	0.91 ± 0.09	0.88 ± 0.18	0.84 ± 0.18
0923−2135	PKS 0921−213	2010-05-04	2010-05-12	<0.53	<0.90	<0.60	<0.37	0.30 ± 0.05	0.26 ± 0.05	0.42 ± 0.10	<0.89	<0.87
0957+5522	4C 55.17	2009-10-26	2009-11-03	1.22 ± 0.15	<1.04	<0.77	0.51 ± 0.09	0.39 ± 0.05	0.27 ± 0.05	<0.38	<1.04	<0.85
1015+4926	1H 1013+498	2010-04-18	2010-04-28	<0.71	<1.04	<0.81	<0.30	<0.19	<0.17	<0.48	<0.89	<0.87
1058+5628	1RXSJ 105837.5+562816	2010-04-19	2010-05-03	<0.65	<1.02	<0.77	<0.37	<0.19	<0.16	<0.48	<0.89	<0.87
1058+0133	4C 01.28	2009-12-07	2009-12-16	6.07 ± 0.14	5.64 ± 0.23	4.51 ± 0.17	4.19 ± 0.08	3.25 ± 0.05	2.55 ± 0.05	1.63 ± 0.09	1.37 ± 0.14	0.98 ± 0.17
1058−8003	PKS 1057−79	2010-08-27	2010-09-13	2.05 ± 0.14	2.14 ± 0.21	1.81 ± 0.16	1.86 ± 0.08	1.21 ± 0.04	0.74 ± 0.04	0.56 ± 0.08	<0.58	<3.17
1104+3812	Mkn 421	2009-11-15	2009-11-24	<0.52	<1.04	<0.81	0.40 ± 0.09	<0.24	<0.23	<0.51	<1.04	<1.72
1127−1857	PKS 1124−186	2010-06-10	2010-06-20	1.63 ± 0.14	1.39 ± 0.26	0.86 ± 0.20	1.18 ± 0.09	0.97 ± 0.04	0.79 ± 0.04	0.74 ± 0.10	<0.65	<0.96
1130−1449	PKS 1127−145	2009-12-27	2010-01-04	3.58 ± 0.14	3.38 ± 0.28	2.83 ± 0.19	2.49 ± 0.08	1.77 ± 0.05	1.20 ± 0.05	0.97 ± 0.10	0.89 ± 0.15	0.81 ± 0.17
1131+3114	B2 1128+31	2009-11-26	2009-12-05	<0.71	<1.04	<0.81	<0.34	<0.19	<0.21	<0.51	<1.04	<1.72
1136+7009	S5 1133+704	2009-10-27	2009-11-05	<0.71	<1.04	<0.73	<0.35	<0.22	<0.21	<0.51	<1.04	<1.72
1147−3812	PKS 1144−379	2010-06-25	2010-07-08	1.29 ± 0.15	<1.10	0.99 ± 0.19	1.91 ± 0.08	1.53 ± 0.04	1.29 ± 0.05	1.04 ± 0.09	0.85 ± 0.16	<0.77
1153+4931	4C 49.22	2009-11-16	2009-11-26	1.03 ± 0.15	1.23 ± 0.25	0.96 ± 0.20	0.70 ± 0.09	0.51 ± 0.05	0.29 ± 0.06	<0.51	<1.04	<1.72
1159+2914	4C 29.45	2010-05-31	2010-06-11	1.35 ± 0.14	1.41 ± 0.22	0.80 ± 0.16	1.53 ± 0.08	1.24 ± 0.05	0.99 ± 0.04	0.77 ± 0.09	0.84 ± 0.14	<0.60
1217+3007	ON 325	2009-12-08	2009-12-19	0.55 ± 0.13	<1.04	<0.72	<0.32	<0.19	0.20 ± 0.05	<0.33	<0.60	<0.68
1220+0203	PKS 1217+02	2010-06-20	2010-06-29	<2.18	<1.04	<1.96	0.59 ± 0.08	0.39 ± 0.05	0.24 ± 0.04	<0.48	<0.89	<0.87
1221+2813	ON 231	2009-12-11	2009-12-22	<0.50	<0.88	<0.67	0.34 ± 0.08	0.30 ± 0.05	0.25 ± 0.04	<0.32	<0.54	<1.72
1222+0413	PKS 1219+04	2010-06-20	2010-06-29	1.50 ± 0.35	<1.85	<1.04	0.94 ± 0.08	0.64 ± 0.05	0.58 ± 0.05	<0.52	<0.89	<0.87

Table 8. continued.

J2000.0 name	Source name	Start Obs. date	End Obs. Date	Flux density 30 GHz (Jy)	Flux density 44 GHz (Jy)	Flux density 70 GHz (Jy)	Flux density 100 GHz (Jy)	Flux density 143 GHz (Jy)	Flux density 217 GHz (Jy)	Flux density 353 GHz (Jy)	Flux density 545 GHz (Jy)	Flux density 857 GHz (Jy)
1229+0203	3C 273	2010-01-02	2010-01-10	24.49 ± 0.43	27.88 ± 0.69	20.58 ± 0.45	21.56 ± 0.11	16.09 ± 0.06	9.51 ± 0.10	6.74 ± 0.14	5.72 ± 0.16	3.99 ± 0.17
1246−2547	PKS 1244−255	2010-01-20	2010-01-26	1.02 ± 0.15	1.22 ± 0.27	1.37 ± 0.19	1.25 ± 0.10	1.08 ± 0.06	0.82 ± 0.06	0.83 ± 0.12	<1.04	<1.00
1248+5820	PG 1246+586	2010-05-12	2010-06-03	<0.71	<1.04	<0.81	<0.37	<0.15	<0.13	<0.48	<0.89	<0.87
1256−0547	3C 279	2010-01-13	2010-01-20	14.36 ± 0.17	14.27 ± 0.31	11.77 ± 0.22	11.96 ± 0.10	9.06 ± 0.06	7.13 ± 0.10	5.45 ± 0.15	4.79 ± 0.17	2.77 ± 0.18
1305−1033	1Jy 1302−102	2010-01-17	2010-01-24	<0.59	<1.02	<0.82	<0.38	0.36 ± 0.06	0.31 ± 0.06	<0.41	<0.74	<1.72
1310+3220	1Jy 1308+326	2009-12-21	2010-01-03	3.64 ± 0.14	3.05 ± 0.25	1.92 ± 0.15	1.81 ± 0.08	1.34 ± 0.05	0.92 ± 0.05	0.73 ± 0.08	0.66 ± 0.12	<0.63
1350+0940	GB6B 1347+0955	2010-07-14	2010-07-22	<0.71	<1.04	<0.81	<0.37	<0.19	<0.21	<0.48	<0.89	<0.87
1407−2701	1WGAJ 1407.5−2700	2010-02-05	2010-02-11	<0.60	<1.04	<0.81	<0.39	<0.23	<0.21	<0.51	<0.70	<1.72
1419+0628	3C 298.0	2010-07-23	2010-07-30	<0.55	<0.98	<0.81	<0.37	<0.19	<0.21	<0.48	<0.89	<0.87
1423+5055	BZQJ 1423+5055	2010-06-24	2010-07-08	<0.50	<0.73	<0.58	0.37 ± 0.08	<0.17	<0.21	<0.48	<0.89	<0.87
1427+2348	PG 1424+240	2010-01-23	2010-02-02	<0.51	<1.04	<0.81	<0.35	0.21 ± 0.05	<0.21	<0.40	<0.70	<1.09
1456+5048	1RXSJ 145603.4+504825	2009-12-26	2010-01-26	<0.71	<1.04	<0.45	<0.35	<0.19	<0.21	<0.20	<0.37	<0.46
1504+1029	PKS 1502+106	2010-08-01	2010-08-07	1.16 ± 0.15	<1.04	0.87 ± 0.18	0.65 ± 0.09	0.40 ± 0.04	0.30 ± 0.05	<0.31	<0.89	<0.87
1507+0415	BZQJ1507+0415	2010-08-04	2010-08-10	<0.71	<1.04	<0.81	<0.31	<0.21	<0.19	<1.43	<1.75	<3.17
1510−0543	4C −05.64	2010-02-13	2010-02-19	0.96 ± 0.17	<1.04	1.05 ± 0.22	<0.35	<0.19	<0.21	<0.51	<1.04	<1.72
1517−2422	AP Lib	2010-02-17	2010-02-23	2.21 ± 0.16	2.21 ± 0.28	1.91 ± 0.24	1.83 ± 0.10	1.54 ± 0.06	1.22 ± 0.06	1.19 ± 0.12	1.21 ± 0.18	1.39 ± 0.25
1555+1111	PG 1553+113	2010-02-21	2010-02-28	<0.71	<1.04	<0.82	<0.35	<0.19	<0.22	<0.51	<1.04	<1.72
1603+1554	WE 1601+16W3	2010-08-12	2010-08-18	<0.71	<1.04	<0.81	<0.31	<0.21	<0.19	<1.43	<1.75	<3.17
1625−2527	OS −237.8	2010-08-28	2010-09-03	2.69 ± 0.39	<1.81	1.48 ± 0.31	1.46 ± 0.20	0.90 ± 0.11	0.78 ± 0.15	<1.52	<6.34	<17.5
1635+3808	4C 38.41	2010-03-02	2010-03-12	3.43 ± 0.26	<1.04	2.95 ± 0.21	<0.35	<0.19	<0.21	<0.51	<1.04	<1.72
1640+3946	NRAO 512	2010-08-07	2010-08-16	<0.71	<1.04	<0.81	<0.69	0.52 ± 0.09	<0.55	<0.38	<0.89	<0.87
1642+3948	3C 345	2010-03-04	2010-03-17	9.10 ± 0.18	<1.04	6.26 ± 0.21	5.75 ± 0.08	<0.19	<0.21	<0.51	<1.04	<1.72
1653+3945	Mkn 501	2010-03-07	2010-03-21	<1.37	<1.04	<0.73	0.57 ± 0.08	0.47 ± 0.04	0.31 ± 0.04	0.35 ± 0.06	<0.44	<0.55
1719+4858	ARP 102B	2010-03-20	2010-03-31	<0.71	<1.04	<0.81	0.33 ± 0.07	0.16 ± 0.04	<0.14	<0.25	<0.89	<0.56
1743+1935	1ES 1741+196	2010-03-20	2010-03-27	<0.71	<1.04	<0.81	<0.35	<0.19	<0.21	<0.51	<1.04	<1.72
1751+0939	OT 081	2010-03-21	2010-03-27	6.46 ± 0.16	5.82 ± 0.28	5.05 ± 0.22	3.72 ± 0.08	2.78 ± 0.06	2.44 ± 0.07	1.68 ± 0.13	1.68 ± 0.21	<1.42
1800+7828	S5 1803+784	2009-10-11	2009-10-27	2.28 ± 0.13	2.14 ± 0.17	1.49 ± 0.15	1.78 ± 0.06	1.43 ± 0.03	1.22 ± 0.03	1.03 ± 0.06	0.99 ± 0.10	0.58 ± 0.14
1833−2103	PKSB 1830−210	2010-09-20	2010-09-26	4.11 ± 0.33	3.42 ± 0.36	2.44 ± 0.22	2.47 ± 0.11	1.64 ± 0.07	1.18 ± 0.08	0.79 ± 0.17	<1.63	<3.17
1840−7709	PKS 1833−77	2010-03-12	2010-03-24	<0.71	<1.04	<0.81	<0.35	<0.19	<0.21	<0.51	<1.04	<1.72
1911−2006	2E 1908.2−201	2009-09-28	2009-10-03	2.88 ± 0.19	3.02 ± 0.33	2.34 ± 0.21	2.02 ± 0.11	1.74 ± 0.06	1.33 ± 0.06	0.86 ± 0.12	1.02 ± 0.18	1.22 ± 0.30
1923−2104	PMNJ 1923−2104	2010-09-30	2010-10-06	2.22 ± 0.19	2.71 ± 0.28	2.43 ± 0.24	<0.31	1.49 ± 0.05	1.19 ± 0.07	0.95 ± 0.12	0.90 ± 0.19	<1.28
1924−2914	OV −236	2010-09-30	2010-10-06	16.48 ± 0.16	13.80 ± 0.30	11.61 ± 0.24	<0.31	5.82 ± 0.06	4.46 ± 0.08	3.27 ± 0.11	3.18 ± 0.21	1.67 ± 0.35
1959+6508	1ES 1959+650	2009-09-16	2010-01-14	<0.71	<1.04	<0.81	<0.35	<0.12	<0.11	<0.51	<0.83	<2.18
2009−4849	1Jy 2005−489	2009-10-05	2009-10-11	<0.67	<1.13	<0.98	0.76 ± 0.10	0.46 ± 0.06	0.37 ± 0.06	0.42 ± 0.10	<1.04	<0.75
2056−4714	PKS 2052−47	2010-10-12	2010-10-19	2.15 ± 0.15	2.27 ± 0.30	1.68 ± 0.20	<0.31	<0.21	<0.19	<1.43	<1.75	<3.17
2129−1538	1Jy 2126−158	2010-05-03	2010-05-11	<0.62	<1.04	<0.81	<0.34	<0.21	<0.21	<0.48	<0.89	<0.87
2143+1743	S3 2141+17	2009-11-14	2009-11-25	1.31 ± 0.16	<0.89	<0.76	0.40 ± 0.09	0.39 ± 0.04	0.26 ± 0.05	<0.51	<1.04	<1.72
2147+0929	1Jy 2144+092	2009-11-11	2009-11-21	1.01 ± 0.22	1.15 ± 0.27	0.78 ± 0.19	0.86 ± 0.09	0.67 ± 0.05	0.58 ± 0.05	0.76 ± 0.10	<0.78	<1.72
2148+0657	4C 06.69	2009-11-10	2009-11-19	5.32 ± 0.16	4.85 ± 0.24	3.23 ± 0.19	2.85 ± 0.08	2.14 ± 0.05	1.43 ± 0.05	1.15 ± 0.10	0.76 ± 0.18	<1.01
2151−3027	PKS 2149−307	2010-05-04	2010-05-13	0.82 ± 0.14	1.03 ± 0.25	<0.81	0.67 ± 0.08	0.42 ± 0.05	0.36 ± 0.05	0.34 ± 0.07	<0.52	<0.87
2202+4216	BL Lac	2009-12-13	2009-12-26	4.01 ± 0.15	3.71 ± 0.22	3.23 ± 0.17	3.13 ± 0.08	2.69 ± 0.05	1.97 ± 0.07	1.81 ± 0.18	<2.16	<1.72
2203+3145	4C 31.63	2009-12-02	2009-12-15	2.90 ± 0.13	2.52 ± 0.23	2.69 ± 0.15	2.59 ± 0.08	2.00 ± 0.05	1.39 ± 0.04	1.02 ± 0.08	0.90 ± 0.15	<1.72
2207−5346	PKS 2204−54	2010-04-26	2010-05-08	0.92 ± 0.14	1.03 ± 0.24	<0.81	0.61 ± 0.08	0.46 ± 0.04	0.41 ± 0.04	<0.31	<0.51	<0.87
2209−4710	NGC 7213	2010-10-23	2010-10-30	<0.71	<1.00	<0.81	<0.31	<0.21	<0.19	<1.43	<1.75	<3.17
2229−0832	PKS 2227−08	2009-11-14	2009-11-22	1.69 ± 0.20	1.79 ± 0.28	2.06 ± 0.21	1.48 ± 0.09	1.29 ± 0.05	0.94 ± 0.04	0.77 ± 0.10	<0.62	<0.71
2230−3942	PKS 2227−399	2010-05-10	2010-05-22	0.71 ± 0.16	<0.97	0.95 ± 0.17	0.49 ± 0.08	0.29 ± 0.05	<0.20	0.31 ± 0.08	<0.89	<0.87
2232+1143	4C 11.69	2009-11-27	2009-12-07	4.53 ± 0.13	3.85 ± 0.26	2.79 ± 0.16	2.15 ± 0.09	1.57 ± 0.05	1.09 ± 0.05	0.73 ± 0.10	<0.63	<0.83
2253+1608	3C 454.3	2009-12-06	2009-12-16	17.11 ± 0.17	21.90 ± 0.27	25.40 ± 0.29	27.28 ± 0.13	25.39 ± 0.08	22.04 ± 0.19	19.29 ± 0.24	19.41 ± 0.20	13.89 ± 0.28
2303−1842	PKS 2300−18	2010-05-30	2010-06-09	0.74 ± 0.17	<1.06	<1.02	<0.37	<0.20	<0.18	<0.34	<0.51	<0.60
2327+0940	PKS 2325+093	2010-06-19	2010-06-29	1.48 ± 0.16	1.22 ± 0.25	0.75 ± 0.17	0.65 ± 0.08	0.61 ± 0.05	0.41 ± 0.05	<0.48	<0.89	<0.87
2333−2343	PKS 2331−240	2010-06-08	2010-06-18	1.21 ± 0.14	1.09 ± 0.26	0.93 ± 0.20	0.97 ± 0.08	1.01 ± 0.05	0.90 ± 0.05	0.50 ± 0.09	0.60 ± 0.14	<0.62
2347+5142	1ES 2344+514	2010-01-13	2010-01-22	<0.56	<0.98	<0.81	<0.34	<0.20	<0.22	<0.51	<1.04	<1.72

Notes. Columns 1 and 2: source name; Cols. 3 and 4: observation start and end times; Cols. 5–13: flux densities in units of Jy at 30, 44, 70, 100, 143, 217, 353, 545, and 857 GHz.

The results of the UVOT data analysis are summarized in Table 9, where Cols. 1 and 2 give the source name, Cols. 3 and 4 give the observation date and the *Swift* observation ID, and the remaining columns give the magnitudes in the six UVOT filters with errors.

3.3.2. XRT

The *Swift* XRT is usually operated in "auto-state" mode, which automatically adjusts the CCD read-out mode to the source brightness, in an attempt to avoid pile-up (Burrows et al. 2005; Hill et al. 2004). As a consequence, some of the data were collected using the most sensitive photon counting (PC) mode, while windowed timing (WT) mode was used for bright sources.

The XRT data were processed with the XRTDAS software package (v. 2.5.1, Capalbi et al. 2005) developed at the ASI Science Data Center (ASDC) and distributed by the NASA High Energy Astrophysics Archive Research Center (HEASARC) within the HEASoft package (v. 6.9). Event files were calibrated and cleaned with standard filtering criteria using the *xrtpipeline* task and the latest calibration files available in the *Swift* CALDB. Events in the energy range 0.3–10 keV with grades 0−12 (PC mode) and 0–2 (WT mode) were used for the analysis.

Events for the spectral analysis were selected within a circle of 20 pixels (~47″) radius, which encloses about 90% of the point spread function (PSF) at 1.5 keV (Moretti et al. 2005), centered on the source position. When the source count rate is above ~0.5 counts/s, the PC mode data are significantly affected by pile-up in the inner part of the PSF. In these cases, and after comparing the observed PSF profile with the analytical model derived by Moretti et al. (2005), we removed pile-up effects by excluding events detected within up to 6 pixels from the source position, and used an outer radius of 30 pixels. The value of the inner radius was evaluated individually for each observation affected by pile-up, in a way that depended on the observed source count rate.

Ancillary response files were generated with the *xrtmkarf* task by applying corrections for the PSF losses and CCD defects. Source spectra were binned to ensure a minimum of 20 counts per bin when utilizing the χ^2 minimization fitting technique. We fitted the spectra adopting an absorbed power-law model with photon index Γ_x. When deviations from a single power-law model were found, we adopted a log-parabolic law of the form $F(E) = KE^{(a+b\log E)}$ (Massaro et al. 2004), which has been shown to fit the X-ray spectrum of blazars of the HSP type well (e.g. Giommi et al. 2005; Tramacere et al. 2009). This spectral model is described by only two parameters: a, the photon index at 1 keV, and b, the curvature of the parabola. For both models, the amount of hydrogen-equivalent column density ($N_{\rm H}$) was fixed to the Galactic value along the line of sight (Kalberla et al. 2005). For a fraction of the sources fitted with a power-law model (~15%), we found evidence of an absorption excess at low energies and the hydrogen column density $N_{\rm H}$ parameter was left free.

The results of the spectral fits with a power-law model and Galactic $N_{\rm H}$ are shown in Table 10, where Cols. 1 and 2 give the source name, Col. 3 gives the *Swift* observation date, Col. 4 gives the best-fit photon index Γ_x, Col. 5 gives the Galactic $N_{\rm H}$, Cols. 6 and 7 give the 0.1–2.4 and 2–10 keV X-ray fluxes, Col. 8 gives the value of the reduced χ^2, and Col. 9 gives the number of degrees of freedom.

In Table 11, we report data obtained using a log-parabola to describe the spectrum model. Columns 1 and 2 give the source name, Col. 3 gives the *Swift* observation date, Cols. 4 and 5 give the log parabola parameters a and b, Col. 6 gives the Galactic $N_{\rm H}$, Cols. 7 and 8 give the 0.1–2.4 and 2–10 keV X-ray fluxes, Col. 9 gives the value of the reduced χ^2, and Col. 10 gives the number of degrees of freedom.

Finally, in Table 12 we report the results of the spectral fits that were performed leaving the hydrogen column density $N_{\rm H}$ to vary as a free parameter. Columns 1 and 2 give the source name, Col. 3 gives the *Swift* observation date, Col. 4 gives the best-fit photon index Γ_x, Col. 5 gives the estimated $N_{\rm H}$, Cols. 6 and 7 give the 0.1–2.4 and 2–10 keV X-ray fluxes, Col. 8 gives the value of the reduced χ^2, and Col. 9 gives the number of degrees of freedom.

3.4. *Fermi*-LAT γ-ray data

The Large Area Telescope (LAT) on-board *Fermi* is an electron-positron pair conversion telescope sensitive to γ-rays of energies from 20 MeV to >300 GeV. The *Fermi*-LAT consists of a high-resolution silicon microstrip tracker, a CsI hodoscopic electromagnetic calorimeter, and an anticoincidence detector for charged particle background identification. A full description of the instrument and its performance can be found in Atwood et al. (2009). The large field of view (~2.4 sr) allows the LAT to observe the full sky in survey mode every 3 h. The LAT point spread function (PSF) depends strongly on both the energy and the conversion point in the tracker, but less on the incidence angle.

The LAT γ-ray spectra of all AGN sources are studied in Abdo et al. (2010b) based on 11 months of *Fermi*-LAT data. Here we derived the γ-ray spectra of the blazars for which we built the simultaneous SEDs, integrating for two weeks encompassing the whole duration of the *Planck* observations.

The *Fermi*-LAT data considered for this analysis cover the period from August 4, 2008 to November 4, 2010 and were analyzed using the standard *Fermi*-LAT ScienceTools software package[7] (version v9r16) and selecting for each source only photons of energies above 100 MeV belonging to the diffuse class (Pass6 V3 IRF; Atwood et al. 2009), which have the lowest background contamination. For each source, we selected only photons within a 15° region of interest (RoI) centered around the source itself. To avoid background contamination from the bright Earth limb, time intervals where the Earth entered the LAT Field of View (FoV) were excluded from the data sample. In addition, we excluded observations in which the source under study was viewed at zenith angles larger than 105°, where Earth's atmospheric γ-rays increase the background contamination. The data were analyzed with a binned maximum likelihood technique (Mattox et al. 1996) using the analysis software *gtlike* developed by the LAT team[8]. A model accounting for the diffuse emission and nearby γ-ray sources was included in the fit.

The diffuse foreground, including Galactic interstellar emission, extragalactic γ-ray emission, and residual CR background, was modeled with *gll_iem_v02*[9] for the Galactic diffuse emission and isotropic_iem_v02 for the extragalactic isotropic emission. Each source under study was modeled with a power-law function

$$\frac{{\rm d}N}{{\rm d}E} = \frac{N(\Gamma+1)E^{\Gamma}}{E_{\rm max}^{\Gamma+1} - E_{\rm min}^{\Gamma+1}} \quad (1)$$

[7] http://fermi.gsfc.nasa.gov/ssc/data/analysis/documentation/Cicerone

[8] http://fermi.gsfc.nasa.gov/ssc/data/analysis/documentation/Cicerone/Cicerone_Likelihood

[9] http://fermi.gsfc.nasa.gov/ssc/data/access/lat/BackgroundModels.html

Table 9. *Swift*-UVOT data.

J2000.0 name	Source name	Obs. date	*Swift* ObsID	*V*	*B*	*U*	*UVW*1	*UVM*2	*UVW*2
0010+1058	III ZW 2	2010-07-08	00036363006	15.05 ± 0.02	...	...	14.22 ± 0.04	14.09 ± 0.04	13.99 ± 0.04
0010+1058	III ZW 2	2010-07-08	00036363007	...	...	...	...	...	14.01 ± 0.03
0017+8135	S5 0014+813	2010-09-21	00031816001	15.92 ± 0.03	16.80 ± 0.04	17.41 ± 0.07	...	...	...
0017+8135	S5 0014+813	2010-09-21	00031816002	...	...	17.45 ± 0.04	...	...	...
0017+8135	S5 0014+813	2010-09-22	00031816003	...	...	...	...	...	19.46 ± 0.32
0136+4751	S4 0133+47	2010-02-05	00036188007	...	...	16.89 ± 0.03	...	...	17.01 ± 0.05
0136+4751	S4 0133+47	2010-02-05	00036188008	17.23 ± 0.14	17.32 ± 0.10	16.75 ± 0.10	16.95 ± 0.11	16.75 ± 0.13	16.98 ± 0.09
0204−1701	PKS 0202−17	2010-01-08	00038366001	17.40 ± 0.06	17.40 ± 0.04	16.32 ± 0.04	16.35 ± 0.04	16.28 ± 0.04	16.44 ± 0.04
0210−5101	PKS 0208−512	2009-11-26	00035002044	17.94 ± 0.14	18.45 ± 0.10	17.22 ± 0.07	17.15 ± 0.08	16.79 ± 0.08	17.37 ± 0.07
0217+7349	1Jy 0212+735	2010-09-09	00035241004	...	...	...	...	<14.17	<13.89
0217+7349	1Jy 0212+735	2010-09-10	00035241005	16.95 ± 0.32	<16.81	<16.10	...	...	...
0221+3556	1Jy 0218+357	2010-08-20	00038096003	18.90	<19.96	<19.56	<19.79	<19.52	<20.17
0237+2848	4C 28.07	2010-02-05	00036189004	17.41 ± 0.21	17.92 ± 0.15	17.02 ± 0.11	17.19 ± 0.12	...	17.11 ± 0.09
0237+2848	4C 28.07	2010-02-05	00036189005	...	...	16.85 ± 0.03	...	...	...
0238+1636	PKS 0235+164	2010-01-30	00030880053	<18.19	<19.06	<18.66	<18.97	<18.94	<19.48
0319+4130	NGC 1275	2010-08-09	00031770010	13.34 ± 0.02	13.81 ± 0.02	13.27 ± 0.02	13.29 ± 0.03	13.04 ± 0.04	13.21 ± 0.03
0334−4008	PKS 0332−403	2010-01-17	00038372003	17.62 ± 0.07	18.09 ± 0.06	17.45 ± 0.05	17.71 ± 0.07	17.82 ± 0.07	18.69 ± 0.08
0336+3218	NRAO 140	2010-08-26	00036366004	...	...	...	...	10.80 ± 0.04	...
0336+3218	NRAO 140	2010-08-26	00036366005	14.99 ± 0.06	14.64 ± 0.05	13.27 ± 0.04	...	...	...
0423−0120	PKS 0420−01	2009-08-27	00036368006	...	...	...	...	15.42 ± 0.03	...
0428−3756	PKS 0426−380	2010-08-17	00041513005	17.75 ± 0.19	18.07 ± 0.10	17.34 ± 0.09	17.36 ± 0.09	17.22 ± 0.10	17.42 ± 0.08
0428−3756	PKS 0426−380	2010-08-17	00041513004	...	...	...	...	...	17.61 ± 0.04
0433+0521	3C 120	2010-02-25	00037594002	14.15 ± 0.03	...	13.19 ± 0.03	13.04 ± 0.04	12.78 ± 0.04	12.76 ± 0.04
0433+0521	3C 120	2010-02-25	00037594003	...	...	13.18 ± 0.02	...	...	...
0457−2324	PKS 0454−234	2010-02-25	00038101005	17.82 ± 0.15	18.32 ± 0.12	17.44 ± 0.10	17.50 ± 0.09	17.45 ± 0.11	17.74 ± 0.09
0457−2324	PKS 0454−234	2010-02-25	00038101006	...	...	17.36 ± 0.04	...	...	...
0457−2324	PKS 0454−234	2010-02-27	00038101007	...	...	...	...	17.34 ± 0.04	...
0522−3627	PKS 0521−36	2010-03-05	00031645001	14.88 ± 0.03	15.55 ± 0.03	14.98 ± 0.03	15.18 ± 0.04	15.08 ± 0.04	15.24 ± 0.04
0522−3627	PKS 0521−36	2010-03-08	00031645002	...	...	...	15.02 ± 0.03	...	...
0530+1331	PKS 0528+134	2009-09-24	00035384041	<16.62	<16.51	<15.72	<14.70	<12.17	<13.05
0538−4405	PKS 0537−441	2010-03-03	00030138029	14.44 ± 0.01	14.87 ± 0.02	14.09 ± 0.02	14.20 ± 0.03	14.09 ± 0.03	14.35 ± 0.03
0539−2839	1Jy 0537−286	2010-03-12	00030816009	<18.94	<19.88	<19.49	<19.73	<19.55	<20.21
0539−2839	1Jy 0537−286	2010-03-12	00030816010	...	...	20.68 ± 0.34	<20.61	...	...
0550−3216	PKS 0548−322	2010-03-12	00030836003	16.07 ± 0.06	16.91 ± 0.05	16.42 ± 0.05	16.43 ± 0.07	16.22 ± 0.07	16.38 ± 0.05
0550−3216	PKS 0548−322	2010-03-12	00030836004	...	...	16.46 ± 0.04	16.48 ± 0.03	...	...
0623−6436	IRAS-L 06229−643	2010-08-19	00030947008	15.42 ± 0.05	15.67 ± 0.04	14.41 ± 0.04	14.09 ± 0.04	13.70 ± 0.04	13.63 ± 0.04
0623−6436	IRAS-L 06229−643	2010-08-19	00030947009	...	...	...	14.10 ± 0.03	...	...
0738+1742	PKS 0735+17	2010-10-07	00036372003	...	16.54 ± 0.04	15.66 ± 0.04	15.72 ± 0.04	15.67 ± 0.04	15.81 ± 0.04
0738+1742	PKS 0735+17	2010-10-07	00036372004	...	...	15.70 ± 0.03	...	...	...
0738+1742	PKS 0735+17	2010-10-09	00036372005	...	...	...	...	15.67 ± 0.03	...

Table 9. continued.

J2000.0 name	Source name	Obs. date	*Swift* ObsID	*V*	*B*	*U*	*UVW1*	*UVM2*	*UVW2*
0746+2549	B2.2 0743+25	2010-10-15	00035422008	19.34 ± 0.24	<20.36	19.74 ± 0.23	...	...	...
0746+2549	B2.2 0743+25	2010-10-15	00035422009	...	...	20.06 ± 0.19	...	...	<20.82
0818+4222	S4 0814+425	2010-10-15	00038138002	17.88 ± 0.10	18.41 ± 0.07	17.68 ± 0.05	17.83 ± 0.07	17.77 ± 0.07	17.92 ± 0.06
0824+5552	OJ 535	2010-03-28	00038389002	18.23 ± 0.12	18.52 ± 0.07	17.35 ± 0.04	...	...	...
0824+5552	OJ 535	2010-03-28	00038389003	...	...	...	17.29 ± 0.04	...	...
0841+7053	4C 71.07	2010-03-21	00036376007	17.20 ± 0.04	...	...	...	...	...
0854+2006	PKS 0851+202	2010-04-10	00030901076	14.73 ± 0.02	15.06 ± 0.03	14.19 ± 0.02	14.20 ± 0.03	14.03 ± 0.04	14.20 ± 0.03
0915+2933	B2 0912+29	2010-10-28	00039151003	16.43 ± 0.08	16.57 ± 0.04	15.60 ± 0.04	15.48 ± 0.04	15.28 ± 0.05	15.39 ± 0.04
0915+2933	B2 0912+29	2010-10-28	00039151004	...	...	...	...	...	15.40 ± 0.03
0920+4441	S4 0917+44	2009-10-29	00020118001	17.71 ± 0.11	18.07 ± 0.07	17.33 ± 0.06	18.93 ± 0.21	<19.55	<19.84
0920+4441	S4 0917+44	2009-10-29	00038392002	17.84 ± 0.05	17.94 ± 0.09	17.46 ± 0.04	...	...	...
0923−2135	PKS 0921−213	2010-05-06	00037995052	...	...	...	...	16.60 ± 0.05	...
0923−2135	PKS 0921−213	2010-05-10	00037995053	...	...	...	...	16.66 ± 0.05	...
0957+5522	4C 55.17	2009-11-01	00038396002	17.59 ± 0.09	17.83 ± 0.05	16.85 ± 0.04	16.74 ± 0.04	16.55 ± 0.05	16.83 ± 0.04
1015+4926	1H 1013+498	2010-04-24	00035012018	15.46 ± 0.04	15.71 ± 0.04	14.76 ± 0.03	14.68 ± 0.04	14.53 ± 0.05	14.66 ± 0.04
1015+4926	1H 1013+498	2010-04-28	00035012019	...	...	...	...	14.55 ± 0.03	...
1058+5628	1RXSJ 105837.5+562816	2010-04-18	00038453002	15.42 ± 0.05	15.79 ± 0.04	14.90 ± 0.04	14.86 ± 0.04	14.83 ± 0.05	14.84 ± 0.04
1058+0133	4C 01.28	2009-12-03	00036379005	17.02 ± 0.06	17.41 ± 0.04	16.73 ± 0.04	16.77 ± 0.04	16.65 ± 0.05	16.88 ± 0.04
1058−8003	PKS 1057−79	2010-08-30	00036766004	18.04 ± 0.28	17.84 ± 0.13	17.01 ± 0.11	17.13 ± 0.13	17.16 ± 0.19	16.98 ± 0.11
1058−8003	PKS 1057−79	2010-08-30	00036766005	...	...	...	...	16.60 ± 0.09	...
1127−1857	PKS 1124−186	2010-06-10	00036243004	17.39 ± 0.07	17.77 ± 0.05	16.81 ± 0.04	...	...	...
1127−1857	PKS 1124−186	2010-06-10	00036243005	...	...	...	...	...	17.00 ± 0.04
1127−1857	PKS 1124−186	2010-06-14	00036243006	...	...	...	...	...	17.01 ± 0.04
1130−1449	PKS 1127−145	2009-12-28	00036380003	16.73 ± 0.07	17.11 ± 0.05	15.97 ± 0.04	15.79 ± 0.04	15.81 ± 0.05	16.05 ± 0.04
1130−1449	PKS 1127−145	2009-12-28	00036380004	...	...	...	...	...	16.14 ± 0.03
1131+3114	B2 1128+31	2009-11-28	00037564003	16.36 ± 0.03	16.22 ± 0.03	15.17 ± 0.02	15.10 ± 0.03	14.74 ± 0.03	14.86 ± 0.03
1147−3812	PKS 1144−379	2010-06-24	00040565001	18.69 ± 0.19	19.18 ± 0.14	18.59 ± 0.12	...	...	...
1147−3812	PKS 1144−379	2010-06-24	00040565002	...	...	...	18.77 ± 0.07	...	...
1153+4931	4C 49.22	2009-11-17	00037519002	17.34 ± 0.07	17.18 ± 0.04	16.01 ± 0.03	15.72 ± 0.04	15.28 ± 0.04	15.41 ± 0.03
1159+29114	4C 29.45	2010-05-28	00036381006	...	...	16.85 ± 0.02	...	...	...
1159+29114	4C 29.45	2010-05-28	00036381007	...	17.72 ± 0.08	16.84 ± 0.07	17.03 ± 0.08	...	16.93 ± 0.06
1217+3007	ON 325	2009-12-03	00031553001	15.59 ± 0.02	15.91 ± 0.02	15.06 ± 0.02	14.98 ± 0.03	14.84 ± 0.03	15.01 ± 0.03
1220+0203	PKS 1217+02	2010-06-24	00031744001	16.36 ± 0.07	16.19 ± 0.04	14.96 ± 0.04	14.91 ± 0.04	14.66 ± 0.04	14.50 ± 0.04
1220+0203	PKS 1217+02	2010-06-26	00031744002	...	...	...	...	...	14.62 ± 0.03
1221+2813	ON 231	2009-12-10	00035018025	15.03 ± 0.02	15.41 ± 0.02	14.59 ± 0.02	14.64 ± 0.03	14.53 ± 0.03	14.69 ± 0.03
1222+0413	PKS 1219+04	2010-06-17	00036330004	17.56 ± 0.07	17.92 ± 0.04	16.80 ± 0.04	...	...	...
1222+0413	PKS 1219+04	2010-06-17	00036330005	...	...	16.90 ± 0.02	...	...	...
1229+0203	3C 273	2010-01-10	00035017046	12.77 ± 0.01	...	...	...	...	...
1229+0203	3C 273	2010-01-11	00035017047	12.76 ± 0.01	...	...	...	...	...
1229+0203	3C 273	2010-01-12	00035017048	12.76 ± 0.01	...	...	...	...	...
1229+0203	3C 273	2010-01-13	00035017049	12.76 ± 0.01	...	...	...	...	...

Table 9. continued.

J2000.0 name	Source name	Obs. date	*Swift* ObsID	*V*	*B*	*U*	*UVW1*	*UVM2*	*UVW2*
1246−2547	PKS 1244−255	2010-01-25	00031591001	17.33 ± 0.15	17.69 ± 0.09	16.78 ± 0.07	16.50 ± 0.07	15.93 ± 0.08	16.10 ± 0.05
1246−2547	PKS 1244−255	2010-01-25	00031591002	...	...	...	...	...	16.17 ± 0.04
1248+5820	PG 1246+586	2010-05-20	00040749003	15.51 ± 0.04	15.85 ± 0.04	14.99 ± 0.03	14.92 ± 0.04	14.74 ± 0.04	14.94 ± 0.04
1248+5820	PG 1246+586	2010-05-20	00040749004	...	...	15.09 ± 0.02	...	...	...
1256−0547	3C 279	2010-01-15	00035019021	16.99 ± 0.05	17.59 ± 0.04	17.01 ± 0.04	17.22 ± 0.05	17.11 ± 0.05	17.24 ± 0.04
1310+3220	1Jy 1308+326	2009-12-12	00036384008	...	...	...	...	...	18.46 ± 0.06
1350+0940	GB6B 1347+0955	2010-07-18	00031760001	18.08 ± 0.23	19.31 ± 0.35	<18.95	<19.33	<19.44	<20.04
1350+0940	GB6B 1347+0955	2010-07-18	00031760002	17.20 ± 0.07	18.40 ± 0.10	18.54 ± 0.16	18.56 ± 0.12	18.62 ± 0.13	18.61 ± 0.09
1407−2701	1WGAJ 1407.5−2700	2010-02-12	00031618001	...	...	...	<20.06	...	...
1419+0628	3C 298.0	2010-07-30	00031777001	17.05 ± 0.05	17.44 ± 0.04	16.53 ± 0.04	...	...	...
1419+0628	3C 298.0	2010-07-30	00031777002	...	...	...	16.82 ± 0.04	...	...
1423+5055	BZQJ 1423+5055	2010-07-13	00035375002	...	17.66 ± 0.10	16.52 ± 0.07	16.36 ± 0.07	...	...
1423+5055	BZQJ 1423+5055	2010-07-13	00035375003	...	...	...	...	15.97 ± 0.03	...
1427+2348	PG 1424+240	2010-01-22	00039182002	14.41 ± 0.03	14.70 ± 0.03	13.85 ± 0.03	13.81 ± 0.04	13.63 ± 0.04	13.82 ± 0.04
1456+5048	1RXSJ 145603.4+504825	2009-12-25	00030925002	<18.49	19.00 ± 0.22	18.61 ± 0.21	18.04 ± 0.11	17.98 ± 0.12	18.01 ± 0.09
1456+5048	1RXSJ 145603.4+504825	2009-12-25	00030925003	...	...	...	...	18.01 ± 0.04	...
1504+1029	PKS 1502+106	2010-07-29	00036388018	18.47 ± 0.13	18.62 ± 0.09	17.97 ± 0.08	18.26 ± 0.09	18.31 ± 0.09	18.46 ± 0.07
1517−2422	AP Lib	2010-02-20	00036341005	14.72 ± 0.04	15.39 ± 0.04	14.93 ± 0.04	14.98 ± 0.05	14.88 ± 0.06	14.99 ± 0.05
1517−2422	AP Lib	2010-02-22	00036341006	...	...	...	...	...	14.93 ± 0.03
1555+1111	PG 1553+113	2010-02-05	00031368012	14.55 ± 0.02	14.82 ± 0.02	13.89 ± 0.02	13.77 ± 0.03	13.59 ± 0.03	13.72 ± 0.03
1603+1554	WE 1601+16W3	2010-08-14	00031786001	17.11 ± 0.10	18.03 ± 0.09	18.40 ± 0.18	18.32 ± 0.15	18.49 ± 0.18	18.54 ± 0.12
1603+1554	WE 1601+16W3	2010-08-14	00031786002	...	...	...	...	18.34 ± 0.07	...
1625−2527	OS −237.8	2010-08-27	00038428002	...	...	...	<12.48	...	...
1635+3808	4C 38.41	2010-03-07	00036389026	...	...	...	...	18.10 ± 0.08	...
1640+3946	NRAO 512	2010-08-06	00036213008	...	...	...	18.07 ± 0.04	...	...
1640+3946	NRAO 512	2010-08-07	00036213009	18.30 ± 0.11	18.50 ± 0.07	17.85 ± 0.06	...	...	...
1642+3948	3C 345	2010-03-06	00036390016	...	17.39 ± 0.06	16.78 ± 0.05	16.44 ± 0.05	...	16.34 ± 0.09
1642+3948	3C 345	2010-03-06	00036390017	...	...	...	...	16.24 ± 0.06	16.29 ± 0.05
1642+3948	3C 345	2010-03-07	00036390018	...	...	...	16.45 ± 0.04	...	...
1642+3948	3C 345	2010-03-08	00036390019	...	...	16.93 ± 0.03	...	...	...
1653+3945	Mkn 501	2010-03-21	00030793112	13.88 ± 0.01	14.50 ± 0.02	13.94 ± 0.02	13.89 ± 0.03	13.71 ± 0.03	13.80 ± 0.03
1719+4858	ARP 102B	2010-03-31	00035493002	...	...	...	17.08 ± 0.06	17.56 ± 0.09	17.54 ± 0.07
1719+4858	ARP 102B	2010-03-31	00035493003	...	...	...	...	17.59 ± 0.06	...
1751+0939	OT 081	2010-04-01	00036392011	17.17 ± 0.18	17.37 ± 0.11	16.74 ± 0.10	16.90 ± 0.13	16.51 ± 0.15	17.20 ± 0.14
1751+0939	OT 081	2010-04-04	00036392012	...	...	...	...	16.75 ± 0.10	...
1751+0939	OT 081	2010-04-06	00036392013	...	...	16.67 ± 0.03	...	...	...
1800+7828	S5 1803+784	2009-10-13	00036393005	15.79 ± 0.03	16.20 ± 0.03	15.41 ± 0.03	15.52 ± 0.04	15.43 ± 0.04	15.59 ± 0.03
1840−7709	PKS 1833−77	2010-03-11	00039424002	...	...	...	...	16.09 ± 0.05	...
1840−7709	PKS 1833−77	2010-03-13	00039424003	14.02 ± 0.03	14.93 ± 0.04	15.27 ± 0.05	16.12 ± 0.08	16.14 ± 0.10	16.04 ± 0.07
1840−7709	PKS 1833−77	2010-03-13	00039424004	...	...	15.37 ± 0.02	...	...	...
1840−7709	PKS 1833−77	2010-03-16	00039424005	...	...	...	16.05 ± 0.04	...	...

Table 9. continued.

J2000.0 name	Source name	Obs. date	*Swift* ObsID	*V*	*B*	*U*	*UVW1*	*UVM2*	*UVW2*
1911−2006	2E 1908.2−201	2009-10-04	00036351005	18.65 ± 0.32	18.56 ± 0.16	17.58 ± 0.10	17.32 ± 0.09	17.11 ± 0.09	17.40 ± 0.08
1923−2104	PMNJ 1923−2104	2010-09-30	00036771002	15.82 ± 0.05	16.18 ± 0.04	15.26 ± 0.04	15.22 ± 0.04	14.98 ± 0.05	15.30 ± 0.04
1923−2104	PMNJ 1923−2104	2010-09-30	00036771003	...	...	...	...	...	15.28 ± 0.03
1923−2104	PMNJ 1923−2104	2010-10-01	00036771004	...	...	...	...	14.94 ± 0.04	...
1924−2914	OV −236	2010-09-30	00031373002	17.01 ± 0.14	17.83 ± 0.16	17.06 ± 0.13	17.18 ± 0.13	16.51 ± 0.10	16.90 ± 0.09
1924−2914	OV −236	2010-09-30	00031373003	...	...	...	...	...	16.81 ± 0.04
1959+6508	1ES 1959+650	2009-09-26	00035025044	14.47 ± 0.01	14.78 ± 0.02	13.89 ± 0.02	13.84 ± 0.03	13.49 ± 0.03	13.53 ± 0.03
2009−4849	1Jy 2005−489	2009-10-05	00035026010	14.01 ± 0.02	14.40 ± 0.02	13.52 ± 0.02	13.40 ± 0.03	13.14 ± 0.03	13.27 ± 0.03
2056−4714	PKS 2052−47	2010-10-18	00038412009	...	...	...	17.76 ± 0.10	...	...
2056−4714	PKS 2052−47	2010-10-19	00038412010	18.32 ± 0.09	18.54 ± 0.05	17.50 ± 0.04	...	...	...
2056−4714	PKS 2052−47	2010-10-19	00038412011	...	...	17.45 ± 0.04	...	...	...
2129−1538	1Jy 2126−158	2010-05-03	00036356005	16.97 ± 0.14	17.92 ± 0.13	18.76 ± 0.34	<19.19	<18.99	<19.65
2129−1538	1Jy 2126−158	2010-05-03	00036356006	...	...	...	<20.87	...	...
2143+1743	S3 2141+17	2009-11-20	00036358005	15.85 ± 0.03	15.91 ± 0.03	14.72 ± 0.02	14.54 ± 0.03	14.22 ± 0.04	14.27 ± 0.03
2148+0657	4C 06.69	2009-11-21	00036774003	16.15 ± 0.03	16.42 ± 0.03	15.21 ± 0.03	14.99 ± 0.04	14.72 ± 0.04	15.03 ± 0.03
2151−3027	PKS 2149−307	2010-05-11	00031404008	17.58 ± 0.07	17.93 ± 0.06	17.24 ± 0.04	...	...	...
2151−3027	PKS 2149−307	2010-05-11	00031404009	...	...	...	18.17 ± 0.04	...	...
2202+4216	BLLac	2009-12-23	00035028039	14.40 ± 0.03	14.90 ± 0.04	14.29 ± 0.04	14.56 ± 0.06	14.18 ± 0.08	14.49 ± 0.06
2203+3145	4C 31.63	2009-11-27	00036226009	...	...	...	...	13.30 ± 0.03	...
2207−5346	PKS 2204−54	2010-05-03	00038409002	17.57 ± 0.16	17.85 ± 0.10	16.65 ± 0.06	16.42 ± 0.06	16.44 ± 0.08	16.80 ± 0.06
2207−5346	PKS 2204−54	2010-05-03	00038409003	...	...	...	16.46 ± 0.03	...	...
2230−3942	PKS 2227−399	2010-05-09	00037511002	17.56 ± 0.13	17.48 ± 0.06	16.48 ± 0.05	16.25 ± 0.05	15.69 ± 0.05	15.74 ± 0.04
2230−3942	PKS 2227−399	2010-05-09	00037511003	...	...	...	...	...	15.77 ± 0.03
2232+1143	4C 11.69	2009-11-29	00036401005	17.04 ± 0.07	17.25 ± 0.04	16.10 ± 0.04	15.87 ± 0.04	15.59 ± 0.04	15.91 ± 0.04
2253+1608	3C 454.3	2009-12-06	00035030079	...	...	...	13.97 ± 0.04	13.84 ± 0.04	14.09 ± 0.04
2303−1842	PKS 2300−18	2010-05-30	00031729001	17.15 ± 0.11	17.69 ± 0.08	16.61 ± 0.06	16.53 ± 0.06	16.39 ± 0.07	16.12 ± 0.04
2303−1842	PKS 2300−18	2010-05-30	00031729002	...	...	...	...	16.41 ± 0.04	...
2327+0940	PKS 2325+093	2010-06-18	00031558001	18.49 ± 0.14	18.77 ± 0.09	17.71 ± 0.05	...	...	...
2327+0940	PKS 2325+093	2010-06-18	00031558002	...	...	...	...	17.84 ± 0.09	18.12 ± 0.05
2333−2343	PKS 2331−240	2010-06-05	00031731001	16.20 ± 0.05	17.03 ± 0.05	16.77 ± 0.06	16.98 ± 0.07	16.87 ± 0.07	16.86 ± 0.05
2333−2343	PKS 2331−240	2010-06-05	00031731002	...	...	16.76 ± 0.02	...	...	...
2347+5142	1ES 2344+514	2010-01-17	00035031052	14.96 ± 0.04	15.82 ± 0.04	15.61 ± 0.06	15.78 ± 0.08	15.67 ± 0.10	15.64 ± 0.07

Notes. Columns 1 and 2: source name; Cols. 3 and 4: observation date and *Swift* observation ID; Cols. 5–10: magnitudes in the six UVOT filters.

Table 10. *Swift*-XRT data. described by a power-law. The last four lines refer to sources where the spectral index is fixed to $\Gamma = -2$.

J2000.0 name	Source name	Obs. date	Photon index	Galactic N_H	X-ray flux 10^{-12} erg cm^{-2} s^{-1}		Reduced χ^2	d.o.f.
				10^{21} cm^{-2}	0.1–2.4 keV	2–10 keV		
0010+1058	III ZW 2	2010-07-08	$-1.64^{+0.07}_{-0.07}$	0.54	6.8	12.8	1.24	58
0136+4751	S4 0133+47	2010-02-05	$-1.58^{+0.17}_{-0.17}$	1.04	0.9	1.9	0.96	10
0204−1701	PKS 0202−17	2010-01-08	$-1.63^{+0.25}_{-0.24}$	0.26	0.8	1.5	1.00	7
0210−5101	PKS 0208−512	2009-11-26	$-0.67^{+0.66}_{-0.57}$	0.18	0.8	8.5	0.55	1
0237+2848	4C 28.07	2010-02-05	$-1.18^{+0.42}_{-0.39}$	0.76	0.4	1.6	0.65	2
0334−4008	PKS 0332−403	2010-01-17	$-1.44^{+0.31}_{-0.30}$	0.15	0.5	1.5	0.62	3
0428−3756	PKS 0426−380	2010-08-17	$-1.85^{+0.36}_{-0.35}$	0.21	0.5	0.7	1.85	2
0457−2324	PKS 0454−234	2010-02-25	$-1.72^{+0.30}_{-0.30}$	0.28	0.5	0.8	1.71	4
0522−3627	PKS 0521−36	2010-03-05	$-1.63^{+0.07}_{-0.07}$	0.36	5.7	11.0	1.31	56
0530+1331	PKS 0528+134	2009-09-24	$-1.21^{+0.28}_{-0.27}$	2.40	0.5	2.0	0.87	6
0538−4405	PKS 0537−441	2010-03-03	$-1.83^{+0.10}_{-0.10}$	0.31	2.4	3.1	0.69	27
0539−2839	1Jy 0537−286	2010-03-12	$-1.08^{+0.35}_{-0.32}$	0.22	0.4	2.2	1.27	3
0623−6436	IRAS-L 06229−643	2010-08-19	$-2.11^{+0.12}_{-0.12}$	0.39	4.8	3.3	0.67	24
0738+1742	PKS 0735+17	2010-10-07	$-1.56^{+0.27}_{-0.28}$	0.40	0.3	0.7	1.58	3
0746+2549	B2.2 0743+25	2010-10-15	$-1.18^{+0.17}_{-0.17}$	0.45	0.5	2.0	0.94	9
0818+4222	S4 0814+425	2010-10-15	$-1.76^{+0.37}_{-0.37}$	0.56	0.2	0.3	0.28	1
0824+5552	OJ 535	2010-03-28	$-1.51^{+0.26}_{-0.26}$	0.47	0.5	1.2	0.33	4
0841+7053	4C 71.07	2010-03-21	$-1.31^{+0.22}_{-0.21}$	0.28	3.7	12.7	0.86	6
0854+2006	PKS 0851+202	2010-04-10	$-2.10^{+0.13}_{-0.14}$	0.25	4.0	2.8	0.87	15
0920+4441	S4 0917+44	2009-10-29	$-1.44^{+0.22}_{-0.22}$	0.15	1.1	3.0	0.30	6
0923−2135	PKS 0921−213	2010-05-06	$-1.81^{+0.12}_{-0.12}$	0.46	3.8	5.0	1.21	18
0957+5522	4C 55.17	2009-11-01	$-1.59^{+0.39}_{-0.38}$	0.09	0.3	0.7	0.27	2
1015+4926	1H 1013+498	2010-04-24	$-2.52^{+0.08}_{-0.08}$	0.08	4.1	3.6	10.85	46
1058+5628	1RXSJ 105837.5+562816	2010-04-18	$-2.35^{+0.62}_{-0.61}$	0.07	3.5	1.4	0.04	1
1058+0133	4C 01.28	2009-12-03	$-1.85^{+0.17}_{-0.17}$	0.31	1.5	1.9	0.61	9
1127−1857	PKS 1124−186	2010-06-10	$-1.40^{+0.19}_{-0.19}$	0.35	0.4	1.2	1.49	5
1131+3114	B2 1128+31	2009-11-28	$-2.11^{+0.14}_{-0.14}$	0.18	2.4	1.6	1.28	20
1147−3812	PKS 1144−379	2010-06-24	$-1.64^{+0.19}_{-0.18}$	0.74	0.7	1.3	1.13	8
1153+4931	4C 49.22	2009-11-17	$-2.06^{+0.13}_{-0.14}$	0.21	2.2	1.7	0.61	17
1159+2914	4C 29.45	2010-05-28	$-1.72^{+0.21}_{-0.21}$	0.18	0.6	0.9	1.40	6
1217+3007	ON 325	2009-12-03	$-2.56^{+0.10}_{-0.10}$	0.17	6.6	1.6	0.95	31
1220+0203	PKS 1217+02	2010-06-24	$-1.99^{+0.09}_{-0.09}$	0.18	4.3	3.9	0.79	35
1221+2813	ON 231	2009-12-10	$-2.35^{+0.24}_{-0.24}$	0.20	1.2	0.5	0.86	6
1222+0413	PKS 1219+04	2010-06-17	$-1.16^{+0.13}_{-0.13}$	0.16	0.8	3.9	1.12	16
1229+0203	3C 273	2010-01-11	$-1.57^{+0.02}_{-0.02}$	0.17	1.9	176.7	81.10	280
1248+5820	PG 1246+586	2010-05-20	$-2.53^{+0.12}_{-0.13}$	0.07	3.2	0.8	1.14	20
1256−0547	3C 279	2010-01-15	$-1.60^{+0.08}_{-0.08}$	0.21	3.8	7.8	1.20	41
1310+3220	1Jy 1308+326	2009-12-12	$-1.81^{+0.35}_{-0.35}$	0.12	0.7	0.9	0.01	2
1419+0628	3C 298.0	2010-07-30	$-2.03^{+0.37}_{-0.37}$	0.21	0.6	0.5	0.77	2

Table 10. continued.

J2000.0 name	Source name	Obs. date	Photon index	Galactic N_H 10^{21} cm^{-2}	X-ray flux 10^{-12} erg cm^{-2} s^{-1} 0.1–2.4 keV	2–10 keV	Reduced χ^2	d.o.f.
1423+5055	BZQJ 1423+5055	2010-07-13	$-2.00^{+0.14}_{-0.14}$	0.13	2.5	2.2	0.51	14
1427+2348	PG 1424+240	2010-01-22	$-2.35^{+0.17}_{-0.18}$	0.31	5.1	2.0	1.72	14
1456+5048	1RXSJ 145603.4+504825	2009-12-25	$-2.13^{+0.09}_{-0.09}$	0.16	3.7	2.4	0.90	30
1504+1029	PKS 1502+106	2010-07-29	$-1.78^{+0.29}_{-0.29}$	0.23	0.3	0.4	0.80	2
1517−2422	AP Lib	2010-02-20	$-1.48^{+0.10}_{-0.10}$	0.83	2.2	5.6	0.81	28
1625−2527	OS −237.8	2010-08-27	$-0.72^{+0.42}_{-0.38}$	1.30	0.2	1.7	1.16	2
1640+3946	NRAO 512	2010-08-07	$-1.87^{+0.50}_{-0.48}$	0.11	0.4	0.5	0.50	1
1642+3948	3C 345	2010-03-06	$-1.77^{+0.12}_{-0.12}$	0.11	2.2	3.2	0.70	20
1800+7828	S5 1803+784	2009-10-13	$-1.58^{+0.15}_{-0.16}$	0.34	0.9	2.0	1.30	11
1911−2006	2E 1908.2−201	2009-10-04	$-1.39^{+0.28}_{-0.27}$	0.92	0.6	1.9	0.79	5
1923−2104	PMNJ 1923−2104	2010-09-30	$-1.50^{+0.16}_{-0.15}$	0.58	0.7	1.8	0.45	11
1924−2914	OV −236	2010-09-30	$-1.72^{+0.08}_{-0.08}$	0.72	3.3	5.4	0.87	40
2143+1743	S3 2141+17	2009-11-20	$-1.46^{+0.22}_{-0.22}$	0.76	0.7	1.8	1.25	8
2148+0657	4C 06.69	2009-11-21	$-1.63^{+0.10}_{-0.10}$	0.45	2.2	4.3	0.89	26
2151−3027	PKS 2149−307	2010-05-11	$-1.35^{+0.08}_{-0.08}$	0.16	2.7	8.8	1.02	43
2203+3145	4C 31.63	2009-11-27	$-1.61^{+0.08}_{-0.08}$	0.85	3.3	6.5	1.22	44
2207−5346	PKS 2204−54	2010-05-03	$-1.17^{+0.25}_{-0.24}$	0.18	0.5	2.1	1.04	7
2209−4710	NGC 7213	2010-10-23	$-1.79^{+0.09}_{-0.09}$	0.11	7.0	9.7	1.14	32
2229−0832	PKS 2227−08	2009-11-19	$-1.63^{+0.18}_{-0.19}$	0.42	1.1	2.1	0.63	9
2230−3942	PKS 2227−399	2010-05-09	$-1.81^{+0.08}_{-0.08}$	0.13	3.8	5.0	1.49	41
2232+1143	4C 11.69	2009-11-29	$-1.47^{+0.17}_{-0.17}$	0.54	0.9	2.4	0.90	9
2303−1842	PKS 2300−18	2010-05-30	$-1.71^{+0.08}_{-0.08}$	0.22	3.4	5.5	0.81	42
2327+0940	PKS 2325+093	2010-06-18	$-1.41^{+0.14}_{-0.14}$	0.40	0.8	2.3	1.12	11
2333−2343	PKS 2331−240	2010-06-05	$-1.69^{+0.07}_{-0.07}$	0.16	3.7	6.4	1.04	45
2347+5142	1ES 2344+514	2010-01-17	$-2.56^{+0.32}_{-0.31}$	1.50	8.7	2.1	1.62	4
0221+3556	1Jy 0218+357	2010-08-20	−2.00	0.56	0.4	0.3	5.09	1.
0238+1636	PKS 0235+164	2010-01-30	−2.00	0.74	1.2	1.1	4.63	1.
1058−8003	PKS 1057−79	2010-08-30	−2.00	0.63	1.0	0.9	0.08	1.
1635+3808	4C 38.41	2010-03-07	−2.00	0.11	1.3	1.1	0.25	1.

Notes. Columns 1 and 2: source name; Col. 3: *Swift* observation date; Col. 4: best-fit photon index Γ_x; Col. 5: Galactic N_H; Cols. 6 and 7: 0.1–2.4 and 2–10 keV X-ray fluxes; Col. 8: reduced χ^2; Col. 9: number of degrees of freedom.

where both the normalization factor N and the spectral index Γ were allowed to vary in the model fit. The model also includes all the sources within a 20° RoI included in *Fermi*-LAT one-year catalog (Abdo et al. 2010c) and modeled using power-law functions. If a source included in the model is a pulsar belonging to the *Fermi*-LAT pulsar catalog (Abdo et al. 2010d), we modeled the spectrum with a power-law with exponential cut-off using the spectral parameters in the pulsar catalog.

For the evaluation of the γ-ray SEDs, the whole energy range from 100 MeV to 300 GeV was divided into two equal logarithmically spaced bins per decade. In each energy bin, the standard *gtlike* binned analysis was applied assuming power-law spectra with photon index =−2.0 for all the point sources in the model. Assuming that in each energy bin the spectral shape can be approximated by a power-law, the flux of the source in all selected energy bins was evaluated, requiring in each energy bin a TS greater than ten. If the TS is lower than ten, an upper limit (UL) was evaluated in that energy bin. Only the statistical errors in the fit parameters are shown in the plots. Systematic errors due mainly to uncertainties in the LAT effective area derived from the on-orbit estimations, are <5% near 1 GeV, 10% below 0.1 GeV, and 20% above 10 GeV.

For each source, we considered the three different integration periods for the γ-ray data:

- *Simultaneous observations*: data accumulated during the period of *Planck* observation of the source. As the *Planck* instruments point in slightly different directions and the field of view depends on the frequency of observation, a typical observation covering all *Planck* channels takes about one week, the exact integration time depending on the position of the source.
- *Quasi-simultaneous observations*: data integrated over a period of two months centered on the *Planck* observing period of the source.
- *Twenty-seven month Fermi-LAT integration*: data integrated over a period of 27 months from August 4, 2008 to November 4, 2010, i.e., the entire *Fermi*-LAT data set available for this paper.

Tables 13 and 14 give a summary of the γ-ray detections (TS > 25) in all our samples. The fraction of sources detected by *Fermi*-LAT during the simultaneous integrations is not very large and varies from ∼40% in the *Fermi*-LAT sample to just ∼20% in the soft X-ray selected sample. We note that even considering all the *Fermi*-LAT data available at the time of writing (27 month integration), a sizable fraction of the blazars in the radio and both soft and hard X-ray selected samples were not detected.

Detailed results of the *Fermi*-LAT analysis are given in Tables 15–20, where the observed fluxes or upper limits are given in six or three energy bands depending on the source brightness.

Two sources (PKS 0548−322 and NGC 7213) appear as significant γ-ray detections in our 27-month data set, although they were not included in any of the *Fermi*-LAT catalogues published so far (Abdo et al. 2009b, 2010c, and [10]). These should therefore be considered as new γ-ray detections.

4. The importance of simultaneity

Blazars are, by definition, highly variable sources. It is therefore important to use simultaneous multi-frequency data to build

[10] http://heasarc.gsfc.nasa.gov/W3Browse/all/fermilpsc.html

Table 11. *Swift*-XRT data for sources described by a log parabola.

			log parabola		Galactic N_H	X-ray flux 10^{-12} erg cm^{-2} s^{-1}			
J2000.0 name	Source name	Obs. date	a	b	10^{21} cm^{-2}	0.1–2.4 keV	2–10 keV	Reduced χ^2	d.o.f.
0550−3216	PKS 0548−322	2010-03-12	$-1.55^{+0.06}_{-0.05}$	$-0.27^{+0.10}_{-0.10}$	0.26	25.0	41.1	0.94	188
1104+3812	Mkn 421	2009-11-17	$-1.97^{+0.01}_{-0.01}$	$-0.40^{+0.02}_{-0.02}$	0.19	878.5	530.8	1.04	639
1136+7009	S5 1133+704	2009-10-28	$-1.86^{+0.05}_{-0.05}$	$-0.66^{+0.13}_{-0.13}$	0.12	91.7	50.7	1.17	164
1555+1111	PG 1553+113	2010-02-05	$-2.50^{+0.06}_{-0.06}$	$-0.35^{+0.18}_{-0.19}$	0.36	15.1	4.7	0.85	90
1653+3945	Mkn 501	2010-03-21	$-1.93^{+0.03}_{-0.03}$	$-0.22^{+0.07}_{-0.07}$	0.15	92.5	65.4	1.03	257
1959+6508	1ES 1959+650	2009-09-26	$-2.05^{+0.04}_{-0.03}$	$-0.59^{+0.05}_{-0.07}$	1.00	104.0	71.7	1.00	369
2009−4849	1Jy 2005−489	2009-10-05	$-2.02^{+0.07}_{-0.06}$	$-0.28^{+0.16}_{-0.16}$	0.39	69.0	48.5	1.29	98

Notes. Columns 1 and 2: source name; Col. 3: *Swift* observation date; Cols. 4 and 5: log parabola parameters a and b; Col. 6: Galactic N_H; Cols. 7 and 8: 0.1–2.4 and 2–10 keV X-ray fluxes; Col. 9: reduced χ^2; Col. 10: number of degrees of freedom.

Table 12. *Swift*-XRT data for sources described by a power-law leaving the column density $N_{\rm H}$ as free parameter.

J2000.0 name	Source name	Obs. date	Photon index	Galactic $N_{\rm H}$	X-ray flux 10^{-12} erg cm^{-2} s^{-1}		Reduced χ^2	d.o.f.
				10^{21} cm^{-2}	0.1–2.4 keV	2–10 keV		
0017+8135	S5 0014+813	2010-09-21	$-2.15^{+0.31}_{-0.35}$	$4.28^{+1.33}_{-1.11}$	4.2	2.7	0.75	14
0217+7349	1Jy 0212+735	2010-09-10	$-1.59^{+0.31}_{-0.35}$	$5.53^{+2.73}_{-1.95}$	2.2	4.7	0.93	12
0336+3218	NRAO 140	2010-08-26	$-1.57^{+0.12}_{-0.12}$	$3.37^{+0.63}_{-0.55}$	7.7	17.0	0.97	63
0423−0120	PKS 0420−01	2009-08-27	$-2.10^{+0.40}_{-0.46}$	$2.39^{+1.41}_{-1.09}$	3.6	2.6	0.61	9
0433+0521	3C 120	2010-02-25	$-1.86^{+0.09}_{-0.10}$	$2.22^{+0.31}_{-0.29}$	24.8	33.8	0.89	108
0915+2933	B2 0912+29	2010-10-28	$-2.68^{+0.14}_{-0.15}$	$0.77^{+0.25}_{-0.23}$	9.3	3.8	0.89	66
1130−1449	PKS 1127−145	2009-12-28	$-1.61^{+0.18}_{-0.20}$	$1.50^{+0.58}_{-0.50}$	2.5	4.9	0.79	27
1246−2547	PKS 1244−255	2010-01-25	$-2.09^{+0.29}_{-0.33}$	$1.65^{+0.86}_{-0.72}$	1.9	1.4	0.40	10
1507+0415	BZQJ 1507+0415	2010-08-05	$-3.66^{+0.37}_{-0.44}$	$2.34^{+0.69}_{-0.58}$	2.7	0.6	1.22	28
1719+4858	ARP 102B	2010-03-31	$-1.76^{+0.39}_{-0.44}$	$2.37^{+1.46}_{-1.17}$	2.1	3.2	0.38	8
1751+0939	OT 081	2010-04-01	$-1.93^{+0.29}_{-0.33}$	$2.24^{+0.98}_{-0.81}$	2.5	2.6	0.52	14
1833−2103	PKSB 1830−210	2010-09-23	$-1.22^{+0.20}_{-0.22}$	$7.81^{+2.54}_{-1.95}$	3.1	13.3	0.75	29
1840−7709	PKS 1833−77	2010-03-11	$-2.46^{+0.19}_{-0.21}$	$1.72^{+0.44}_{-0.40}$	9.6	2.9	1.19	37
2056−4714	PKS 2052−47	2010-10-18	$-2.19^{+0.68}_{-0.81}$	$1.99^{+1.95}_{-1.51}$	1.7	1.0	1.33	3
2129−1538	1Jy 2126−158	2010-05-03	$-1.71^{+0.16}_{-0.16}$	$1.75^{+0.55}_{-0.48}$	3.8	6.4	1.01	38
2202+4216	BL Lac	2009-12-23	$-1.88^{+0.23}_{-0.25}$	$2.93^{+0.90}_{-0.76}$	9.6	11.2	0.47	21
2253+1608	3C 454.3	2009-12-06	$-1.71^{+0.08}_{-0.08}$	$1.25^{+0.24}_{-0.23}$	56.3	93.0	0.86	113

Notes. Columns 1 and 2: source name; Col. 3: *Swift* observation date; Col. 4: best-fit photon index Γ_x; Col. 5: estimated $N_{\rm H}$; Col. 6 and 7: 0.1–2.4 and 2–10 keV X-ray fluxes; Col. 8: reduced χ^2; Col. 9: number of degrees of freedom.

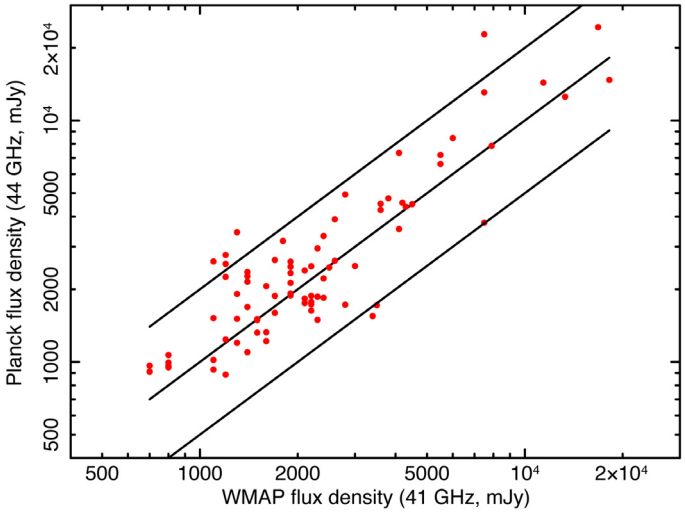

Fig. 1. The *Planck* 44 GHz flux density of the sources in our sample is plotted against the 41 GHz flux density from the WMAP five-year catalog (81 sources). The three solid lines represent equal flux densities (i.e., no variation) and a factor of two variability above or below the equal flux level. Almost all the points lie between the factor of two variability lines.

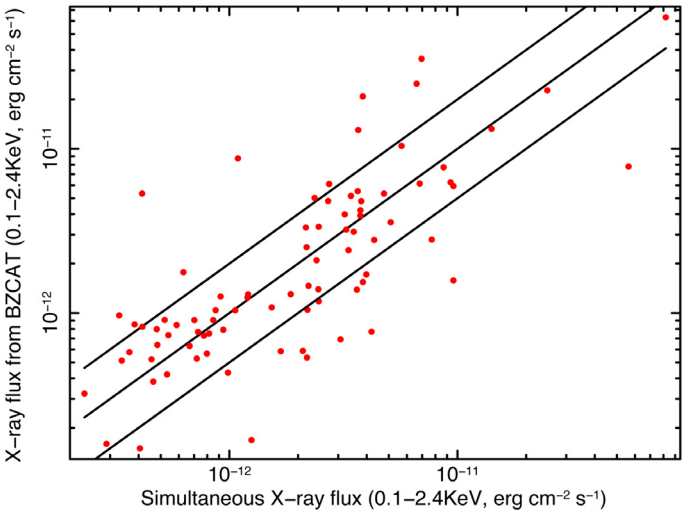

Fig. 2. The *Swift* X-ray (0.1–2.4 keV) flux of the sources in our sample measured simultaneously with *Planck* is plotted against the 0.1–2.4 keV flux reported in the BZCAT catalog (83 sources). The three solid lines represent equal fluxes (i.e., no variation) and a factor of two variability above or below the equal flux level. Note that several points are outside the factor of two variability lines, revealing variability of up to about a factor ten.

Table 13. Summary of γ-ray detections with significance TS > 25.

	No. of detected sources			Sources
Sample	simult.	2 months	27 months	in sample
Fermi-LAT	18 (36%)	40 (80%)	50 (100%)	50
Swift-BAT	9 (26%)	12 (35%)	27 (79%)	34
ROSAT/RASS	10 (23%)	15 (35%)	24 (56%)	43
Radio	22 (21%)	38 (37%)	78 (75%)	104

Table 14. Statistics of γ-ray detections (TS > 25) in the 27 month *Fermi*-LAT data set.

	No. of detected sources		
Sample	FSRQs	BL Lacs	Uncertain
Fermi-LAT	28 (100%)	14 (100%)	8 (100%)
Swift-BAT	17 (63%)	7 (100%)	3 (50%)
ROSAT/RASS	8 (53%)	14 (88%)	2 (17%)
Radio	48 (72%)	16 (100%)	9 (64%)

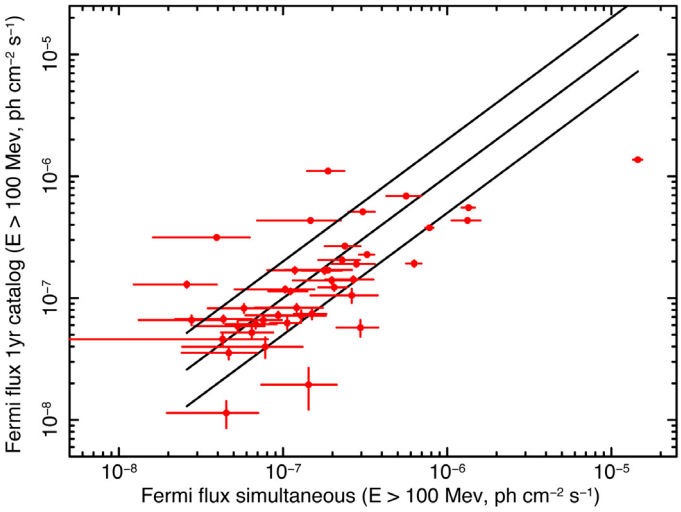

Fig. 3. The *Fermi*-LAT γ-ray flux of the sources in our samples detected during the simultaneous integration with *Planck* is plotted against the flux reported in the *Fermi*-LAT 1-year catalog. The three solid lines represent equal fluxes (i.e., no variation) and a factor of two variability above or below the equal flux level. Note that several points are outside the factor of two variability lines, revealing variability of up to about a factor ten.

SEDs for comparison with theoretical models. In this section, we compare our measurements with data taken from the literature in order to derive an estimate of the uncertainties introduced by the use of non-simultaneous data in different parts of the spectrum.

Figure 1 plots the *Planck* flux density at 44 GHz presented in this paper versus the WMAP flux density at 41 GHz from the WMAP point source catalogs (Bennett et al. 2003; Wright et al. 2009). Some scatter is present, but most of the points lie between the two solid lines indicating a factor of two variability.

Figure 2 plots the X-ray fluxes of the sources observed by *Swift* simultaneously with *Planck* (see Table 10) against the X-ray fluxes of the same sources from the BZCAT catalog (Massaro et al. 2009, 2010). In this case, a large scatter is present, with variations of over a factor of ten.

Figure 3 shows the *Fermi*-LAT γ-ray fluxes of our sources measured simultaneously with *Planck* plotted against their γ-ray fluxes in the *Fermi*-LAT 1FGL catalog (Abdo et al. 2010c). As in the X-ray sample, a scatter with variations larger than a factor of ten is observed.

We conclude that SEDs built with non-simultaneous data suffer from uncertainties in the microwave region that are relatively modest and generally limited to about a factor of two, while the high energy part of the spectrum (X-ray and γ-ray) is much more affected, with uncertainties caused by flux variations of up to a factor of ten or more. The same uncertainties, of course, apply when searching for correlations in non-simultaneous multi-frequency data.

Table 15. *Fermi*-LAT data at two bins/decade simultaneous with the *Planck* observations.

		Flux density (10^{-10} ph cm^{-2} s^{-1} MeV^{-1})						
J2000.0 name	Source name	100–316 MeV	316 MeV–1 GeV	1–3.16 GeV	3.16–10 GeV	10–31.6 GeV	31.6–100 GeV	100 GeV–316 GeV
0010+1058	III ZW 2	<6.1	<0.24	$<1.6 \times 10^{-2}$	...	...	...	...
0136+4751	S4 0133+47	<5.8	<0.43	$<3.0 \times 10^{-2}$	...	...	...	...
0319+4130	NGC 1275	8.5 ± 1.8	0.95 ± 0.12	$(13.1 \pm 1.8) \times 10^{-2}$	$(10.3 \pm 2.7) \times 10^{-3}$	$<1.0 \times 10^{-3}$	$(5.9 \pm 5.9) \times 10^{-5}$	...
0334−4008	PKS 0332−403	<3.9	<0.21	$<1.4 \times 10^{-2}$	$<2.7 \times 10^{-3}$	$(1.8 \pm 1.8) \times 10^{-4}$	...	$<2.7 \times 10^{-5}$
0428−3756	PKS 0426−380	<3.6	<0.19	$<2.4 \times 10^{-2}$	$(2.3 \pm 1.7) \times 10^{-3}$	$<4.6 \times 10^{-4}$	...	...
0457−2324	PKS 0454−234	8.3 ± 2.2	0.85 ± 0.17	$(4.7 \pm 1.8) \times 10^{-2}$	...	...	...	...
0522−3627	PKS 0521−36	<2.1	<0.23	$<3.0 \times 10^{-2}$	...	...	...	...
0530+1331	PKS 0528+134	<8.1	<0.74	...	...	...	...	...
0538−4405	PKS 0537−441	23.6 ± 1.9	2.23 ± 0.16	$(19.7 \pm 2.2) \times 10^{-2}$	$(16.8 \pm 3.5) \times 10^{-3}$	$(7.2 \pm 4.0) \times 10^{-4}$	...	...
0550−3216	PKS 0548−322	<2.6	<0.25	...	...	...	...	...
0920+4441	S4 0917+44	6.2 ± 2.1	0.48 ± 0.14	$<4.9 \times 10^{-2}$	$<5.3 \times 10^{-3}$	...	...	...
1015+4926	1H 1013+498	<4.6	<0.19	$(2.4 \pm 1.3) \times 10^{-2}$	$(3.3 \pm 2.3) \times 10^{-3}$	...	...	...
1104+3812	Mkn 421	6.8 ± 2.3	0.75 ± 0.17	$(6.2 \pm 2.1) \times 10^{-2}$	$(12.0 \pm 4.9) \times 10^{-3}$	$(3.2 \pm 1.3) \times 10^{-3}$	$<1.7 \times 10^{-3}$	$(6.0 \pm 6.0) \times 10^{-5}$
1127−1857	PKS 1124−186	<6.5	0.52 ± 0.13	$(3.7 \pm 1.4) \times 10^{-2}$	$(6.2 \pm 2.8) \times 10^{-3}$	...	...	...
1130−1449	PKS 1127−145	<4.6	<0.43	...	...	...	...	...
1147−3812	PKS 1144−379	<5.3	...	...	...	$<2.2 \times 10^{-3}$	...	...
1217+3007	ON 325	<1.8	0.21 ± 0.08	$(11.3 \pm 6.9) \times 10^{-3}$	...	...	...	...
1229+0203	3C 273	43.1 ± 5.2	2.92 ± 0.34	$(11.4 \pm 3.0) \times 10^{-2}$	$(6.7 \pm 3.9) \times 10^{-3}$	...	...	...
1248+5820	PG 1246+586	<2.1	<0.17	$(10.9 \pm 5.7) \times 10^{-3}$	...	...	...	...
1256−0547	3C 279	<16.3	1.20 ± 0.28	$(5.2 \pm 2.5) \times 10^{-2}$	...	...	...	...
1407−2701	1WGAJ 1407.5−2700	<3.5	...	...	...	...	...	...
1423+5055	BZQJ 1423+5055	<2.7	...	...	...	...	...	...
1427+2348	PG 1424+240	<7.2	<0.33	$(4.1 \pm 1.7) \times 10^{-2}$	$<8.1 \times 10^{-3}$	$<1.6 \times 10^{-3}$	...	...
1456+5048	1RXJ 145603.4+504825	<2.0	...	...	$<8.2 \times 10^{-4}$	...	...	...
1504+1029	PKS 1502+106	<9.9	0.55 ± 0.16	$(6.9 \pm 2.2) \times 10^{-2}$	$(7.7 \pm 3.9) \times 10^{-3}$	...	...	...
1603+1554	WE 1601+16W3	<2.4	...	$<2.0 \times 10^{-2}$	...	...	...	...
1635+3808	4C 38.41	22.2 ± 3.0	1.27 ± 0.18	$(4.4 \pm 1.6) \times 10^{-2}$	$<5.3 \times 10^{-3}$	...	...	...
1642+3948	3C 345	<4.2	<0.54	...	...	...	...	...
1653+3945	Mkn 501	<4.9	0.24 ± 0.10	$(2.2 \pm 1.1) \times 10^{-2}$	$(3.3 \pm 1.9) \times 10^{-3}$	$(4.5 \pm 4.2) \times 10^{-4}$	...	...
1751+0939	OT 081	...	<0.39	$<2.7 \times 10^{-2}$	$<2.3 \times 10^{-3}$	...	...	...
1800+7828	S5 1803+784	<4.6	0.31 ± 0.08	$(3.5 \pm 1.1) \times 10^{-2}$	$(1.5 \pm 1.1) \times 10^{-3}$	...	...	...
1833−2103	PKSB 1830−210	34.5 ± 9.1	18.6 ± 0.5	$(9.9 \pm 4.9) \times 10^{-2}$	$<1.6 \times 10^{-2}$	...	...	...
2143+1743	S3 2141+17	<8.0	0.44 ± 0.15	$<1.2 \times 10^{-2}$	...	...	...	...
2148+0657	4C 06.69	<7.8	<0.47	$<2.4 \times 10^{-2}$	...	...	...	...
2202+4216	BL Lac	9.0 ± 1.9	0.99 ± 0.15	$(4.4 \pm 1.4) \times 10^{-2}$	$<5.3 \times 10^{-3}$	...	...	$<4.1 \times 10^{-5}$
2232+1143	4C 11.69	<7.3	<0.35	$<3.4 \times 10^{-2}$	...	...	...	...
2253+1608	3C 454.3	204 ± 29	19.2 ± 2.4	1.23 ± 0.27	$(3.5 \pm 2.5) \times 10^{-2}$	...	...	...

Notes. Columns 1 and 2: source name; Cols. 3–9: *Fermi*-LAT flux densities in seven energy bands.

Table 16. *Fermi*-LAT data at one bin/decade simultaneous with the *Planck* observations.

J2000.0 name	Source name	Flux density (10^{-10} ph cm^{-2} s^{-1} MeV^{-1})		
		100 Mev–1 GeV	1–10 GeV	10–100 GeV
0017+8135	S5 0014+813	<0.33	$<3.0 \times 10^{-3}$	...
0035+5950	1ES 0033+595	...	<0.32	$<5.5 \times 10^{-2}$
0048+3157	Mkn 348	<0.49	...	...
0120−2701	1Jy 0118−272	<0.70	$(1.0 \pm 0.4) \times 10^{-2}$	...
0204−1701	PKS 0202−17	0.48 ± 0.21	...	...
0210−5101	PKS 0208−512	<0.64	$<1.3 \times 10^{-3}$	...
0214+5144	GB6J 0214+5145	<4.8	...	...
0217+7349	1Jy 0212+735	...	...	...
0217+0144	PKS 0215+015	0.91 ± 0.31	$<7.7 \times 10^{-3}$	...
0221+3556	1Jy 0218+357	<1.4	$<1.1 \times 10^{-2}$	...
0237+2848	4C 28.07	1.5 ± 0.5	$<1.1 \times 10^{-2}$	...
0238+1636	PKS 0235+164	<1.9	$<7.6 \times 10^{-3}$	...
0336+3218	NRAO 140	<0.95	$<1.5 \times 10^{-2}$	$<4.5 \times 10^{-4}$
0423−0120	PKS 0420−01	1.5 ± 0.5	$<1.1 \times 10^{-2}$	...
0433+0521	3C 120	<1.3	...	...
0539−2839	1Jy 0537−286	<0.59	...	...
0738+1742	PKS 0735+17	<1.1	$(5.2 \pm 3.1) \times 10^{-3}$	...
0746+2549	B2.2 0743+25	...	<0.46	...
0818+4222	S4 0814+425	<1.2	$<1.4 \times 10^{-2}$	...
0824+5552	OJ 535	<0.39	...	...
0841+7053	4C 71.07	<0.43	...	...
0854+2006	PKS 0851+202	<0.81	$<1.1 \times 10^{-2}$	...
0915+2933	B2 0912+29	<0.46	$<7.8 \times 10^{-3}$	...
0923−2135	PKS 0921−213	<0.21	...	...
0957+5522	4C 55.17	0.89 ± 0.27	$(1.7 \pm 0.5) \times 10^{-3}$	$(1.1 \pm 1.1) \times 10^{-4}$
1058+5628	1RXSJ 105837.5+562816	0.51 ± 0.19	$(6.2 \pm 2.3) \times 10^{-3}$	...
1058+0133	4C 01.28	<0.71	$<7.5 \times 10^{-3}$	...
1058−8003	PKS 1057−79	<0.65	$<7.4 \times 10^{-3}$	$<9.7 \times 10^{-5}$
1131+3114	B2 1128+31	<0.24	...	...
1136+7009	S5 1133+704	<0.77	$<8.0 \times 10^{-3}$	...
1153+4931	4C 49.22	<0.48	...	...
1159+2914	4C 29.45	17.8 ± 0.3	$(2.0 \pm 0.5) \times 10^{-2}$	...
1220+0203	PKS 1217+02	<0.50	...	...
1221+2813	ON 231	<0.65	$<5.7 \times 10^{-3}$	...
1222+0413	PKS 1219+04	1.2 ± 0.4	$<7.3 \times 10^{-3}$	...
1246−2547	PKS 1244−255	<1.8	$<1.7 \times 10^{-2}$	...
1305−1033	1Jy 1302−102	<0.55	...	...
1310+3220	1Jy 1308+326	<0.31	$(6.5 \pm 2.2) \times 10^{-3}$	...
1350+0940	GB6B 1347+0955	<0.43	...	...
1419+0628	3C 298.0	<0.66	$<7.2 \times 10^{-3}$	...
1507+0415	BZQJ 1507+0415	<0.45	...	...
1510−0543	4C −05.64	$(45.5 \pm 7.6) \times 10^{-2}$	$(21.3 \pm 2.9) \times 10^{-4}$	$<5.8 \times 10^{-6}$
1517−2422	AP Lib	1.22 ± 0.41	$<9.5 \times 10^{-3}$	$<4.8 \times 10^{-4}$
1555+1111	PG 1553+113	<1.1	$(14.6 \pm 3.3) \times 10^{-3}$	$<7.8 \times 10^{-5}$
1625−2527	OS −237.8	<2.9	$<1.4 \times 10^{-2}$	...
1640+3946	NRAO 512	<9.8	<0.67	$(5.7 \pm 1.7) \times 10^{-2}$
1719+4858	ARP 102B	...	...	...
1743+1935	1ES 1741+196	<0.31	...	$<2.5 \times 10^{-2}$
1840−7709	PKS 1833−77	<0.59	$<3.3 \times 10^{-3}$	...
1911−2006	2E 1908.2−201	<1.4	$<2.4 \times 10^{-2}$	...
1923−2104	PMNJ 1923−2104	1.97 ± 0.67	$(8.78 \pm 5.4) \times 10^{-3}$	...
1924−2914	OV −236	<1.6	$(12.7 \pm 6.9) \times 10^{-3}$	...
2129−1538	1Jy 2126−158	...	$<6.1 \times 10^{-3}$	$<4.2 \times 10^{-4}$
2147+0929	1Jy 2144+092	1.47 ± 0.45	$<7.6 \times 10^{-3}$	...
2151−3027	PKS 2149−307	<1.2	...	...
2203+3145	4C 31.63	<0.32	...	...
2207−5346	PKS 2204−54	<0.61	...	...
2209−4710	NGC 7213	<0.62	...	...
2229−0832	PKS 2227−08	<0.81	$<9.7 \times 10^{-3}$	...
2230−3942	PKS 2227−399	<0.31	...	$<9.1 \times 10^{-5}$
2303−1842	PKS 2300−18	<0.45	$<6.9 \times 10^{-3}$	...
2327+0940	PKS 2325+093	<0.97	$<4.7 \times 10^{-3}$	...
2333−2343	PKS 2331−240	<0.83	...	...
2347+5142	1ES 2344+514	...	$<9.9 \times 10^{-3}$	...

Notes. Columns 1 and 2: source name; Cols. 3–9: *Fermi*-LAT flux densities in three energy bands.

Table 17. *Fermi*-LAT data at two bins/decade integrated over two months around the *Planck* observations.

J2000.0 name	Source name	Flux density (10^{-10} ph cm^{-2} s^{-1} MeV^{-1})						
		100–316 MeV	316 MeV–1 GeV	1–3.16 GeV	3.16–10 GeV	10–31.6 GeV	31.6–100 GeV	100 GeV–316 GeV
0010+1058	III ZW 2	<2.2	<0.12	...	$<8.8\times10^{-4}$	...	...	...
0017+8135	S5 0014+813	<1.5	$<7.4\times10^{-2}$	$<4.5\times10^{-3}$	$<4.4\times10^{-4}$	...	...	...
S4 0133+47	2.90 ± 0.84	$(19.5\pm4.6)\times10^{-2}$	$(10.3\pm4.0)\times10^{-3}$	$<3.9\times10^{-4}$	$<2.8\times10^{-4}$	...	...	
0136+4751	PKS 0202−17	<0.9	$<9.8\times10^{-2}$	$<7.0\times10^{-3}$	...	...	...	...
0210−5101	PKS 0208−512	2.01 ± 0.69	$(9.9\pm3.4)\times10^{-2}$	$<5.5\times10^{-3}$	$<1.5\times10^{-3}$	...	...	...
0217+7349	1Jy 0212+735	...	<0.25	$<1.4\times10^{-2}$	$<1.1\times10^{-3}$	...	...	...
0217+0144	PKS 0215+015	3.85 ± 0.84	$(33.7\pm5.3)\times10^{-2}$	$(28.3\pm6.3)\times10^{-3}$	$(19.1\pm8.3)\times10^{-4}$	...	...	...
0221+3556	1Jy 0218+357	<3.7	$(14.8\pm4.2)\times10^{-2}$	$(16.6\pm5.1)\times10^{-3}$	$<2.0\times10^{-3}$	...	...	...
0237+2848	4C 28.07	5.48 ± 0.95	$(34.6\pm5.7)\times10^{-2}$	$(25.8\pm5.9)\times10^{-3}$	$<1.4\times10^{-3}$	...	...	...
0238+1636	PKS 0235+164	2.81 ± 0.92	<0.11	$<5.1\times10^{-3}$	$<1.6\times10^{-3}$	...	...	...
0319+4130	NGC 1275	11.2 ± 1.1	$(99.5\pm7.9)\times10^{-2}$	$(12.2\pm1.1)\times10^{-2}$	$(11.1\pm1.8)\times10^{-3}$	$(8.0\pm2.5)\times10^{-4}$	$(2.6\pm2.6)\times10^{-5}$	3.2×10^{-5}
0334−4008	PKS 0332−403	<3.1	$(12.6\pm3.7)\times10^{-2}$	$<1.3\times10^{-2}$	$(9.6\pm5.7)\times10^{-4}$	$<3.2\times10^{-4}$	...	...
0336+3218	NRAO 140	<6.1	<0.21	$<1.4\times10^{-2}$	$<4.5\times10^{-4}$	$<1.9\times10^{-4}$	...	...
0428−3756	PKS 0426−380	3.13 ± 0.76	$(27.0\pm4.8)\times10^{-2}$	$(24.5\pm5.8)\times10^{-3}$	$(24.5\pm8.9)\times10^{-4}$	$<3.3\times10^{-4}$	...	...
0433+0521	3C 120	<4.3	$<9.5\times10^{-2}$	...	...	...	...	...
0457−2324	PKS 0454−234	5.59 ± 0.87	$(60.4\pm6.5)\times10^{-2}$	$(36.1\pm6.7)\times10^{-3}$	$(14.0\pm6.8)\times10^{-4}$	$<1.2\times10^{-4}$	...	...
0522−3627	PKS 0521−36	<3.0	$(17.2\pm4.3)\times10^{-2}$	$(9.0\pm4.0)\times10^{-3}$	$<1.3\times10^{-3}$	...	...	...
0530+1331	PKS 0528+134	<5.0	<0.12	...	$(18.6\pm9.4)\times10^{-4}$	...	...	...
0539−2839	1Jy 0537−286	<2.4	<0.11	...	$<8.6\times10^{-4}$	...	...	...
0538−4405	PKS 0537−441	22.6 ± 1.3	2.15 ± 0.11	$(23.0\pm1.6)\times10^{-2}$	$(20.9\pm2.5)\times10^{-3}$	$(12.6\pm3.4)\times10^{-4}$	$(4.0\pm3.6)\times10^{-5}$	...
0550−3216	PKS 0548−322	<1.2	$<7.7\times10^{-2}$	$<2.4\times10^{-3}$	$<1.6\times10^{-3}$	...	...	...
0623−6436	IRAS-L 06229−643	<2.3	$<7.1\times10^{-2}$	$<6.3\times10^{-3}$	$<1.0\times10^{-3}$	...	...	...
0746+2549	B2.2 0743+25	<1.9	...	$<7.7\times10^{-3}$	$<4.7\times10^{-4}$	...	...	...
0818+4222	S4 0814+425	<2.9	$(16.1\pm3.8)\times10^{-2}$	$(11.6\pm4.0)\times10^{-3}$	$<1.8\times10^{-3}$	$<4.0\times10^{-4}$	...	...
0824+5552	OJ 535	<2.6	$<6.0\times10^{-2}$	$<4.4\times10^{-3}$	...	...	$<4.2\times10^{-5}$	...
0841+7053	4C 71.07	<2.8	$<5.7\times10^{-2}$	...	...	...	...	...
0920+4441	S4 0917+44	4.98 ± 0.76	$(33.5\pm4.8)\times10^{-2}$	$(13.6\pm4.1)\times10^{-3}$	$(11.5\pm6.1)\times10^{-4}$	...	...	...
0923−2135	PKS 0921−213	<3.1	...	...	...	...	...	...
0957+5522	4C 55.17	3.53 ± 0.64	$(26.8\pm4.0)\times10^{-2}$	$(46.7\pm6.7)\times10^{-3}$	$(22.1\pm7.7)\times10^{-4}$	$(2.9\pm1.4)\times10^{-4}$	...	$(7.8\pm7.8)\times10^{-6}$
1015+4926	1H 1013+498	1.82 ± 0.64	$(8.1\pm3.0)\times10^{-2}$	$(16.9\pm4.5)\times10^{-3}$	$(19.6\pm8.1)\times10^{-4}$	$(1.6\pm1.2)\times10^{-4}$	...	...
1058+5628	1RXSJ 105837.5+562816	<2.2	$(14.8\pm3.5)\times10^{-2}$	$(13.5\pm3.9)\times10^{-3}$	$(10.5\pm5.5)\times10^{-4}$	$<2.8\times10^{-4}$	...	...
1058+0133	4C 01.28	<4.2	$(18.1\pm5.0)\times10^{-2}$	$(10.1\pm4.7)\times10^{-3}$	$<1.9\times10^{-3}$	...	...	...
1058−8003	PKS 1057−79	<3.4	<0.20	$<1.2\times10^{-2}$	$(11.4\pm6.8)\times10^{-4}$	...	...	...
1104+3812	Mkn 421	6.51 ± 0.85	$(76.0\pm6.7)\times10^{-2}$	$(72.9\pm8.8)\times10^{-3}$	$(10.5\pm1.8)\times10^{-3}$	$(18.1\pm3.9)\times10^{-4}$	$(18.1\pm6.8)\times10^{-5}$	$(2.8\pm1.6)\times10^{-5}$
1127−1857	PKS 1124−186	5.15 ± 0.97	$(37.3\pm5.5)\times10^{-2}$	$(19.1\pm5.2)\times10^{-3}$	$(17.1\pm7.6)\times10^{-4}$	$<2.7\times10^{-4}$	...	...
1130−1449	PKS 1127−145	<2.9	<0.16	$<3.2\times10^{-3}$	...	...	...	...
1131+3114	B2 1128+31	...	$<6.2\times10^{-2}$	...	$<1.1\times10^{-3}$	...	...	...
1136+7009	S5 1133+704	...	<0.12	$<8.5\times10^{-3}$	$<1.2\times10^{-3}$	$(13.2\pm9.3)\times10^{-5}$	$<2.0\times10^{-4}$	...
1147−3812	PKS 1144−379	<1.1	$<7.5\times10^{-2}$	$<3.9\times10^{-3}$	$<1.1\times10^{-3}$	$<3.7\times10^{-4}$	...	...
1153+4931	4C 49.22	<1.5	$<4.2\times10^{-2}$	$<5.8\times10^{-3}$	...	...	...	...
1159+2914	4C 29.45	9.64 ± 0.97	$(65.2\pm6.3)\times10^{-2}$	$(64.7\pm8.4)\times10^{-3}$	$(3.4\pm1.0)\times10^{-3}$	$(2.0\pm1.4)\times10^{-4}$	$(25.5\pm2.6)\times10^{-6}$	...
1217+3007	ON 325	<2.3	$(27.4\pm5.2)\times10^{-2}$	$(12.4\pm4.5)\times10^{-3}$	$<2.1\times10^{-3}$	$(1.8\pm1.3)\times10^{-4}$	...	...
1220+0203	PKS 1217+02	<3.0	$<7.1\times10^{-2}$	$<8.7\times10^{-3}$	$<4.5\times10^{-4}$	...	...	...
1221+2813	ON 231	<3.6	<0.17	$(13.7\pm4.5)\times10^{-3}$	$<1.0\times10^{-3}$	$<2.6\times10^{-4}$	...	...
1222+0413	PKS 1219+04	3.9 ± 1.1	$(15.9\pm4.7)\times10^{-2}$	$<8.5\times10^{-3}$	$<5.9\times10^{-4}$	...	...	...
1229+0203	3C 273	26.4 ± 1.9	1.32 ± 0.10	$(60.0\pm9.3)\times10^{-3}$	$<2.5\times10^{-3}$	$<3.7\times10^{-4}$	...	...
1246−2547	PKS 1244−255	<4.1	$(17.8\pm4.9)\times10^{-2}$	$<1.5\times10^{-2}$	$<4.3\times10^{-4}$	...	...	...
1248+5820	PG 1246+586	<0.68	$(7.0\pm2.7)\times10^{-2}$	$(12.1\pm3.7)\times10^{-3}$	$<1.4\times10^{-3}$	$(1.5\pm1.1)\times10^{-4}$	...	...
1256−0547	3C 279	13.1 ± 1.5	$(83.2\pm8.2)\times10^{-2}$	$(37.0\pm7.5)\times10^{-3}$	$<2.2\times10^{-3}$	...	...	...

Table 17. continued.

J2000.0 name	Source name	Flux density (10^{-10} ph cm^{-2} s^{-1} MeV^{-1})						
		100–316 MeV	316 MeV–1 GeV	1–3.16 GeV	3.16–10 GeV	10–31.6 GeV	31.6–100 GeV	100 GeV–316 GeV
1310+3220	1Jy 1308+326	2.78 ± 0.83	<0.10	$(12.6 \pm 4.2) \times 10^{-3}$	$(11.5 \pm 5.9) \times 10^{-4}$	...	...	...
1350+0940	GB6B 1347+0955	<0.90	$<5.4 \times 10^{-2}$	$<4.2 \times 10^{-3}$	...	...	...	...
1407−2701	1WGAJ 1407.5−2700	<1.6	<0.10	$<5.6 \times 10^{-3}$	...	...	...	...
1419+0628	3C 298.0	<2.9	$<7.4 \times 10^{-2}$	...	$<1.3 \times 10^{-3}$	...	...	...
1423+5055	BZQJ 1423+5055	<1.5	...	...	...	...	...	...
1427+2348	PG 1424+240	<3.6	$(16.4 \pm 4.4) \times 10^{-2}$	$(31.4 \pm 6.8) \times 10^{-3}$	$(2.9 \pm 1.0) \times 10^{-3}$	$(5.8 \pm 2.4) \times 10^{-4}$	$(10.5 \pm 5.7) \times 10^{-5}$	...
1456+5048	1RXSJ 145603.4+504825	...	$<2.2 \times 10^{-2}$	$<3.3 \times 10^{-3}$	$<3.6 \times 10^{-4}$	...	...	...
1504+1029	PKS 1502+106	6.7 ± 1.0	$(35.6 \pm 5.7) \times 10^{-2}$	$(25.3 \pm 6.0) \times 10^{-3}$	$(18.5 \pm 8.2) \times 10^{-4}$	...	...	...
1507+0415	BZQJ1507+0415	<3.4	...	$<8.1 \times 10^{-3}$	$<4.4 \times 10^{-4}$	...	...	...
1510−0543	4C −05.64	<2.7	<0.36	$(11.9 \pm 4.9) \times 10^{-3}$	...	...	...	...
1517−2422	AP Lib	<3.6	$(27.4 \pm 6.1) \times 10^{-2}$	$(25.0 \pm 6.9) \times 10^{-3}$	$(3.4 \pm 1.2) \times 10^{-3}$	$<3.3) \times 10^{-4}$	...	...
1555+1111	PG 1553+113	<2.1	$(16.8 \pm 5.7) \times 10^{-2}$	$(48.2 \pm 8.4) \times 10^{-3}$	$(5.6 \pm 1.4) \times 10^{-3}$	$<3.6 \times 10^{-4}$	$(6.3 \pm 4.4) \times 10^{-5}$	...
1603+1554	WE 1601+16W3	<2.2	$<7.8 \times 10^{-2}$	$<5.0 \times 10^{-3}$	...	...	...	...
1625−2527	OS −237.8	9.2 ± 3.0	0.42 ± 0.11	$(24.5 \pm 8.1) \times 10^{-3}$	$(13.9 \pm 7.4) \times 10^{-4}$	$<3.1 \times 10^{-4}$	...	...
1635+3808	4C 38.41	17.4 ± 1.3	1.24 ± 0.08	$(48.6 \pm 7.5) \times 10^{-3}$	$(24.4 \pm 8.9) \times 10^{-4}$	$<3.0 \times 10^{-4}$	...	...
1640+3946	NRAO 512	8.8 ± 1.3	$(64.5 \pm 6.7) \times 10^{-2}$	$(48.8 \pm 7.4) \times 10^{-3}$	$(26.2 \pm 9.2) \times 10^{-4}$	...	...	...
1642+3948	3C 345	<5.5	$(39.5 \pm 6.1) \times 10^{-2}$	$(18.5 \pm 5.1) \times 10^{-3}$	$(23.2 \pm 9.0) \times 10^{-4}$	...	...	...
1653+3945	Mkn 501	<2.9	$(16.9 \pm 4.3) \times 10^{-2}$	$(17.9 \pm 5.0) \times 10^{-3}$	$(19.1 \pm 7.9) \times 10^{-4}$	$(4.5 \pm 2.0) \times 10^{-4}$	...	...
1719+4858	ARP 102B	<2.2	...	...	...	...	...	...
1751+0939	OT 081	...	<0.14	$<1.8 \times 10^{-2}$	$<5.0 \times 10^{-4}$	...	...	...
1800+7828	S5 1803+784	2.44 ± 0.58	$(17.9 \pm 3.6) \times 10^{-2}$	$(16.4 \pm 4.0) \times 10^{-3}$	$(12.4 \pm 5.6) \times 10^{-4}$	$<2.2 \times 10^{-4}$	...	...
1833−2103	PKSB 1830−210	40.5 ± 2.1	...	...	...	...	...	...
1840−7709	PKS 1833−77	...	...	$<5.6 \times 10^{-3}$	$<1.1 \times 10^{-3}$	...	...	...
1911−2006	2E 1908.2−201	<5.9	<0.26	$(16.0 \pm 5.3) \times 10^{-3}$	$(7.8 \pm 5.3) \times 10^{-4}$	...	...	...
1923−2104	PMNJ 1923−2104	<3.4	$(28.1 \pm 5.6) \times 10^{-2}$	$(10.5 \pm 4.2) \times 10^{-3}$	$<1.3 \times 10^{-3}$	...	...	...
1924−2914	OV −236	<3.3	<0.15	$(10.7 \pm 4.6) \times 10^{-3}$	$<1.6 \times 10^{-3}$	$<3.1 \times 10^{-4}$	$<3.6 \times 10^{-5}$	...
2009−4849	1Jy 2005−489	<1.9	<0.17	$(7.5 \pm 3.4) \times 10^{-3}$	$(8.8 \pm 5.3) \times 10^{-4}$	$(1.6 \pm 1.2) \times 10^{-4}$	$(2.5 \pm 2.5) \times 10^{-5}$	...
2056−4714	PKS 2052−47	4.75 ± 0.86	$(16.2 \pm 4.3) \times 10^{-2}$	$<1.2 \times 10^{-2}$	$<4.2 \times 10^{-4}$	...	...	...
2129−1538	1Jy 2126−158	...	$<7.5 \times 10^{-2}$	$<8.3 \times 10^{-3}$	...	...	...	...
2143+1743	S3 2141+17	6.3 ± 1.3	$(36.3 \pm 6.1) \times 10^{-2}$	$(18.3 \pm 5.2) \times 10^{-3}$	$<4.5 \times 10^{-4}$	...	...	...
2147+0929	1Jy 2144+092	6.7 ± 1.2	$(21.9 \pm 5.5) \times 10^{-2}$	$(13.1 \pm 4.7) \times 10^{-3}$	$(9.1 \pm 5.6) \times 10^{-4}$	$<3.3 \times 10^{-4}$	...	...
2148+0657	4C 06.69	<2.6	<0.13	$<8.4 \times 10^{-3}$	...	...	...	...
2151−3027	PKS 2149−307	<2.8	<0.16	$<3.5 \times 10^{-3}$	...	...	...	...
2202+4216	BL Lac	7.7 ± 1.1	$(53.6 \pm 7.0) \times 10^{-2}$	$(41.1 \pm 7.3) \times 10^{-3}$	$(32.9 \pm 9.9) \times 10^{-4}$	$(1.6 \pm 1.1) \times 10^{-4}$	...	...
2203+3145	4C 31.63	<2.5	$<8.0 \times 10^{-2}$	...	...	...	...	...
2207−5346	PKS 2204−54	<1.9	$<8.6 \times 10^{-2}$	...	$<4.4 \times 10^{-4}$	...	...	...
2209−4710	NGC 7213	<1.0	...	...	...	$<1.8 \times 10^{-4}$	...	...
2229−0832	PKS 2227−08	4.17 ± 0.92	$(14.0 \pm 0.4) \times 10^{-2}$	$(14.5 \pm 4.9) \times 10^{-3}$	...	$<1.3 \times 10^{-4}$	...	...
2230−3942	PKS 2227−399	<1.3	$<6.2 \times 10^{-2}$	...	$<4.3 \times 10^{-4}$	...	...	...
2232+1143	4C 11.69	<3.8	$(16.3 \pm 4.7) \times 10^{-2}$	$<1.6 \times 10^{-2}$	$<1.1 \times 10^{-3}$	...	...	...
2253+1608	3C 454.3	220 ± 3	17.2 ± 0.3	1.13 ± 0.03	$(44.3 \pm 3.8) \times 10^{-3}$	$(11.8 \pm 3.3) \times 10^{-4}$	...	...
2303−1842	PKS 2300−18	<1.4	...	$<4.5 \times 10^{-3}$	$<4.4 \times 10^{-4}$	...	...	...
2327+0940	PKS 2325+093	<2.5	<0.11	$<3.6 \times 10^{-3}$	$<5.6 \times 10^{-4}$	...	...	...
2333−2343	PKS 2331−240	<2.4	$<8.2 \times 10^{-2}$	$<5.4 \times 10^{-3}$	...	...	...	...

Notes. Columns 1 and 2: source name; Cols. 3–9: *Fermi*-LAT flux densities in seven energy bands.

5. Spectral energy distributions

We constructed the SEDs of all the blazars in our samples from the simultaneous multi-frequency data described above using the ASDC SED Builder, an on-line service developed at the ASI Science Data Center (ASDC)[11] (Stratta et al. 2011). This is a WEB-based tool that allows users to build multi-frequency SEDs combining data from local catalogs and external services (e.g., NED, SDSS, USNO) with the user's own data. The tool converts observed fluxes or magnitudes into de-reddened fluxes at a given frequency using standard recipes that take into account the instrument response and assumed average spectral slopes. The SED builder can display SEDs both in flux and in luminosity (if redshift information is given); it also provides useful tasks such as the overlay of templates for blazar host galaxies and nuclear optical emission (blue-bump), and allows users to compare the SED with models including one or more SSC components.

The SEDs of all the sources in our samples are shown in Figs. 24–41. In these figures, red points represent strictly simultaneous multi-frequency data, green points represent γ-ray data integrated over a period of two months centered on the times of the *Swift*/*Planck* observations, ground-based data taken quasi-simultaneously, and *Planck*-ERCSC flux densities, and blue points represent γ-ray data integrated over the full period of 27 months. In the few cases where no *Swift* simultaneous observations could be obtained, we plot only *Planck*, *Fermi*-LAT, and ground-based data. Two-σ upper limits are indicated by arrows.

5.1. Distinguishing the non-thermal/jet-related radiation from QSO accretion and host galaxy emission

We used the simultaneous SEDs of Figs. 24–41 to determine some parameters that can constrain the physical mechanisms powering blazars. However, before doing so we had to identify and separate the radiation that is unrelated to the non-thermal, relativistically amplified emission from the jet of the blazars; that is, radiation from accretion onto the central black hole and from the host galaxy (see, e.g., Perlman et al. 2008). To do so, we estimated the contamination by the host galaxy assuming that all blazars are hosted by giant elliptical galaxies (e.g., Kotilainen et al. 1998; Nilsson et al. 2003; León-Tavares et al. 2011a) with absolute magnitude of $M_R = -23.7$. As Scarpa et al. (2000) and Urry et al. (2000) demonstrated, this value is within one magnitude of the observed values in a sample of over 100 BL Lacs observed with the *Hubble* Space Telescope. For the spectral shape, we used the elliptical galaxy template of Mannucci et al. 2001 (bottom panel of Fig. 4), which is based on low spectral resolution observations of a number of nearby galaxies in the wavelength range 0.12–2.4 μm and is a good match to the predictions of spectrophotometric models for giant ellipticals Mannucci et al. (2001).

The radiation produced by accretion was estimated from the composite optical spectrum built by Vanden Berk et al. (2001) using over 2200 optical spectra of radio-quiet QSOs taken from the SDSS database (York et al. 2000) (top panel of Fig. 4), and the expected soft X-ray emission of radio quiet AGN from Grupe et al. (2010).

The ratio of optical to soft X-ray light has been known to be a function of optical luminosity since the early obervations of the *Einstein* observatory (Avni & Tananbaum 1986). More recently, this dependence has been confirmed using simultaneously acquired optical and soft X-ray data from *Swift* (Grupe et al. 2010) and *XMM-Newton* (Vagnetti et al. 2010). To assess the presence

[11] http://tools.asdc.asi.it/SED/

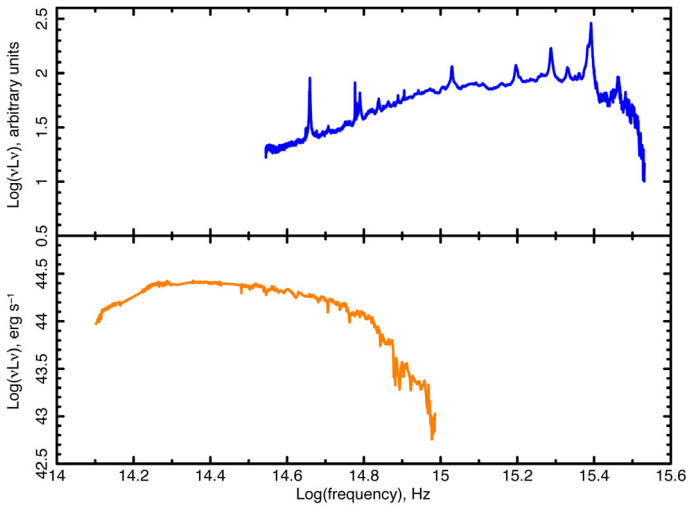

Fig. 4. *Top panel*: the SDSS template of Vanden Berk et al. (2001) for the broad-line and thermal emission from a QSO. *Bottom panel*: the giant elliptical galaxy template of Mannucci et al. (2001). See text for details.

of a possible thermal component in the X-ray emission, we used the relationship given by Grupe et al. (2010)

$$\alpha_{\mathrm{UV-X(Radio-quietQSO)}} = 0.114 \log(L_{2500\,\text{Å}}) - 1.177, \quad (2)$$

where $L_{2500\,\text{Å}}$ is the rest-frame luminosity of the thermal emission at 2500 Å in units of W Hz^{-1} and $\alpha_{\mathrm{UV-X(radio-quietQSO)}}$ is the usual slope between the UV (2500 Å) and the soft X-ray (2 keV) flux in radio quiet QSOs (e.g., Vagnetti et al. 2010).

Examples of the emission from these components unrelated to the jet are shown in Fig. 5, which shows the SEDs of Mkn 501 and Mkn 421 where the optical light is dominated by the host galaxy.

Figures 6 and 7 show the SEDs of BL Lacertae where part of the UV light is thought to originate in disk emission (Raiteri et al. 2009), the nearby FSRQ 3C 273 ($z = 0.158$), the high-redshift FSRQs 4C 38.41 ($z = 1.814$) and 1 Jy 0537−286 ($z = 3.104$) where the optical/UV light is heavily, or completely, contaminated by radiation coming from accretion onto the central black hole. We compared the amplitude of the optical thermal emission to non-thermal radiation using the parameter $\alpha_{\mathrm{R-O(Thermal)}}$, defined as the spectral slope between the 5 GHz radio flux density and the 5000 Å optical flux density that can be attributed to the blue-bump/disk/thermal emission. This quantity depends on both the relativistic amplification factor and the intrinsic ratio of non-thermal/jet radiation to disk emission. In the case of FSRQs, the optical spectrum displays emission lines by definition, therefore we were able to constrain $\alpha_{\mathrm{R-O(Thermal)}}$ by adjusting the optical thermal emission to the same level as the data. When the thermal blue bump was seen directly in the optical/UV part of the SED (e.g., Figs. 6 and 7), we fit the template of Vanden Berk et al. (2001) to the observed data; when the disk emission was not obviously visible we set the intensity of the blue-bump template to just below the observed optical/UV emission where the broad emission lines had been detected.

The BL Lacs do not show emission lines in their optical spectrum, so for this class of objects we could only set upper limits on $\alpha_{\mathrm{R-O(Thermal)}}$. We did that by assuming that the template for the optical thermal emission is at least one order of magnitude below the observed data, that is sufficiently low to hamper any broad line detection. The estimation of $\alpha_{\mathrm{R-O(Thermal)}}$ relies strongly on

Table 18. *Fermi*-LAT data at one bin/decade integrated over 2 months around the *Planck* observations.

J2000.0 name	Source name	Flux density (10^{-10} ph cm^{-2} s^{-1} MeV^{-1})		
		100 Mev–1 GeV	1–10 GeV	10–100 GeV
0035+5950	1ES 0033+595	<0.41	$<3.8 \times 10^{-3}$	$<7.0 \times 10^{-5}$
0048+3157	Mkn 348	<0.19	$<4.6 \times 10^{-4}$	$<6.8 \times 10^{-5}$
0120−2701	1Jy 0118−272	$(43.3 \pm 9.8) \times 10^{-2}$	$(4.7 \pm 1.2) \times 10^{-3}$	$(6.0 \pm 3.5) \times 10^{-5}$
0214+5144	GB6J 0214+5145	<0.22	$<1.9 \times 10^{-3}$	...
0423−0120	PKS 0420−01	1.34 ± 0.18	$(6.5 \pm 1.5) \times 10^{-3}$	...
0738+1742	PKS 0735+17	0.51 ± 0.13	$(3.6 \pm 1.2) \times 10^{-3}$	$(7.3 \pm 4.2) \times 10^{-5}$
0854+2006	PKS 0851+202	0.50 ± 0.14	$(3.2 \pm 1.19 \times 10^{-3}$	$(4.1 \pm 2.9) \times 10^{-5}$
0915+2933	B2 0912+29	<0.18	$(96.5 \pm 5.4) \times 10^{-5}$	...
1305−1033	1Jy 1302−102	<0.29	...	...
1743+1935	1ES 1741+196	<0.39	$<2.9 \times 10^{-3}$	...
2347+5142	1ES 2344+514	<0.41	$<2.5 \times 10^{-3}$	...

Notes. Columns 1 and 2: source name; Cols. 3–9: *Fermi*-LAT flux densities in seven energy bands.

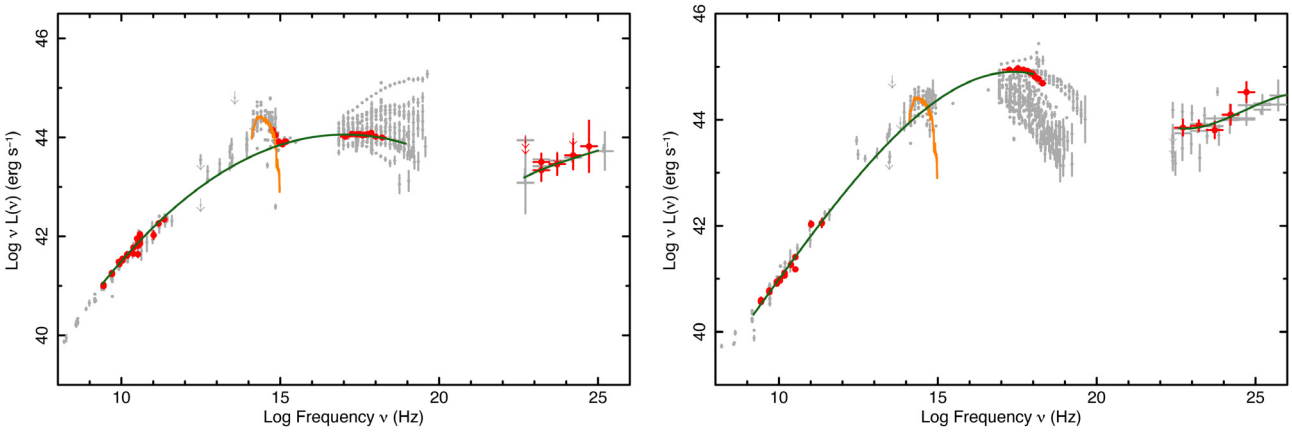

Fig. 5. The SEDs of Mkn 501 (*left*) and Mkn 421 (*right*) showing the expected emission from the host galaxy (giant elliptical) as an orange line. The green lines are the best-fit to the simultaneous non-thermal data using a third degree polynomial function. See text for details.

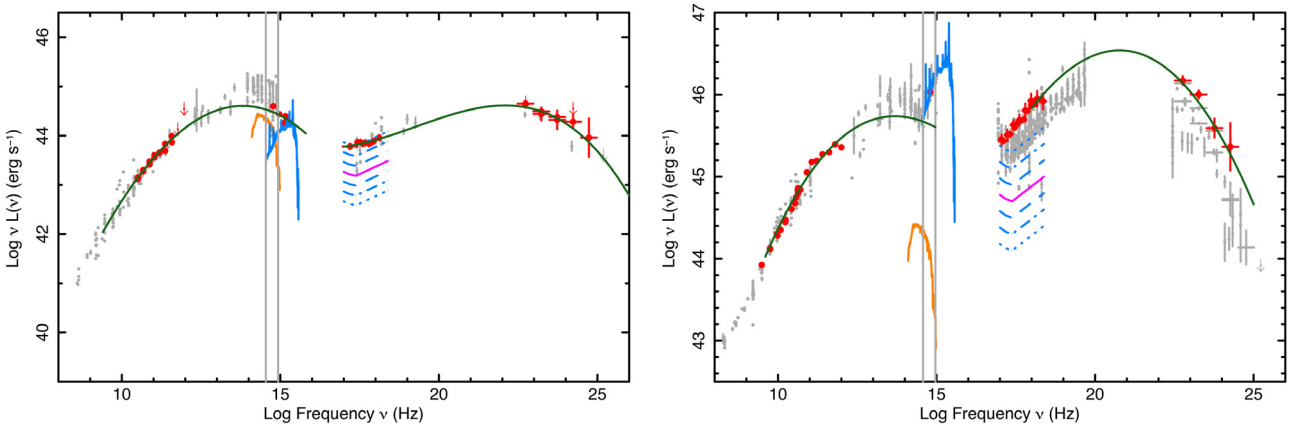

Fig. 6. *Left*: the SED of BL Lacertae showing the expected emission from the host galaxy (just below the observed non-thermal radiation, giant elliptical, orange line) and the blue bump emission (blue line, see also Raiteri et al. 2009). *Right*: the SED of 3C 273 showing the thermal emission from the blue bump and the expected X-ray emission from accretion including 1, 2, and 3σ bands (purple and blue lines) derived from Eq. (2). The vertical parallel lines represent the optical window (4000–10 000 Å). The green lines are the best-fit to the simultaneous non-thermal data using a third degree polynomial function.

the quality of the optical data available, in particular on the simultaneous UVOT data. Therefore we define an "optical data quality" flag as follows:

- 0: no simultaneous data available;
- 1: poor quality (e.g., only one UVOT filter available);
- 2: good quality (e.g., two or three UVOT filters available);
- 3: excellent quality (all UVOT filters available).

In Fig. 8 (upper panel), we show the distribution of $\alpha_{\rm R-O(Thermal)}$ for all the FSRQs with excellent optical data for the whole sample and each of our samples independently. The distribution of the $\alpha_{\rm R-O(Thermal)}$ upper limits for BL Lac objects is shown in the bottom panel. The results suggest a possible difference in the $\alpha_{\rm R-O(Thermal)}$ distribution between different samples. As reported in Table 21, when only sources with excellent optical data are considered we obtain $\langle\alpha_{\rm R-O(Thermal)}\rangle = -0.64 \pm 0.05$ for

Table 19. *Fermi*-LAT data at two bins/decade integrated over 27 months.

J2000.0 name	Source name	Flux density (10^{-10} ph cm^{-2} s^{-1} MeV^{-1})						
		100–316 MeV	316 MeV–1 GeV	1–3.16 GeV	3.16–10 GeV	10–31.6 GeV	31.6–100 GeV	100 GeV–316 GeV
0010+1058	III ZW 2	<0.54	$(3.5 \pm 1.0) \times 10^{-2}$	$<2.0 \times 10^{-3}$	...	...	...	...
0035+5950	1ES 0033+595	<1.3	$(4.5 \pm 1.4) \times 10^{-2}$	$(48.0 \pm 9.9) \times 10^{-4}$	$(5.2 \pm 1.2) \times 10^{-4}$	$(7.8 \pm 2.0) \times 10^{-5}$	$(7.0 \pm 3.3) \times 10^{-6}$	$<1.9 \times 10^{-6}$
0048+3157	Mkn 348	...	...	$<6.7 \times 10^{-4}$	...	$<2.7 \times 10^{-5}$	$<3.1 \times 10^{-6}$	...
0120−2701	1Jy 0118−272	0.95 ± 0.16	$(11.4 \pm 0.9) \times 10^{-2}$	$(12.0 \pm 1.1) \times 10^{-3}$	$(12.0 \pm 1.7) \times 10^{-4}$	$(12.3 \pm 2.8) \times 10^{-5}$	$(5.6 \pm 3.4) \times 10^{-6}$	...
0136+4751	S4 0133+47	4.04 ± 0.23	$(28.9 \pm 1.3) \times 10^{-2}$	$(19.4 \pm 1.3) \times 10^{-3}$	$(11.2 \pm 1.5) \times 10^{-4}$	$<3.4 \times 10^{-5}$	$<6.1 \times 10^{-6}$	...
0204−1701	PKS 0202−17	0.99 ± 0.17	$(59.3 \pm 8.6) \times 10^{-3}$	$(42.4 \pm 7.4) \times 10^{-4}$	$<1.4 \times 10^{-4}$	...	...	$<9.9 \times 10^{-7}$
0210−5101	PKS 0208−512	2.41 ± 0.25	$(18.7 \pm 1.1) \times 10^{-2}$	$(14.0 \pm 1.1) \times 10^{-3}$	$(5.9 \pm 1.2) \times 10^{-4}$	$<3.0 \times 10^{-5}$	$<9.6 \times 10^{-6}$	...
0217+0144	PKS 0215+015	2.29 ± 0.20	$(20.2 \pm 1.2) \times 10^{-2}$	$(18.0 \pm 1.4) \times 10^{-3}$	$(15.0 \pm 1.9) \times 10^{-4}$	$(5.9 \pm 2.1) \times 10^{-5}$	$<7.3 \times 10^{-6}$	...
0221+3556	1Jy 0218+357	4.02 ± 0.25	$(26.7 \pm 1.3) \times 10^{-2}$	$(16.6 \pm 1.3) \times 10^{-3}$	$(13.1 \pm 1.7) \times 10^{-4}$	$(4.8 \pm 1.8) \times 10^{-5}$	$<6.9 \times 10^{-6}$	...
0237+2848	4C 28.07	4.38 ± 0.24	$(31.2 \pm 1.5) \times 10^{-2}$	$(14.5 \pm 1.3) \times 10^{-3}$	$(6.4 \pm 1.3) \times 10^{-4}$	$(1.6 \pm 1.0) \times 10^{-5}$	...	...
0238+1636	PKS 0235+164	7.63 ± 0.30	$(65.1 \pm 1.9) \times 10^{-2}$	$(57.7 \pm 2.3) \times 10^{-3}$	$(41.9 \pm 3.1) \times 10^{-4}$	$(17.7 \pm 3.4) \times 10^{-5}$	$(7.6 \pm 3.8) \times 10^{-6}$	...
0319+4130	NGC 1275	6.83 ± 0.27	$(60.9 \pm 1.8) \times 10^{-2}$	$(63.4 \pm 2.2) \times 10^{-3}$	$(48.7 \pm 3.2) \times 10^{-4}$	$(34.5 \pm 4.4) \times 10^{-5}$	$(25.5 \pm 6.9) \times 10^{-6}$	$<2.9 \times 10^{-6}$
0334−4008	PKS 0332−403	1.85 ± 0.18	$(21.4 \pm 1.1) \times 10^{-2}$	$(15.4 \pm 1.2) \times 10^{-3}$	$(9.6 \pm 1.5) \times 10^{-4}$	$(6.5 \pm 2.0) \times 10^{-5}$	$<6.6 \times 10^{-6}$	...
0336+3218	NRAO 140	<2.8	$(12.3 \pm 2.7) \times 10^{-2}$	$(4.5 \pm 1.3) \times 10^{-3}$	...	...	...	...
0423−0120	PKS 0420−01	4.50 ± 0.33	$(32.9 \pm 1.6) \times 10^{-2}$	$(22.0 \pm 1.5) \times 10^{-3}$	$(13.1 \pm 1.9) \times 10^{-4}$	$(7.0 \pm 2.2) \times 10^{-5}$	...	...
0428−3756	PKS 0426−380	10.2 ± 0.3	$(93.4 \pm 1.9) \times 10^{-2}$	$(91.7 \pm 2.7) \times 10^{-3}$	$(80.9 \pm 4.2) \times 10^{-4}$	$(40.7 \pm 5.0) \times 10^{-5}$	$(21.8 \pm 6.3) \times 10^{-6}$	$<2.4 \times 10^{-6}$
0433+0521	3C 120	<1.3	$(3.9 \pm 1.2) \times 10^{-2}$	$<2.0 \times 10^{-3}$	$<2.2 \times 10^{-4}$	...	...	...
0457−2324	PKS 0454−234	10.6 ± 0.3	$(93.4 \pm 2.0) \times 10^{-2}$	$(72.4 \pm 2.4) \times 10^{-3}$	$(42.1 \pm 3.1) \times 10^{-4}$	$(12.0 \pm 2.8) \times 10^{-5}$	$(7.9 \pm 4.2) \times 10^{-6}$	...
0522−3627	PKS 0521−36	4.42 ± 0.22	$(27.2 \pm 1.3) \times 10^{-2}$	$(16.7 \pm 1.3) \times 10^{-3}$	$(6.5 \pm 1.3) \times 10^{-4}$	$<3.1 \times 10^{-5}$	$<7.9 \times 10^{-6}$	...
0530+1331	PKS 0528+134	3.27 ± 0.34	$(16.2 \pm 1.8) \times 10^{-2}$	$(8.1 \pm 1.3) \times 10^{-3}$	$<3.8 \times 10^{-4}$	...	$<4.7 \times 10^{-6}$	...
0538−4405	PKS 0537−441	13.9 ± 0.3	1.19 ± 0.02	$(11.4 \pm 0.3) \times 10^{-2}$	$(86.6 \pm 4.3) \times 10^{-4}$	$(44.1 \pm 5.2) \times 10^{-5}$	$(26.9 \pm 7.1) \times 10^{-6}$	...
0539−2839	1Jy 0537−286	1.87 ± 0.19	$(49.8 \pm 8.7) \times 10^{-3}$	$(17.2 \pm 5.7) \times 10^{-4}$	$<2.1 \times 10^{-4}$	$<2.8 \times 10^{-5}$	...	...
0623−6436	IRAS-L 06229−643	0.79 ± 0.17	$<2.1 \times 10^{-2}$	...	$<2.0 \times 10^{-4}$	$<1.0 \times 10^{-5}$	...	...
0738+1742	PKS 0735+17	1.45 ± 0.22	$(16.6 \pm 1.2) \times 10^{-2}$	$(16.0 \pm 1.3) \times 10^{-3}$	$(14.7 \pm 1.9) \times 10^{-4}$	$(14.7 \pm 3.2) \times 10^{-5}$	$<9.8 \times 10^{-6}$	...
0746+2549	B2.2 0743+25	1.46 ± 0.20	$(40.4 \pm 9.0) \times 10^{-3}$	$<2.5 \times 10^{-3}$	$<1.8 \times 10^{-4}$	...	...	...
0818+4222	S4 0814+425	2.89 ± 0.20	$(24.4 \pm 1.2) \times 10^{-2}$	$(23.3 \pm 1.4) \times 10^{-3}$	$(15.3 \pm 1.8) \times 10^{-4}$	$(7.8 \pm 2.2) \times 10^{-5}$	...	...
0824+5552	OJ 535	1.11 ± 0.16	$(46.6 \pm 7.4) \times 10^{-3}$	$(13.1 \pm 4.8) \times 10^{-4}$	$<1.7 \times 10^{-4}$	...	...	$<7.4 \times 10^{-7}$
0841+7053	4C 71.07	1.98 ± 0.16	$(76.0 \pm 7.5) \times 10^{-3}$	$(20.2 \pm 5.0) \times 10^{-4}$	$<1.5 \times 10^{-4}$	$<2.5\times 10^{-5}$	...	...
0854+2006	PKS 0851+202	2.78 ± 0.34	$(16.9 \pm 1.3) \times 10^{-2}$	$(11.1 \pm 1.1) \times 10^{-3}$	$(9.3 \pm 1.5) \times 10^{-4}$	$(4.0 \pm 1.7) \times 10^{-5}$	$<7.0 \times 10^{-6}$	...
0915+2933	B2 0912+29	<0.71	$(62.1 \pm 8.4) \times 10^{-3}$	$(72.5 \pm 8.9) \times 10^{-4}$	$(5.0 \pm 1.1) \times 10^{-4}$	$(2.9 \pm 1.5) \times 10^{-5}$	$(5.8 \pm 3.3) \times 10^{-6}$	$<2.4 \times 10^{-6}$
0920+4441	S4 0917+44	5.25 ± 0.21	$(42.4 \pm 1.3) \times 10^{-2}$	$(27.6 \pm 1.4) \times 10^{-3}$	$(16.3 \pm 1.8) \times 10^{-4}$	$(5.4 \pm 1.8) \times 10^{-5}$	...	...
0923−2135	PKS 0921−213	0.77 ± 0.21	$<2.2 \times 10^{-2}$	$<1.5 \times 10^{-3}$	...	...	...	...
0957+5522	4C 55.17	2.50 ± 0.16	$(27.5 \pm 1.1) \times 10^{-2}$	$(30.7 \pm 1.4) \times 10^{-3}$	$(27.2 \pm 2.2) \times 10^{-4}$	$(17.4 \pm 3.0) \times 10^{-5}$	$(14.9 \pm 4.8) \times 10^{-6}$	$<2.0 \times 10^{-6}$
1015+4926	1H 1013+498	1.52 ± 0.15	$(14.8 \pm 0.9) \times 10^{-2}$	$(20.2 \pm 1.2) \times 10^{-3}$	$(18.8 \pm 1.9) \times 10^{-4}$	$(16.6 \pm 3.0) \times 10^{-5}$	$(14.9 \pm 4.9) \times 10^{-6}$	$(1.8 \pm 1.0) \times 10^{-6}$
1058+5628	1RXSJ 105837.5+562816	1.04 ± 0.15	$(10.1 \pm 0.8) \times 10^{-2}$	$(12.1 \pm 0.9) \times 10^{-3}$	$(10.7 \pm 1.4) \times 10^{-4}$	$(9.8 \pm 2.2) \times 10^{-5}$	$(13.1 \pm 4.4) \times 10^{-6}$	$<7.7 \times 10^{-7}$
1058+0133	4C 01.28	3.45 ± 0.36	$(25.8 \pm 1.4) \times 10^{-2}$	$(19.8 \pm 1.5) \times 10^{-3}$	$(10.4 \pm 1.7) \times 10^{-4}$	$(8.3 \pm 2.5) \times 10^{-5}$	$(6.2 \pm 3.6) \times 10^{-6}$	...
1058−8003	PKS 1057−79	1.18 ± 0.23	$(11.5 \pm 1.1) \times 10^{-2}$	$(72.8 \pm 8.8) \times 10^{-4}$	$(32.3 \pm 9.2) \times 10^{-5}$	$<2.6 \times 10^{-5}$	...	...
1104+3812	Mkn 421	5.38 ± 0.21	$(59.2 \pm 1.5) \times 10^{-2}$	$(74.1 \pm 2.3) \times 10^{-3}$	$(94.8 \pm 4.4) \times 10^{-4}$	$(97.0 \pm 7.4) \times 10^{-5}$	$(15.0 \pm 1.6) \times 10^{-5}$	$(18.6 \pm 3.4) \times 10^{-6}$
1127−1857	PKS 1124−186	2.97 ± 0.24	$(23.6 \pm 1.3) \times 10^{-2}$	$(17.0 \pm 1.4) \times 10^{-3}$	$(8.6 \pm 1.5) \times 10^{-4}$	$(5.5 \pm 2.0) \times 10^{-5}$	$<6.2 \times 10^{-6}$	...
1130−1449	PKS 1127−145	2.91 ± 0.23	$(11.6 \pm 1.1) \times 10^{-2}$	$(55.5 \pm 8.7) \times 10^{-4}$	...	...	...	...
1131+3114	B2 1128+31	...	$<1.3 \times 10^{-2}$	$<8.8 \times 10^{-4}$	...	...	...	...
1136+7009	S5 1133+704	<0.42	$(22.5 \pm 5.3) \times 10^{-3}$	$(28.0 \pm 5.1) \times 10^{-4}$	$(28.6 \pm 7.4) \times 10^{-5}$	$(4.4 \pm 1.4) \times 10^{-5}$	$(5.1 \pm 2.7) \times 10^{-6}$	...
1153+4931	4C 49.22	0.65 ± 0.14	$(42.8 \pm 6.6) \times 10^{-3}$	$(24.1 \pm 5.5) \times 10^{-4}$	$<1.3 \times 10^{-4}$	$<1.7 \times 10^{-5}$	...	...
1159+2914	4C 29.45	5.11 ± 0.23	$(37.4 \pm 1.4) \times 10^{-2}$	$(30.0 \pm 1.6) \times 10^{-3}$	$(14.5 \pm 1.8) \times 10^{-4}$	$(6.7 \pm 2.1) \times 10^{-5}$	...	...
1217+3007	ON 325	1.82 ± 0.28	$(17.5 \pm 1.5) \times 10^{-2}$	$(19.1 \pm 1.4) \times 10^{-3}$	$(15.2 \pm 1.9) \times 10^{-4}$	$(10.9 \pm 2.6) \times 10^{-5}$	$(7.7 \pm 4.1) \times 10^{-6}$	$<2.6 \times 10^{-6}$

Table 19. contunied.

J2000.0 name	Source name	Flux density (10^{-10} ph cm^{-2} s^{-1} MeV^{-1})						
		100–316 MeV	316 MeV–1 GeV	1–3.16 GeV	3.16–10 GeV	10–31.6 GeV	31.6–100 GeV	100 GeV–316 GeV
1221+2813	ON 231	1.54 ± 0.27	$(16.9 \pm 1.2) \times 10^{-2}$	$(17.8 \pm 1.3) \times 10^{-3}$	$(13.0 \pm 1.7) \times 10^{-4}$	$(11.2 \pm 2.7) \times 10^{-5}$	$(11.4 \pm 4.8) \times 10^{-6}$	...
1222+0413	PKS 1219+04	1.86 ± 0.32	$(13.1 \pm 1.3) \times 10^{-2}$	$(36.4 \pm 7.8) \times 10^{-4}$	$<1.3 \times 10^{-4}$	$<3.4 \times 10^{-5}$	$<7.5 \times 10^{-6}$	$<1.0 \times 10^{-6}$
1229+0203	3C 273	24.1 ± 0.5	1.29 ± 0.02	$(57.3 \pm 2.3) \times 10^{-3}$	$(15.0 \pm 2.0) \times 10^{-4}$	$(4.0 \pm 1.8) \times 10^{-5}$	...	...
1246−2547	PKS 1244−255	4.97 ± 0.26	$(42.3 \pm 1.7) \times 10^{-2}$	$(30.7 \pm 1.7) \times 10^{-3}$	$(16.2 \pm 2.1) \times 10^{-4}$	$(2.6 \pm 1.5) \times 10^{-5}$	...	...
1248+5820	PG 1246+586	1.02 ± 0.14	$(10.1 \pm 0.8) \times 10^{-2}$	$(11.5 \pm 0.9) \times 10^{-3}$	$(11.7 \pm 1.5) \times 10^{-4}$	$(7.9 \pm 2.0) \times 10^{-5}$	$(13.3 \pm 4.6) \times 10^{-6}$	...
1256−0547	3C 279	18.8 ± 0.4	1.37 ± 0.02	$(88.7 \pm 2.8) \times 10^{-3}$	$(45.9 \pm 3.4) \times 10^{-4}$	$(20.9 \pm 3.8) \times 10^{-5}$	...	...
1310+3220	1Jy 1308+326	3.04 ± 0.23	$(21.2 \pm 1.1) \times 10^{-2}$	$(16.3 \pm 1.2) \times 10^{-3}$	$(9.8 \pm 1.5) \times 10^{-4}$	$(3.2 \pm 1.4) \times 10^{-5}$	$<5.2 \times 10^{-6}$	...
1350+0940	GB6B 1347+0955	<0.19	$<1.3 \times 10^{-2}$	...	$<1.1 \times 10^{-4}$	$<8.9 \times 10^{-6}$	...	...
1407−2701	1WGAJ 1407.5−2700	...	...	...	...	$(2.3 \pm 1.3) \times 10^{-5}$	...	...
1427+2348	PG 1424+240	2.42 ± 0.30	$(25.8 \pm 1.3) \times 10^{-2}$	$(33.3 \pm 1.7) \times 10^{-3}$	$(38.0 \pm 2.9) \times 10^{-4}$	$(46.0 \pm 5.4) \times 10^{-5}$	$(46.4 \pm 9.5) \times 10^{-6}$	$(2.1 \pm 1.2) \times 10^{-6}$
1504+1029	PKS 1502+106	20.1 ± 0.4	1.79 ± 0.03	$(13.8 \pm 0.3) \times 10^{-3}$	$(81.1 \pm 4.3) \times 10^{-4}$	$(21.3 \pm 3.8) \times 10^{-5}$	$(6.8 \pm 4.0) \times 10^{-6}$	...
1507+0415	BZQJ1507+0415	...	...	...	...	...	...	$<2.9 \times 10^{-6}$
1517−2422	AP Lib	2.15 ± 0.32	$(21.1 \pm 1.5) \times 10^{-2}$	$(15.0 \pm 1.4) \times 10^{-3}$	$(16.7 \pm 2.1) \times 10^{-4}$	$(15.6 \pm 3.3) \times 10^{-5}$	$<7.2 \times 10^{-6}$	...
1555+1111	PG 1553+113	2.15 ± 0.33	$(26.2 \pm 1.5) \times 10^{-2}$	$(36.5 \pm 1.9) \times 10^{-3}$	$(54.1 \pm 3.6) \times 10^{-4}$	$(62.7 \pm 6.3) \times 10^{-5}$	$(6.6 \pm 1.1) \times 10^{-5}$	$(5.7 \pm 2.0) \times 10^{-6}$
1625−2527	OS −237.8	6.72 ± 1.14	$(50.3 \pm 3.1) \times 10^{-2}$	$(29.0 \pm 2.1) \times 10^{-3}$	$(9.7 \pm 1.8) \times 10^{-4}$	$(4.6 \pm 2.0) \times 10^{-5}$	...	...
1635+3808	4C 38.41	9.58 ± 0.52	$(68.2 \pm 2.0) \times 10^{-2}$	$(40.4 \pm 1.8) \times 10^{-3}$	$(12.9 \pm 1.7) \times 10^{-4}$	$(3.7 \pm 1.5) \times 10^{-5}$	...	...
1640+3946	NRAO 512	<6.4	$(17.6 \pm 3.2) \times 10^{-2}$	$(14.7 \pm 1.7) \times 10^{-3}$	$(8.3 \pm 1.5) \times 10^{-4}$	$(1.9 \pm 1.1) \times 10^{-5}$	...	...
1642+3948	3C 345	...	...	...	...	...	$<8.3 \times 10^{-6}$	...
1653+3945	Mkn 501	1.25 ± 0.33	$(16.9 \pm 1.1) \times 10^{-2}$	$(21.2 \pm 1.3) \times 10^{-3}$	$(25.1 \pm 2.3) \times 10^{-4}$	$(27.6 \pm 4.0) \times 10^{-5}$	$(42.8 \pm 8.5) \times 10^{-6}$	$(6.5 \pm 2.0) \times 10^{-6}$
1751+0939	OT 081	2.07 ± 0.40	$(23.0 \pm 1.7) \times 10^{-2}$	$(16.7 \pm 1.5) \times 10^{-3}$	$(7.8 \pm 1.5) \times 10^{-4}$	$(3.9 \pm 1.7) \times 10^{-5}$	...	...
1800+7828	S5 1803+784	2.51 ± 0.16	$(14.4 \pm 0.9) \times 10^{-2}$	$(10.9 \pm 0.9) \times 10^{-3}$	$(8.2 \pm 1.2) \times 10^{-4}$	$(4.6 \pm 1.5) \times 10^{-5}$	$<4.8 \times 10^{-6}$	...
1833−2103	PKSB 1830−210	19.5 ± 0.6	1.17 ± 0.03	$(60.7 \pm 2.7) \times 10^{-3}$	$(17.2 \pm 2.2) \times 10^{-4}$	$(5.6 \pm 2.0) \times 10^{-5}$	...	$<9.9 \times 10^{-7}$
1840−7709	PKS 1833−77	<0.68	...	$<9.5 \times 10^{-4}$	$<1.0 \times 10^{-4}$	...	...	...
1911−2006	2E 1908.2−201	4.23 ± 0.34	$(32.0 \pm 1.8) \times 10^{-2}$	$(20.8 \pm 1.6) \times 10^{-3}$	$(7.1 \pm 1.5) \times 10^{-4}$	...	...	...
1923−2104	PMNJ 1923−2104	3.93 ± 0.31	$(32.0 \pm 1.7) \times 10^{-2}$	$(27.2 \pm 1.7) \times 10^{-3}$	$(16.5 \pm 2.1) \times 10^{-4}$	$(3.6 \pm 1.7) \times 10^{-5}$	...	$<2.5 \times 10^{-6}$
1924−2914	OV −236	3.28 ± 0.32	$(16.4 \pm 1.4) \times 10^{-2}$	$(10.2 \pm 1.2) \times 10^{-3}$	$(5.0 \pm 1.3) \times 10^{-4}$	$<5.7 \times 10^{-5}$	...	...
1959+6508	1ES 1959+650	2.19 ± 0.19	$(16.9 \pm 1.1) \times 10^{-2}$	$(13.6 \pm 1.1) \times 10^{-3}$	$(12.4 \pm 1.5) \times 10^{-4}$	$(17.9 \pm 2.9) \times 10^{-5}$	$(17.1 \pm 5.0) \times 10^{-6}$	$(14.8 \pm 9.2) \times 10^{-7}$
2009−4849	1Jy 2005−489	<0.71	$(75.5 \pm 9.6) \times 10^{-3}$	$(9.3 \pm 1.0) \times 10^{-3}$	$(9.6 \pm 1.5) \times 10^{-4}$	$(10.4 \pm 2.6) \times 10^{-5}$	$(8.6 \pm 4.2) \times 10^{-6}$	$(2.8 \pm 1.4) \times 10^{-6}$
2056−4714	PKS 2052−47	6.48 ± 0.02	$(2.6 \pm 1.5) \times 10^{-2}$	$(24.7 \pm 1.5) \times 10^{-3}$	$(11.3 \pm 1.6) \times 10^{-4}$	$(5.8 \pm 1.9) \times 10^{-5}$	...	...
2143+1743	S3 2141+17	6.50 ± 0.33	$(32.5 \pm 1.6) \times 10^{-2}$	$(18.0 \pm 1.4) \times 10^{-3}$	$(5.1 \pm 1.2) \times 10^{-4}$	$<1.5 \times 10^{-5}$	...	...
2147+0929	1Jy 2144+092	3.85 ± 0.27	$(21.8 \pm 1.3) \times 10^{-2}$	$(11.7 \pm 1.2) \times 10^{-3}$	$(3.3 \pm 1.0) \times 10^{-4}$	$(2.5 \pm 1.3) \times 10^{-5}$	...	...
2148+0657	4C 06.69	<1.1	$(2.9 \pm 0.9) \times 10^{-2}$	$(22.3 \pm 7.0) \times 10^{-4}$	$<1.3 \times 10^{-4}$	...	...	...
2151−3027	PKS 2149−307	1.74 ± 0.30	$(6.1 \pm 1.1) \times 10^{-2}$	$<2.5 \times 10^{-3}$	...	...	...	...
2202+4216	BL Lac	6.23 ± 0.28	$(47.5 \pm 1.7) \times 10^{-2}$	$(33.1 \pm 1.7) \times 10^{-3}$	$(18.4 \pm 2.0) \times 10^{-4}$	$(9.0 \pm 2.3) \times 10^{-5}$	$(5.1 \pm 3.0) \times 10^{-6}$	...
2203+3145	4C 31.63	1.14 ± 0.36	$<3.4 \times 10^{-2}$	$(20.8 \pm 7.0) \times 10^{-4}$	...	...	...	...
2207−5346	PKS 2204−54	0.90 ± 0.16	$(5.8 \pm 0.8) \times 10^{-2}$	$(34.4 \pm 6.6) \times 10^{-4}$	$(13.5 \pm 6.4) \times 10^{-5}$	...	$<7.1 \times 10^{-6}$	...
2209−4710	NGC 7213	0.66 ± 0.16	$<3.2 \times 10^{-2}$	$<1.4 \times 10^{-3}$	...	$<7.9 \times 10^{-6}$	$<2.5 \times 10^{-6}$	...
2229−0832	PKS 2227−08	5.73 ± 0.26	$(31.9 \pm 1.5) \times 10^{-2}$	$(17.2 \pm 1.4) \times 10^{-3}$	$(3.67 \pm 1.0) \times 10^{-4}$	$(1.9 \pm 1.2) \times 10^{-5}$	$<2.7 \times 10^{-6}$	...
2230−3942	PKS 2227−399	...	...	...	...	...	$<5.2\times 10^{-6}$	$<9.1 \times 10^{-7}$
2232+1143	4C 11.69	3.84 ± 0.26	$(20.1 \pm 1.3) \times 10^{-2}$	$(10.9 \pm 1.1) \times 10^{-3}$	$(3.5 \pm 1.0) \times 10^{-4}$	$(1.8 \pm 1.1) \times 10^{-5}$	...	...
2253+1608	3C 454.3	88.0 ± 0.6	6.43 ± 0.05	$(38.9 \pm 0.5) \times 10^{-2}$	$(13.9 \pm 0.6) \times 10^{-3}$	$(21.9 \pm 3.8) \times 10^{-5}$	$<6.6 \times 10^{-6}$	...
2327+0940	PKS 2325+093	2.93 ± 0.24	$(17.7 \pm 1.3) \times 10^{-2}$	$(70.1 \pm 9.5) \times 10^{-4}$	$<2.6 \times 10^{-4}$	...	...	$<1.0 \times 10^{-6}$
2347+5142	1ES 2344+514	<0.87	$(39.5 \pm 9.5) \times 10^{-3}$	$(60.9 \pm 8.7) \times 10^{-4}$	$(33.3 \pm 9.2) \times 10^{-5}$	$(5.4 \pm 1.7) \times 10^{-5}$	$(7.5 \pm 3.6) \times 10^{-6}$	$(11.1 \pm 7.9) \times 10^{-7}$

Notes. Columns 1 and 2: source name; Cols. 3–9: *Fermi*-LAT flux densities in seven energy bands.

the ROSAT/RASS sample, to be compared with $\langle \alpha_{\rm R-O(Thermal)} \rangle = -0.73 \pm 0.02$ for the *Fermi*-LAT sample.

To assess the possible presence of a thermal component in the X-ray emission, for each source we compare the predicted thermal emission from accretion with the actual X-ray spectrum, and we also include the uncertainties in the parameters of Eq. (2) in determining the uncertainties given by 1, 2, and 3σ bands. We therefore define the following X-ray thermal contamination flags:

- 0: no X-ray data available;
- 1: X-ray emission mostly or entirely due to accretion/reflection (data agree with the expectations for accretion emission within 1σ);
- 2: X-ray emission probably contaminated by the accretion component (data agree with with the expectations for accretion emission within 2σ);
- 3: X-ray emission mostly of non-thermal origin (data are at 2–3σ from the expectations for radio quiet QSOs);
- 4: X-ray emission certainly of non-thermal origin (data are more than 3σ away from the expectations for radio quiet QSOs).

Results for all the FSRQs with good or excellent optical data are shown in Fig. 9, and summarized in Table 21 for the whole sample and each sample independently. We considered as contaminated all the sources with X-ray thermal contamination flag $\leq$2. There is a large difference between the *Fermi*-LAT and *Swift*-BAT samples, where $\lesssim$15% of the sources have a thermal component in their X-ray emission, and the ROSAT/RASS sample, where ~50% of the sources are contaminated. This demonstrates that the thermal component in the X-ray emission of blazars cannot be neglected, even in bright sources.

5.2. SED parameter estimation

We used the SEDs of all the objects in our samples to estimate the values of important physical parameters such as $\nu^{\rm S}_{\rm peak}$, $\nu^{\rm S}_{\rm peak} F(\nu^{\rm S}_{\rm peak})$, $\nu^{\rm IC}_{\rm peak}$, and $\nu^{\rm IC}_{\rm peak} F(\nu^{\rm IC}_{\rm peak})$ (see Table 22) taking into account only the non-thermal radiation and fitting third-degree polynomials as described in Abdo et al. (2010a) (see Figs. 5–7 for examples).

For the sources that were not detected by *Fermi*-LAT even in the 27-month integration, we estimated limits of $\nu^{\rm IC}_{\rm peak}$ and $\nu^{\rm IC}_{\rm peak} F(\nu^{\rm IC}_{\rm peak})$ by constraining the polynomial in the high-energy part of the SED with the 27-month *Fermi*-LAT upper limits, as shown in Fig. 10.

In some HSP BL Lacs with particularly high $\nu^{\rm S}_{\rm peak}$ values (see, e.g., Figs. 30, 31, 36, and 38) the *Fermi*-LAT data alone are insufficient to ensure a good measure of $\nu^{\rm IC}_{\rm peak}$, as the spectra are still rising at the highest *Fermi*-LAT energies and no simultaneous TeV data are available. The $\nu^{\rm IC}_{\rm peak}$ values for these sources should therefore be considered as lower limits.

6. The spectral slope of blazars in the radio-microwave region

While WMAP results are consistent with a single flat spectral index in the relatively narrow frequency range 23–94 GHz (Wright et al. 2009; Gold et al. 2011), the blazar spectrum must steepen at frequencies closer to the synchrotron peak. Adding *Planck* data and simultaneous ground-based observations at centimetre wavelengths to the WMAP data improves the spectral coverage, and allows us to probe the spectral shape of blazars over the much wider frequency range ~1 GHz to ~1 THz.

We studied the low frequency (LF) and the high frequency (HF) regions of the centimetre to sub-millimetre blazar spectra separately to search for differences in the spectral index α and determine the frequency at which the spectral index changes. We fitted the two frequency regions independently with power-laws to estimate the spectral indices at both low frequencies ($\alpha_{\rm LF}$, for $\nu \leq \nu_{\rm Break}$) and high frequencies ($\alpha_{\rm HF}$, for $\nu > \nu_{\rm Break}$), assuming a range of break frequency values, $\nu_{\rm Break}$, from 30 GHz to 100 GHz. In Fig. 11, we show the distributions of $\alpha_{\rm LF}$ and $\alpha_{\rm HF}$ for $\nu_{\rm Break} = 70$ GHz and 100 GHz; the blazar spectra steepen from $\alpha_{\rm LF} \sim 0$ to $\alpha_{\rm HF} \sim -0.65$.

To verify the robustness of the results we repeated the analysis by imposing the two minimum numbers of independent frequencies needed to perform the fit, namely 3 and 5, and the results are consistent (Table 23).

We also analyzed the different classes of blazars – flat spectrum radio quasars (FSRQ), BL Lac objects (BL Lac), and radio-loud AGN of unknown classification (Uncertain Type) – separately, and we have found a difference at a level of about 3σ in $\alpha_{\rm HF}$, which is ~−0.7 for FSRQ but ~−0.5 for BL Lacs.

The spectral steepening and the difference in $\alpha_{\rm HF}$ are visible in Fig. 12, where we show $\alpha_{\rm LF}$ versus (vs.) $\alpha_{\rm HF}$ for the sources that meet the requirements for the minimum amount of independent data at both low and high frequencies.

Our results are in complete agreement with the findings of Planck Collaboration (2011e) for the radio selected sample, i.e., flat spectral index at low frequency and $\alpha_{\rm HF} \sim -0.6$ at high frequency with a break frequency ~70 GHz, suggesting that this is a general feature of all blazars regardless of the selection criteria. There is also general agreement with the results presented in Planck Collaboration (2011d) for all the sources in the *Planck* ERCSC catalogs, and the slight discrepancy in the spectral index estimated at low frequency can be explained by the fact that, unlike Planck Collaboration (2011d), we have included the ground-based observations at 5–30 GHz.

7. Searching for correlations between fluxes in different energy bands

We used our simultaneous and average multi-frequency data to identify possible correlations between fluxes measured in different energy bands. As some of the blazars in our samples were not detected by either *Fermi*-LAT or *Planck*, we estimated the significance of the correlations using the ASURV code Rev1.2 (Lavalley et al. 1992), which takes account of upper limits as described in Isobe et al. (1986). We search for possible correlations using fluxes or flux-densities rather than in luminosity-luminosity space because this allows us to use all objects in the samples, including those with no redshift (and consequently luminosity) information.

7.1. Microwave vs. X-ray

Figure 13 shows the *Planck* 143 GHz flux density versus the simultaneous *Swift*-XRT X-ray flux for all the sources where the X-rays are expected to be due to the inverse Compton component (that is all LSP blazars) and not significantly contaminated by X-ray emission that is unrelated to the jet, such as that produced by the accretion process (see Sect. 5.1 for details). Sources that were not detected by *Planck* are plotted as upper limits; all the sources were detected in the X-ray band.

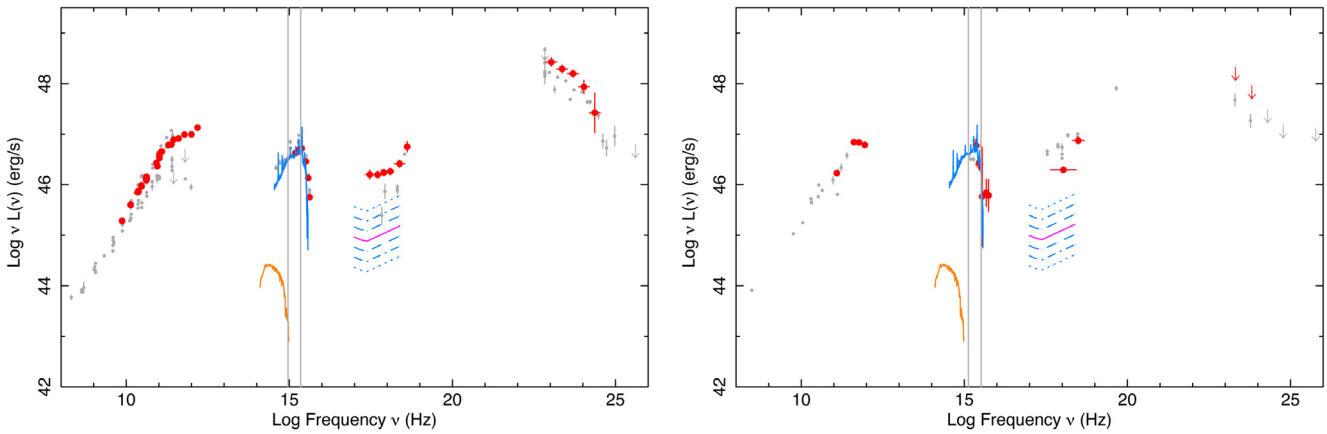

Fig. 7. The SEDs of 4C 38.41 (z = 1.814; *left*) and 1Jy 0537−286 (z = 3.104; *right*). Simultaneous data are shown in red; non-simultaneous literature or archival data are shown in light gray. Note that the UVOT data of these medium and high redshift objects matches quite well the QSO template of Vanden Berk et al. (2001) that we use to estimate the thermal emission from the blue bump (blue line). The emission from the host galaxy (orange line) is very low compared to other components. The observed X-ray emission from these sources is more than 3σ above the expected emission from accretion derived from Eq. (2). In both cases, the optical light is dominated by radiation from the accretion while the X-rays originate from the non-thermal component.

Table 20. *Fermi*-LAT data at one bin/decade integrated over 27 months.

		Flux density (10^{-10} ph cm^{-2} s^{-1} MeV^{-1})		
J2000.0 name	Source name	100 Mev–1 GeV	1–10 GeV	10–100 GeV
0017+8135	S5 0014+813	$<8.7 \times 10^{-2}$	$<1.8 \times 10^{-4}$	...
0214+5144	GB6J 0214+5145	$<6.7 \times 10^{-2}$	$<4.2 \times 10^{-4}$	$<6.4 \times 10^{-6}$
0217+7349	1Jy 0212+735	$(28.1 \pm 3.8) \times 10^{-2}$	$(4.8 \pm 1.7) \times 10^{-4}$	$<3.7 \times 10^{-6}$
0550−3216	PKS 0548−322	$<5.8 \times 10^{-2}$	$<4.7 \times 10^{-4}$	$(4.6 \pm 2.8) \times 10^{-6}$
1147−3812	PKS 1144−379	$(23.1 \pm 3.0) \times 10^{-2}$	$(15.7 \pm 2.2) \times 10^{-4}$	$<8.3 \times 10^{-6}$
1220+0203	PKS 1217+02	$(12.3 \pm 3.6) \times 10^{-2}$	$<4.9 \times 10^{-4}$	$<5.8 \times 10^{-6}$
1305−1033	1Jy 1302−102	$<6.0 \times 10^{-2}$	...	...
1419+0628	3C 298.0	<0.10	$<4.0 \times 10^{-4}$	...
1423+5055	BZQJ 1423+5055	$<4.2 \times 10^{-2}$	...	...
1456+5048	1RXSJ 145603.4+504825	<0.12	...	$<6.5 \times 10^{-6}$
1510−0543	4C −05.64	$(45.5 \pm 7.6) \times 10^{-2}$	$(21.3 \pm 2.9) \times 10^{-4}$	$<5.8 \times 10^{-6}$
1603+1554	WE 1601+16W3	...	$<2.5 \times 10^{-4}$	$<4.9 \times 10^{-6}$
1719+4858	ARP 102B	$<4.8 \times 10^{-2}$	$<1.4 \times 10^{-4}$	...
1743+1935	1ES 1741+196	$<7.6 \times 10^{-2}$	$(9.5 \pm 1.9) \times 10^{-4}$	$(5.8 \pm 3.2) \times 10^{-6}$
2129−1538	1Jy 2126−158	<0.11	$<3.5 \times 10^{-4}$	...
2303−1842	PKS 2300−18	...	$<2.7 \times 10^{-4}$	$<2.3 \times 10^{-6}$
2333−2343	PKS 2331−240	$<9.5 \times 10^{-2}$	$<4.3 \times 10^{-4}$	$<3.7 \times 10^{-6}$

Notes. Column 1 and 2: source name; Cols. 3–9: *Fermi*-LAT flux densities in three energy bands.

Table 21. Contamination of the X-ray emission from a thermal component and $\langle\alpha_{\rm R-O(Thermal)}\rangle$ estimated for FSRQs in the whole sample and for each sample independently, for various thresholds on the quality of the optical data.

	ALL			*Fermi*-LAT			*Swift*-BAT			ROSAT/RASS		
Opt Data quality	cont/ total	%	$\langle\alpha_{\rm R-O(Thermal)}\rangle$	cont/ total	%	$\langle\alpha_{\rm R-O(Thermal)}\rangle$	cont/ total	%	$\langle\alpha_{\rm R-O(Thermal)}\rangle$	cont/ total	%	$\langle\alpha_{\rm R-O(Thermal)}\rangle$
ALL	10/47	21	-0.69 ± 0.02	3/25	12	-0.72 ± 0.02	2/21	10	-0.70 ± 0.03	6/13	46	-0.65 ± 0.04
≥2	10/44	23	-0.69 ± 0.02	3/22	14	-0.73 ± 0.02	2/20	10	-0.70 ± 0.03	6/13	46	-0.65 ± 0.04
3	9/40	23	-0.69 ± 0.02	3/22	14	-0.73 ± 0.02	1/16	6	-0.69 ± 0.04	6/12	50	-0.64 ± 0.05

Notes. We have considered as contaminated sources all those with X-ray thermal contamination flag ≤2 (see the text for a description of the flags).

A correlation, although with some scatter, is clearly present. The Spearman rank coefficients (ρ) and the corresponding probabilities that the observed correlation is the result of chance are given in Table 24. Results obtained using *Planck* flux densities at other frequencies from 30 GHz to 217 GHz are similar and not shown here.

Table 22. Rest-frame $\langle \nu^{S}_{peak} \rangle$ and $\langle \nu^{IC}_{peak} \rangle$ values for different samples and classes.

		Synchrotron peak		inverse Compton peak	
Sample	Class	No. of sources	$\langle \log(\nu_{Peak}) \rangle$	No. of sources	$\langle \log(\nu_{Peak}) \rangle$
	ALL	45	13.34 ± 0.12	42	22.19 ± 0.10
Fermi-LAT	FSRQs	24	13.07 ± 0.07	23	22.21 ± 0.14
	BL Lacs	13	14.11 ± 0.32	11	22.35 ± 0.24
	ALL	26	13.65 ± 0.26	22	21.66 ± 0.28
Swift-BAT	FSRQs	18	13.16 ± 0.09	16	21.45 ± 0.17
	BL Lacs	5	15.75 ± 0.81	3	23.41 ± 1.52
	ALL	25	14.27 ± 0.31	20	22.15 ± 0.38
ROSAT/RASS	FSRQs	11	13.02 ± 0.17	11	21.43 ± 0.30
	BL Lacs	11	15.79 ± 0.28	6	24.24 ± 0.37
	ALL	94	13.20 ± 0.06	77	21.99 ± 0.10
Radio	FSRQs	64	13.08 ± 0.05	49	21.99 ± 0.12
	BL Lacs	14	13.89 ± 0.27	13	22.26 ± 0.20

Table 23. Radio LF and HF spectral index distributions for different values of the break frequency ν_{Break} and of the minimum number of frequency bands considered for the fit.

			Low frequency			High frequency		
ν_{Break}	No. of frequencies	Class	No. of sources	$\langle \alpha_{LF} \rangle$	σ_{LF}	No. of sources	$\langle \alpha_{HF} \rangle$	σ_{HF}
30	3	ALL	47	0.00 ± 0.04	0.27	69	-0.51 ± 0.04	0.30
30	5	ALL	46	0.00 ± 0.04	0.27	57	-0.49 ± 0.03	0.26
44	3	ALL	47	-0.02 ± 0.04	0.25	66	-0.64 ± 0.03	0.26
44	5	ALL	47	-0.02 ± 0.04	0.25	47	-0.62 ± 0.03	0.22
70	3	ALL	63	-0.08 ± 0.03	0.28	66	-0.67 ± 0.03	0.28
70	5	ALL	47	-0.02 ± 0.04	0.25	35	-0.65 ± 0.04	0.22
100	3	ALL	65	-0.11 ± 0.03	0.27	48	-0.56 ± 0.04	0.26
100	5	ALL	47	-0.02 ± 0.04	0.24	15	-0.52 ± 0.05	0.19
70	3	FSRQ	39	-0.11 ± 0.04	0.28	40	-0.73 ± 0.04	0.27
70	3	BL Lac	12	-0.08 ± 0.08	0.29	14	-0.51 ± 0.07	0.27
70	3	Unc. Type	12	-0.02 ± 0.08	0.29	12	-0.64 ± 0.07	0.25

Table 24. Spearman correlation parameters for 143 GHz flux density vs. X-ray flux.

Class	*Fermi*-LAT sample			*Swift*-BAT sample			ROSAT/RASS sample			Radio sample		
	No. of sources (a)/(b)	ρ	P(%)	No. of sources (a)/(b)	ρ	P(%)	No. of sources (a)/(b)	ρ	P(%)	No. of sources (a)/(b)	ρ	P(%)
All	35/3	0.72	<0.01	18/4	0.50	2.34	9/10	0.70	0.30	49/3	0.51	0.03
FSRQs	20/2	0.75	0.06	16/3	0.58	1.40	5/3	0.89	1.85	33/3	0.57	0.08
BL Lacs	8/1	0.95	0.72	2/0	...*	...	1/3	...	...	9/0	0.28	42.29

Notes. [(a)] Number of *Planck* detections. [(b)] Number of *Planck* upper limits. [(*)] The number of detections is too low to allow a reliable estimation of ρ.

7.2. Microwave vs. γ-ray

The relationship between radio or microwave and γ-ray fluxes is a topic that has been addressed several times in the literature. A positive correlation between the radio and γ-ray fluxes is generally found, though with a large scatter (e.g., Kovalev et al. 2009; León-Tavares et al. 2010; Giroletti et al. 2010; Ghirlanda et al. 2010; Mahony et al. 2010; Peel et al. 2011; Linford et al. 2011; Ackermann et al. 2011; León-Tavares et al. 2011b). However, in most cases radio and *non-simultaneous* γ-ray data for sources *detected in both energy bands* are compared. For the first time, we present simultaneous microwave and γ-ray data and take into account upper limits.

The top panel of Fig. 14 shows the simultaneous *Fermi*-LAT γ-ray flux plotted versus the *Planck* flux density at 143 GHz. Sources with TS $<$ 25 in the *Fermi*-LAT data and below 4σ in *Planck* maps are shown as upper limits. The plot shows a clear trend but from Table 25, which gives the Spearman's ρ correlation parameter and the probability P that the observed level of correlation is caused by chance, we see that the level of significance of the correlation is never very high (P is of the order of a few percent and never lower than 0.05%), especially in the hard X-ray and γ-ray selected samples and for BL Lacs. This result is partly due to the large number of upper limits to the simultaneous γ-ray flux, which was estimated typically over a period of one week. To improve the statistics, in the middle panel of Fig. 14 we show the same plot using the *Fermi*-LAT γ-ray flux integrated over a two-month period centered on the time of the *Planck* observations. From Table 25, we see that, although the significance of the correlation in the various samples and blazar classes substantially increases, it is never very high and the scatter remains.

This result may be due to the limited flux dynamic range in the γ-ray band for the *Fermi*-LAT sample and to the small number of objects (in the case of BL Lacs). However, a weak correlation could occur if the microwave flux density represents the superposition of multiple synchrotron components, while the simultaneous γ-ray flux represents the emission from a single

Table 25. Microwave (143 GHz) vs. γ-ray flux correlation parameters.

γ-ray integration period	Class	*Fermi*-LAT sample			*Swift*-BAT sample			ROSAT/RASS sample			Radio sample		
		No. of sources (a)/(b)/(c)	ρ	P(%)	No. of sources (a)/(b)/(c)	ρ	P(%)	No. of sources (a)/(b)/(c)	ρ	P(%)	No. of sources (a)/(b)/(c)	ρ	P(%)
Simult.	All	16/5/32	0.22	12.4	8/6/20	0.42	2.49	6/20/25	0.42	1.42	22/2/71	0.35	0.07
	FSRQs	10/3/16	0.23	23.4	5/2/12	0.39	9.92	4/3/6	0.65	3.97	15/1/46	0.33	1.19
	BL Lacs	5/2/9	0.55	4.76	2/2/2	...*	...	2/11/4	...	...	4/0/10	0.38	17.6
2 months	All	36/5/9	0.29	4.18	11/7/20	0.61	0.07	8/21/18	0.31	6.00	37/3/56	0.40	0.01
	FSRQs	19/3/6	0.17	38.7	6/3/15	0.59	0.89	4/4/9	0.51	6.83	23/2/42	0.36	0.39
	BL Lacs	11/2/1	0.72	0.92	3/3/2	...	...	3/11/5	...	...	10/0/6	0.42	10.2
27 months	All	47/3/0	0.47	0.10	22/16/7	0.67	<0.01	12/23/18	0.40	0.99	75/4/16	0.48	<0.01
	FSRQs	25/3/0	0.48	1.27	16/3/4	0.54	1.59	8/3/7	0.85	0.15	47/2/19	0.48	0.01
	BL Lacs	14/0/0	0.72	0.91	3/4/0	...	...	2/14/2	...	...	16/0/0	0.55	3.22

Notes. [(a)] Number of sources detected both by *Planck* and *Fermi*-LAT. [(b)] Number of *Planck* upper limits. [(c)] Number of *Fermi*-LAT upper limits. [(*)] The number of detections is too low to allow a reliable estimation of ρ.

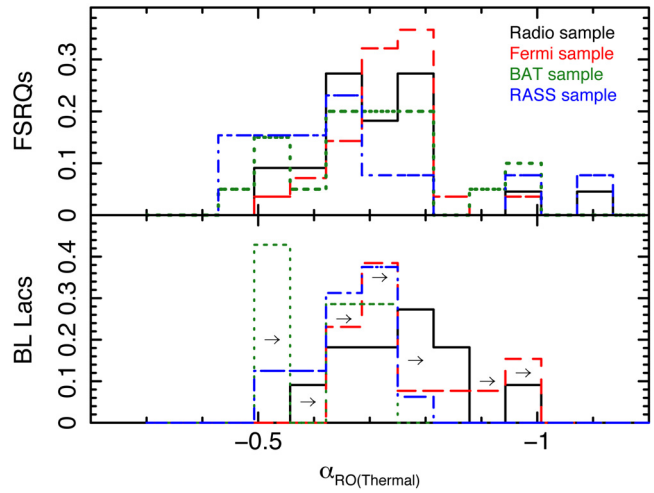

Fig. 8. Distribution of $\alpha_{R-O(Thermal)}$ for all the sources and for each blazar sample. Only SEDs with good or excellent optical data (flag = 2 or 3, see text) were used. Black solid histograms: radio sample; red dashed histograms: *Fermi* sample; green dot-dashed histograms: *Swift* BAT sample; blue dotted histograms: RASS sample. Distributions for BL Lac objects refer to upper limits only.

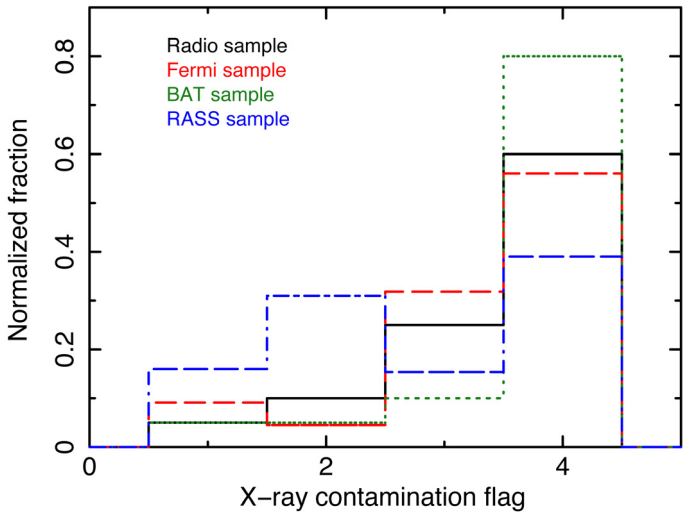

Fig. 9. Distribution of the thermal emission flag for all the FSRQs with good or excellent optical data flag (see text for details). Black solid histograms: radio sample; red dashed histograms: *Fermi*-LAT sample; green dot-dashed histograms: *Swift* BAT sample; and blue dotted histograms: RASS sample. As the X-ray emission of all BL Lacs was not contaminated, the BL Lac data are not plotted here.

dominant component that may be active for only a short time. For this reason, in the bottom panel of Fig. 14, we plot the *Planck* ERCSC flux densities (which in most cases represent the flux density averaged over more than one *Planck* observation) versus the *Fermi*-LAT flux averaged over the entire 27-month period. In this case the correlation is highly significant, although, the many upper limits in both energy bands clearly imply that the dispersion is very large.

7.3. X-ray vs. γ-ray

Figure 15 plots the 2-month γ-ray flux versus the simultaneous X-ray flux for all sources observed by *Swift* that do not show signatures of thermal contamination in the X-ray spectrum. Open red circles represent HSP sources, where the X-ray flux is due to the tail of the synchrotron emission, while black filled circles are LSP and ISP sources for which the X-ray flux is related to the inverse Compton radiation. This distinction is needed in order to properly compare sources where the emission is produced by the same mechanism. We therefore compute the γ-ray vs. X-ray correlation coefficient only for LSP and ISP sources. The

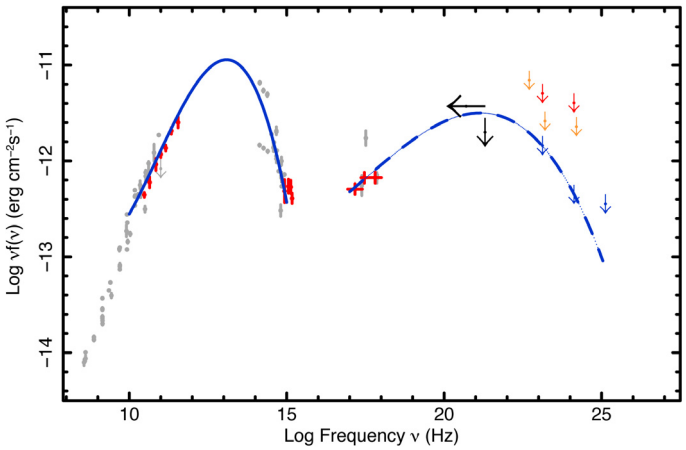

Fig. 10. The SED of the blazar PKS 0003−066, illustrating the estimation of the upper limits to ν^{IC}_{peak} and to $\nu^{IC}_{peak}F(\nu^{IC}_{peak})$ by combining the X-ray data with the 27-month *Fermi*-LAT upper limits.

Spearman rank test shows moderate evidence of a correlation that is less significant in the longer integrations: P = 2.55%

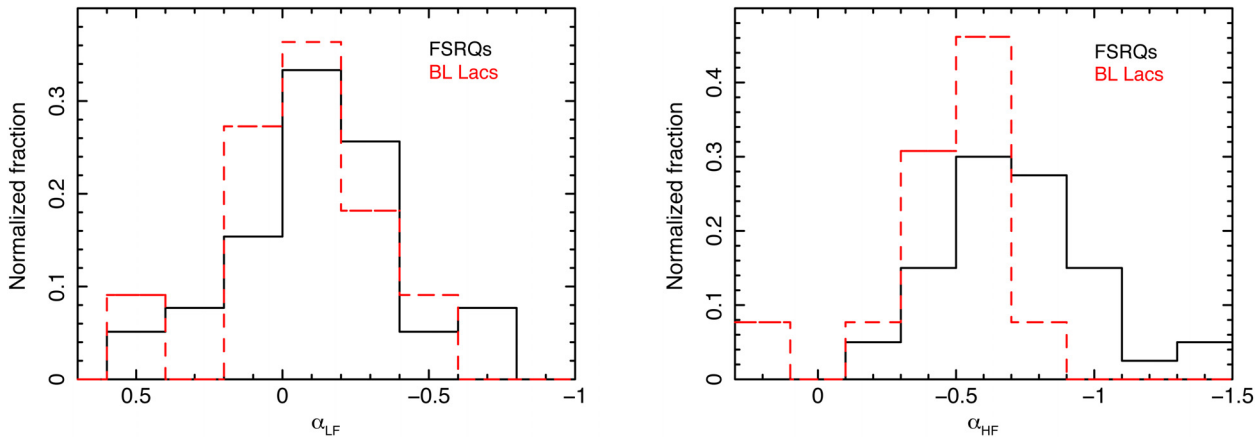

Fig. 11. Radio/microwave low frequency ($\nu < 70$ GHz, LF; *left* side) and high frequency ($\nu > 70$ GHz, HF; *right* side) spectral index distributions of FSRQs and BL Lacs in our samples for the case $\nu_{\rm Break} = 70$ GHz. While the distributions of low frequency spectral indices are very similar for both types of blazars with $\langle\alpha_{\rm LF}\rangle \sim -0.1$, the distributions of the high frequency slopes indicate that the spectra of FSRQs ($\langle\alpha_{\rm HF}\rangle = -0.73 \pm 0.04$) might be somewhat steeper than those of BL Lacs ($\langle\alpha_{\rm HF}\rangle = -0.51 \pm 0.07$). A Kolmogorov Smirnov (KS) test gives a probability of less than 3% that the HF distributions for FSRQs and BL Lacs come from the same parent distribution.

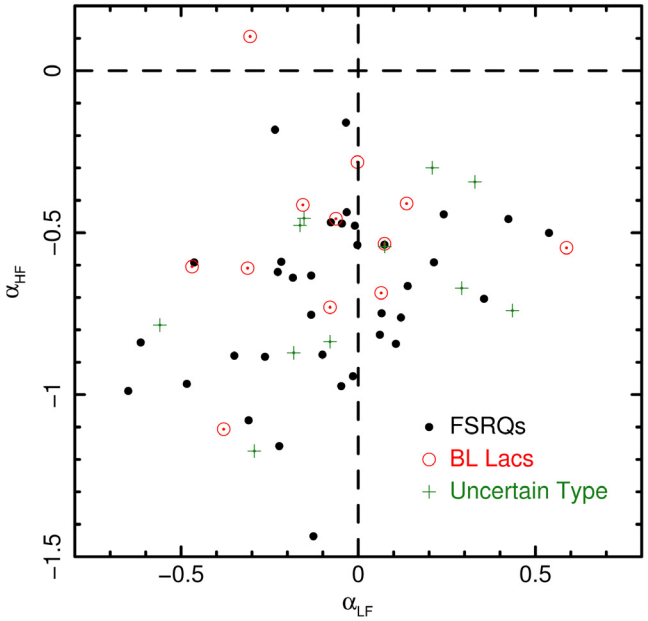

Fig. 12. $\alpha_{\rm HF}$ vs. $\alpha_{\rm LF}$ diagram for $\nu_{\rm Break} = 70$ GHz for different blazar classes: flat spectrum radio quasars (FSRQ), BL Lac objects (BL Lac), and blazars of uncertain classification.

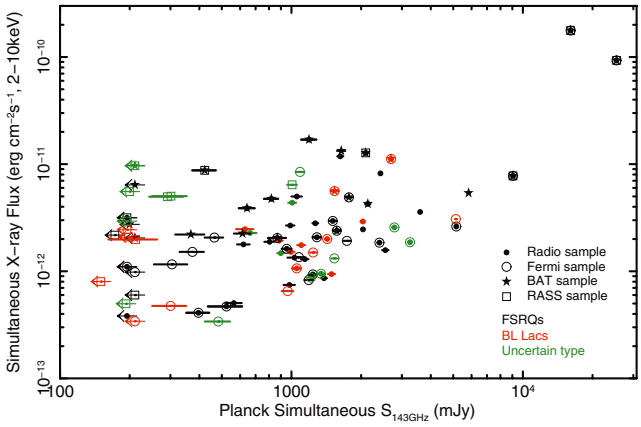

Fig. 13. The *Planck* 143 GHz flux density plotted vs. the simultaneous *Swift* XRT X-ray flux for all sources where the X-ray flux is expected to be due to the inverse Compton component. Blazars with significant X-ray contamination due to accretion have been excluded from the plot.

for simultaneous data, $P = 6.9\%$ for a 2-month integration, or $P = 17.4\%$ for a 27-month integration.

Figure 16 plots the power-law spectral index in the *Swift* XRT energy band (0.3–10 keV) versus the spectral slope in the *Fermi*-LAT γ-ray band (100 MeV–100 GeV) derived using the 2-month γ-ray data. A significant correlation is present, confirming the results of Abdo et al. (2010a). The top right corner of Fig. 16 shows the same plot built with simultaneous γ-ray data; although the number of objects is smaller, the correlation is still present.

8. Discussion and conclusions

We have collected simultaneous *Planck*, *Swift*, *Fermi*-LAT, and ground-based multi-frequency data for 105 blazars included in three statistically well-defined samples characterized by flux limits in the soft X-ray (0.1–2.4 keV, ROSAT), hard X-ray (15–150 keV, *Swift*-BAT), and γ-ray ($E > 100$ MeV, *Fermi*-LAT) energy bands, with the addition of a cut to the radio 5 GHz flux density to ensure a high probability of detection by *Planck*. This study complements a similar study of 104 radio-bright AGN ($f_{37\ \rm GHz} > 1$ Jy) (Planck Collaboration 2011e). Altogether, the four samples contains a total of 175 distinct objects. The acquisition of this unprecedented multi-frequency/multi-satellite data set was possible thanks to cooperation between the *Planck*, *Swift*, and *Fermi*-LAT teams, who agreed to share data and organize an extensive program of multi-frequency observations involving over 160 *Swift* ToO pointings scheduled when the blazars were within the field of view of the *Planck* instruments.

We have used this unique multi-frequency dataset to build well-sampled, simultaneous SEDs of all the blazars included in our high-energy selected samples. This collection of SEDs is an improvement over previous compilations (e.g., Abdo et al. 2010a) because: a) the SEDs presented here are strictly simultaneous, while in Abdo et al. (2010a) the multi-frequency data were collected over a period of up to nine months centered on the first three months of *Fermi*-LAT operations; b) the sources

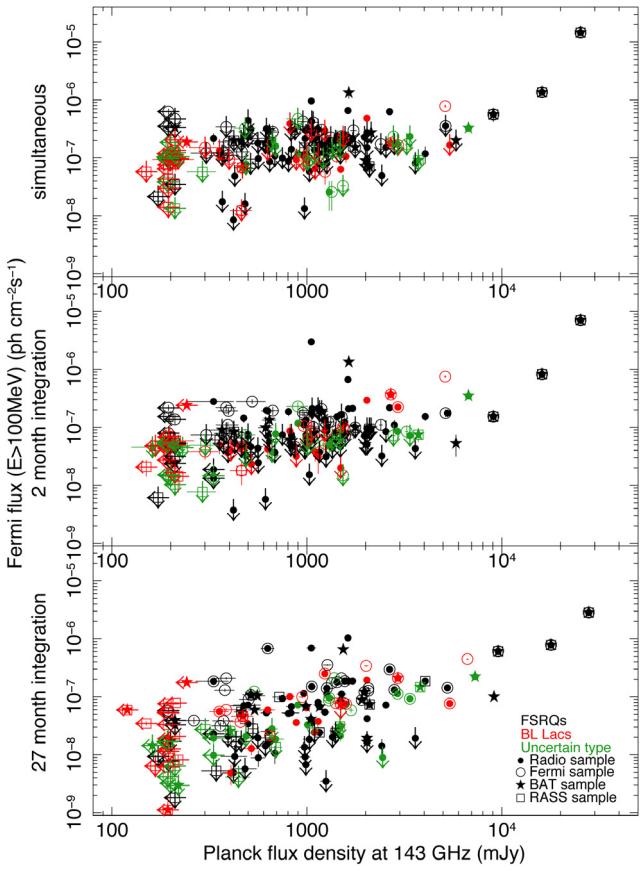

Fig. 14. *Top panel*: the *Planck* flux density at 143 GHz is plotted against the simultaneous *Fermi*-LAT flux. *Middle panel*: the *Planck* flux density at 143 GHz is plotted against the *Fermi*-LAT flux integrated over the 2-month period centered on the *Planck*-*Swift* observations. *Bottom panel*: the *Planck* ERCSC flux density at 143 GHz (flux averaged over more than one *Planck* survey) is plotted versus the γ-ray fluxes averaged over the entire 27 month *Fermi*-LAT observing period.

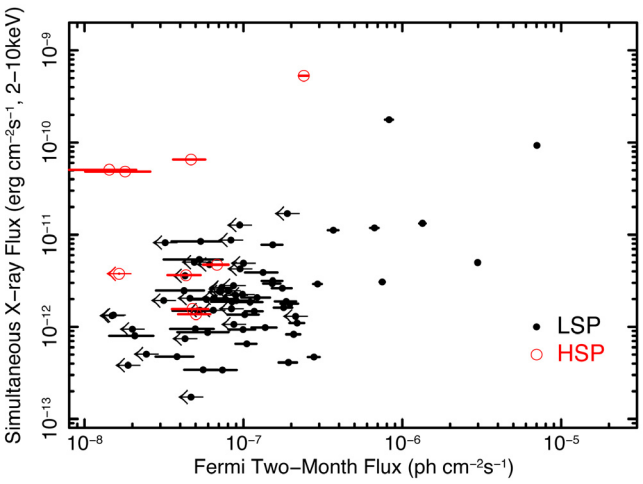

Fig. 15. The *Swift* XRT flux is plotted against the two-month *Fermi*-LAT flux for the sources included in the three high-energy flux-limited samples. Open red circles represent HSP sources, i.e., high synchrotron-peaked BL Lacs where the X-ray flux is dominated by synchrotron radiation. Filled black circles represent LSP sources, i.e., blazars with low synchrotron peak, for which the X-ray flux is dominated by inverse Compton radiation.

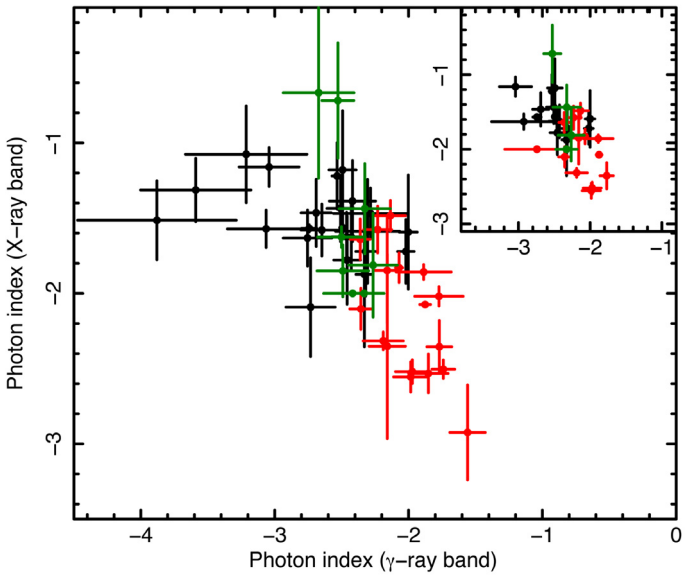

Fig. 16. The power-law spectral index in the *Swift* XRT energy band (0.3–10 keV) is plotted versus the slope in the *Fermi*-LAT γ-ray band (100 MeV–100 GeV) derived using *Fermi*-LAT data integrated over a period of 2 months. The same plot built with simultaneous γ-ray data is shown in the inset at the upper right. A clear anti-correlation is present; the Spearman test gives a probability of less than 0.01% that the correlation is due to chance, even in the simultaneous data.

were selected according to different statistical criteria allowing us to probe the blazar parameter space from widely different viewpoints; and c) we took care to identify and separate radiation components unrelated to the emission from the jet, such as the light from the blazar's host galaxy and the radiation produced by the accretion onto the central black hole, which often contaminate the non-thermal blazar spectrum in the optical, UV, and X-ray bands.

Our findings are broadly consistent with those of Abdo et al. (2010a). However, our analyses of larger samples selected in different parts of the electromagnetic spectrum, wider wavelength coverages, different level of simultaneity, and the ability to separate the emission components, have allowed us to make significant progress in several areas. The use of four widely different samples has allowed us to investigate the consequences of selection effects on the estimation of critical parameters such as $\langle \nu^{S}_{peak} \rangle$, average Compton dominance, especially for the case of BL Lacs.

Some of our sources have been observed simultaneously by *Swift*, *Planck*, and *Fermi*-LAT during more than one *Planck* survey. In these cases, we have presented only the data collected during the first observation. Multiple simultaneous observations of a subset of our blazars and detailed model fitting of the SEDs will be the subject of future papers. The main results of this work are discussed below.

8.1. Fermi-LAT detection statistics and the effects of variability

The percentage of *Fermi*-LAT detected sources during the simultaneous integrations, typically lasting about one week, ranges from $\lesssim$40% in the *Fermi*-LAT sample to 20–25% in the radio and X-ray selected samples (see Table 13). When 2-month integrations centered on the *Planck*-*Swift* observations are considered, these percentages grow to 80% in the *Fermi*-LAT sample and to ~35% in the other samples. However, even when using data from the 27-month *Fermi*-LAT integrations available at the

time of writing, many of the blazars belonging to the radio, and both soft and hard X-ray selected samples remain undetected.

We note that the detection rate is quite different for FSRQs and BL Lacs: if we exclude the *Fermi*-LAT sample where all the objects have been detected (by definition), the percentage of detections is 95% for BL Lacs and only ∼60% for FSRQs, with values ranging from 72% in the radio sample to just 53% in the RASS sample (see Table 14).

A comparison of our simultaneous data with published and archival measurements shows that the use of non-simultaneous data in the SED of blazars typically introduces a scatter of about a factor of two in the microwave band, and a factor of up to ten or more in the X-ray and γ-ray bands.

8.2. The spectral slope in the radio-sub-millimetre region

We confirm that the energy spectrum of blazars in the radio–microwave spectral region is quite flat, with an average slope of $\langle\alpha\rangle \sim 0$ ($f(\nu) \propto \nu^{\alpha}$) up to about 70 GHz, above which it steepens to $\langle\alpha\rangle \sim -0.6$. This behaviour is very similar to that observed in the sample of radio bright blazars considered by Planck Collaboration (2011e; see also Tucci et al. 2011) confirming the findings of Abdo et al. (2010a) that the radio to microwave part of the spectrum is approximately the same in all blazars (FSRQs and BL Lacs) independently of the selection band. However, the spectral slope of BL Lacs above ∼70 GHz is flatter than that of FSRQs with $\langle\alpha_{\rm HF}\rangle = -0.51 \pm 0.07$ for BL Lacs compared to $\langle\alpha_{\rm HF}\rangle = -0.73 \pm 0.04$ for FSRQs (see Table 23 and Fig. 11). A KS test, performed on the subsamples of FSRQs and BL Lacs with radio flux density larger than 1 Jy, gives a probability of less than 3% that the two samples come from the same parent population. This difference in the high frequency spectral index may reflect that the radio-submm part of the spectrum is closer to $\nu^{\rm S}_{\rm peak}$ in LSP than in HSP sources.

8.3. Synchrotron self-absorption

We searched for signatures of synchrotron self-absorption, which in simple homogeneous SSC models is expected to cause strong spectral flattening below ∼100 GHz, but we found no evidence of any common behaviour; indeed, the average spectrum in that region steepens instead of flattening. Possible cases where some evidence of synchrotron self-absorption may be present are PKS 0454−234, PKS 0521−36 (Fig. 27), S4 0917+44 (Fig. 29), PKS 1127−145 (Fig. 31), and 3C 454.3 (Fig. 40).

8.4. Non-thermal versus disk radiation

In several blazars, the optical/UV light is contaminated significantly by thermal/disk radiation (known as the blue bump, see Figs. 6 and 7), while the soft X-ray flux is contaminated by radiation produced in the accretion process in approximately 25% of the blazars in our samples (see Fig. 9). In some of the closest sources, the optical light is instead either contaminated or dominated by the emission from the host galaxy. Ignoring this contamination may cause an overestimate of the position of both $\nu^{\rm S}_{\rm peak}$ and $\nu^{\rm IC}_{\rm peak}$ by 0.5 dex or more.

We investigated the relationship between the radiation produced by accretion and the jet, which co-exist in most FSRQs, using the parameter $\alpha_{\rm R-O(Thermal)}$, defined as the spectral slope between the 5 GHz radio (non-thermal) flux and the 5000 Å optical flux that can be attributed to the blue-bump/disk emission. In the blazar paradigm, this quantity depends on both the amount of relativistic amplification (which only affects the non-thermal radiation from the jet) and the intrinsic ratio of non-thermal/jet radiation to disk emission. We estimated the value of $\alpha_{\rm R-O(Thermal)}$ in all sources for which we had optical data of good quality. Since BL Lacs do not display broad lines, only lower limits to $\alpha_{\rm R-O(Thermal)}$ can be derived.

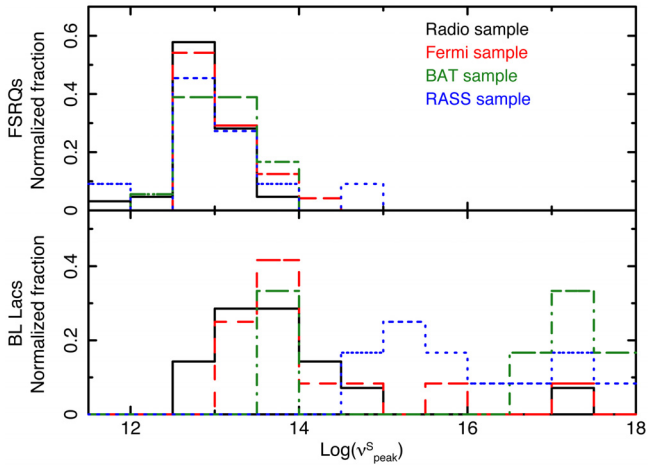

Fig. 17. The rest-frame synchrotron $\nu_{\rm peak}$ distributions of FSRQs and BL Lacs in different samples. Black solid histograms: radio sample; red dashed histograms: *Fermi*-LAT sample; green dot-dashed histograms: *Swift* BAT sample; blue dotted histograms: RASS sample.

Figure 8 shows the distribution of $\alpha_{\rm R-O(Thermal)}$ for all our samples, which range from ∼0.4 to just above 1.0 and have peak values between 0.6 and 0.8. The distributions are all similar, with the largest difference being between the *Fermi*-LAT and the RASS samples (a KS test gives a probability of 3.6% that the two distributions originate from the same parent population), possibly reflecting differences in either the amplification factor or the ratio of accretion to jet emission between γ-ray and soft X-ray selected blazars. We note that the distribution of the $\alpha_{\rm R-O(Thermal)}$ limits for BL Lacs is consistent with intrinsic values of $\alpha_{\rm R-O(Thermal)}$ for BL Lacs that are within the range of values observed in FSRQs.

8.5. The distribution of rest-frame peak energies

The distribution of rest-frame synchrotron peak energies ($\nu^{\rm S}_{\rm peak}$) of FSRQs is very similar in all our samples with a strong peak at $\approx 10^{12.5}$ Hz, an average of $\langle\nu^{\rm S}_{\rm peak}\rangle 10^{13.1\pm0.1}$ Hz, and a dispersion of only ∼0.5 dex. However, for BL Lacs the value of $\langle\nu^{\rm S}_{\rm peak}\rangle$ is at least one order of magnitude larger than that of FSRQs, the exact value depending considerably on the selection method (see Table 22 and Fig. 17). Since all the sources that are below the radio flux density cut in the RASS and BAT samples are ISP or HSP blazars, their inclusion would increase the difference between the $\nu^{\rm S}_{\rm peak}$ distributions. The distributions of $\nu^{\rm IC}_{\rm peak}$ for FSRQs and BL Lacs also differ, but not as much as those of $\nu^{\rm S}_{\rm peak}$ (see Fig. 18). The majority of the sources in all the samples (both FSRQs and BL Lacs) peak between 10^{21} Hz and 10^{23} Hz, with a few extreme HSP BL Lacs reaching $\sim 10^{26}$ Hz.

8.6. Correlations between fluxes and other blazar parameters

Despite the strict simultaneity of our data, plots of fluxes in different spectral regions (microwave vs. X-ray, microwave vs.

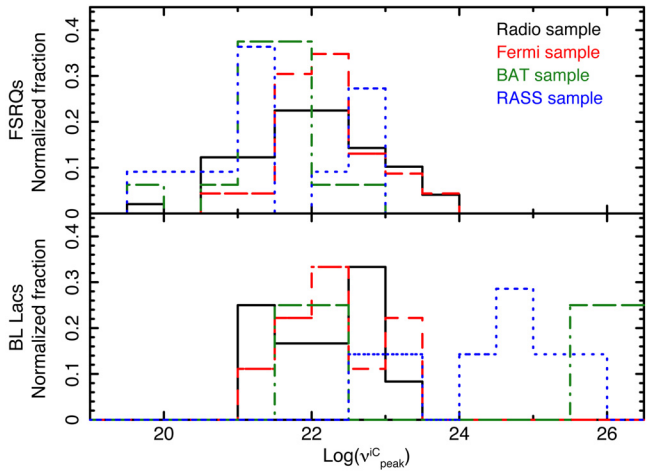

Fig. 18. The rest-frame inverse Compton $\nu_{\rm peak}$ distributions of FSRQs and BL Lacs in different samples. Black solid histograms: radio sample; red dashed histograms: *Fermi*-LAT sample; green dot-dashed histograms: *Swift* BAT sample; blue dotted histograms: RASS sample.

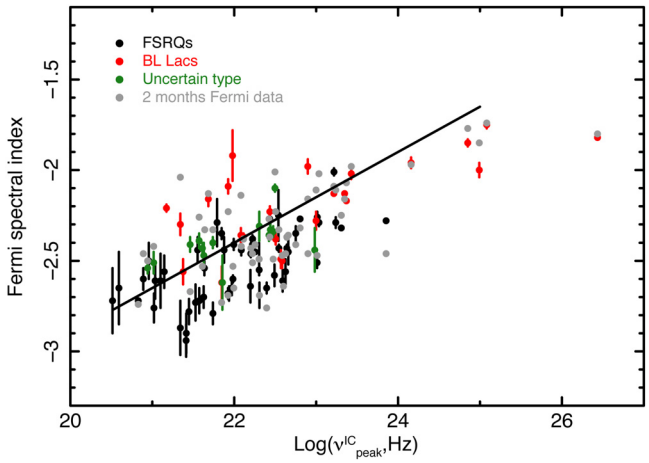

Fig. 19. The γ-ray spectral index, estimated from the entire 27-month *Fermi*-LAT data set of all sources in our samples is plotted against $\log(\nu^{\rm IC}_{\rm peak})$. Gray points, plotted without statistical errors to avoid confusion, represent the *Fermi*-LAT spectral slopes estimated using the 2-month integrations. The solid line is the best-fit given by Abdo et al. (2010a).

γ-ray, and X-ray vs. γ-ray) still have a large scatter (see Figs. 13–15). This is somewhat surprising, as positive correlations between the radio and γ-rays have been reported (e.g. Kovalev et al. 2009; León-Tavares et al. 2010; Giroletti et al. 2010; Ghirlanda et al. 2010; Mahony et al. 2010; Peel et al. 2011; Linford et al. 2011; Ackermann et al. 2011). The difference might be due to the different synchrotron peak energies of the objects in the samples. Even in simple SSC scenarios, this introduces a scatter in the correlation between the fluxes (e.g., for the same radio flux, an object with higher $\nu^{\rm S}_{\rm peak}$ is expected to produce more γ-rays than one with a smaller $\nu^{\rm S}_{\rm peak}$). The large scatter present in Fig. 14 could also imply that γ-ray emission is due to components not always directly related to radiation in other energy bands, e.g., multiple SSC components (see also Abdo et al. 2010a). A good correlation is however present between the X-ray and γ-ray spectral slopes (see Fig. 16).

We confirm the correlations between the *Fermi*-LAT spectral index and the SED peak energies $\nu^{\rm S}_{\rm peak}$ and $\nu^{\rm IC}_{\rm peak}$ found by Abdo et al. (2010a). As an illustration of the agreement, Fig. 19 plots the *Fermi*-LAT spectral slope estimated using the full 27-month data set as a function of $\nu^{\rm IC}_{\rm peak}$. The gray points represent the γ-ray spectral slopes estimated using the quasi-simultaneous two-month dataset. These points, plotted without the much larger error bars to avoid confusion, clearly cluster around the 27-month data, confirming the correlation. The solid line represents the best-fit obtained by Abdo et al. (2010a).

8.7. Comparison with the expectation of simple SSC models

As discussed in Abdo et al. (2010a), simple SSC models predict that in the Thomson regime the peak frequency of the synchrotron ($\nu^{\rm S}_{\rm peak}$) and inverse Compton ($\nu^{\rm IC}_{\rm peak}$) components are related by

$$\frac{\nu^{\rm IC}_{\rm peak}}{\nu^{\rm S}_{\rm peak}} \simeq \frac{4}{3}\left(\gamma^{\rm SSC}_{\rm peak}\right)^2, \quad (3)$$

where $\gamma^{\rm SSC}_{\rm peak}$ is the Lorentz factor of the electrons radiating at the peak energy. This is related to the observed peak frequency of the observed photon spectrum by

$$\gamma^{\rm SSC}_{\rm peak} \propto \left(\frac{\nu^{\rm S}_{\rm peak}}{B\delta}\right)^{1/2}, \quad (4)$$

where $\nu^{\rm S}_{\rm peak}$ is the synchrotron peak frequency in the rest-frame of the emitting region, B is the magnetic field, and δ is the usual Doppler factor (e.g. Urry & Padovani 1995).

In objects where $\nu^{\rm S}_{\rm peak}$ is higher than $\approx 10^{15}$ Hz, the Thomson approximation is no longer valid and the inverse Compton scattering occurs under the Klein-Nishina (KN) regime. Using Monte Carlo simulations, Abdo et al. (2010a) estimated the area covered by SSC models in the plane $\log(\nu^{\rm S}_{\rm peak})$–$\log(\gamma^{\rm SSC}_{\rm peak})$. This area is delimited by the solid contour lines shown in Fig. 20 where we plot the $\log(\gamma^{\rm SSC}_{\rm peak})$ of our sources, calculated from the observed values of $\nu^{\rm S}_{\rm peak}$ and $\nu^{\rm IC}_{\rm peak}$ using Eq. (3), versus the rest-frame $\log(\nu^{\rm S}_{\rm peak})$.

As in the case of the bright γ-ray blazars considered by Abdo et al. (2010a), only a few objects are inside or close to the SSC area, implying that simple SSC models cannot explain the SED of many blazars in our samples. This conclusion is supported by the lack of a strong correlation between radio and γ-ray fluxes.

However, the $\gamma^{\rm SSC}_{\rm peak}$ of blazars that were not detected by *Fermi*-LAT and for which we could only infer a limit to $\nu^{\rm IC}_{\rm peak}$ (from 30% to 40% of the FSRQs in the radio and X-ray selected samples; see Fig. 10 for one example) are plotted as upper limits in Fig. 20; many of these limits are close to or inside the SSC area and therefore the SEDs of these objects are likely consistent with simple SSC emission.

8.8. The Compton dominance of blazars

The Compton dominance (CD, defined as the ratio of the inverse Compton to synchrotron peak luminosities) is a crucial parameter for the study of blazar physics, as it is strictly related to the location of the maximum power output in the energy spectrum of a blazar.

Figure 21 plots the CD values, estimated from our SEDs, as a function of $\nu^{\rm S}_{\rm peak}$, showing that log(CD) ranges from about −0.5

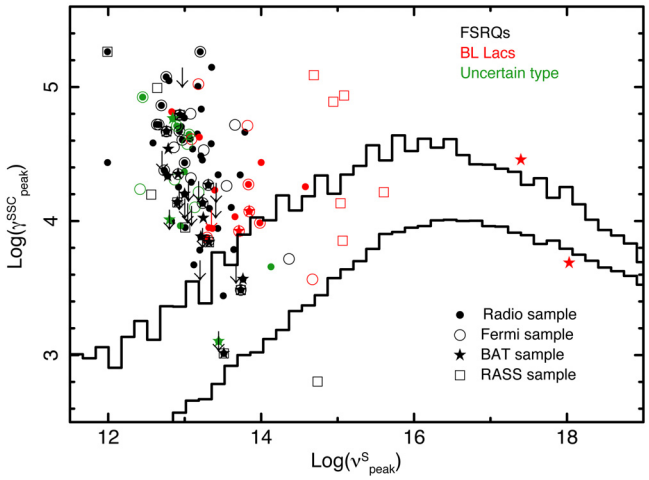

Fig. 20. $\log(\gamma^{SSC}_{peak})$, obtained from Eq. (3) for all the objects in our samples for which we could obtain ν^{S}_{peak} and ν^{IC}_{peak} is plotted against $\log(\nu^{S}_{peak})$ in the rest-frame of the blazars. The two black lines delimit the area predicted by simple homogeneous SSC models obtained through extensive Monte Carlo simulations (see Abdo et al. 2010a, for details).

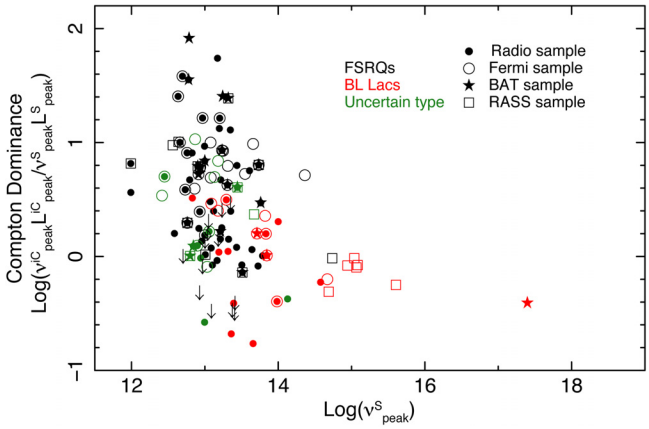

Fig. 21. The logarithm of the Compton dominance is plotted as a function of $\log(\nu^{S}_{peak})$ for all sources for which ν^{S}_{peak} and ν^{IC}_{peak} could be reliably determined.

to about 2. The larger values are always associated with LSP objects, while HSP sources always have values of log(CD) lower than ≈0.5. In this figure, the two blazar subclasses appear to be quite different, with BL Lacs having significantly smaller CD values, even when their ν^{S}_{peak} values are equal to those of FSRQs. To better understand this difference, in Fig. 22 we plot the CD distributions of FSRQs and BL Lacs for different samples and ν^{S}_{peak} intervals.

The FSRQs included in the *Fermi*-LAT sample, which are γ-ray bright by definition, show a CD distribution peaking at large values. We note that in this sample we also applied a radio flux-density limit of 1 Jy, hence the sources below the radio cut must be on average more Compton-dominated than those in our sample. This implies that the distribution of purely γ-ray selected blazars must be even more strongly peaked at high CD values than that of the *Fermi*-LAT sample. Considering instead FSRQs selected in the radio and the X-ray bands, we get quite a different picture, with a broader distribution extending to values of less than 1. Moreover, about 30–45% of FSRQs in the radio, soft X-ray, and hard X-ray selected samples are not detected by *Fermi*-LAT and therefore they must populate the part

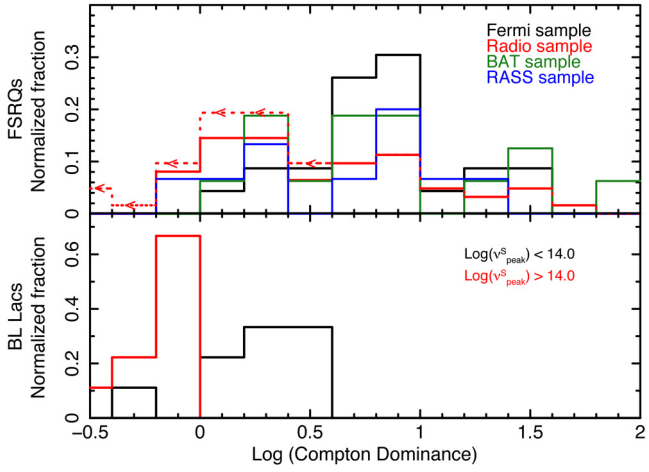

Fig. 22. Distributions of the Compton dominance for FSRQs and BL Lacs of the LSP and HSP type. A significant fraction of FSRQs in the radio, RASS, and BAT samples have not been detected in the γ-ray band and therefore only limits to the Compton dominance (shown as a dashed histogram; only the radio sample to avoid confusion) can be calculated. The large difference between the CD distribution of FSRQs in the *Fermi*-LAT and the other samples illustrates the strong bias that γ-ray selection induces.

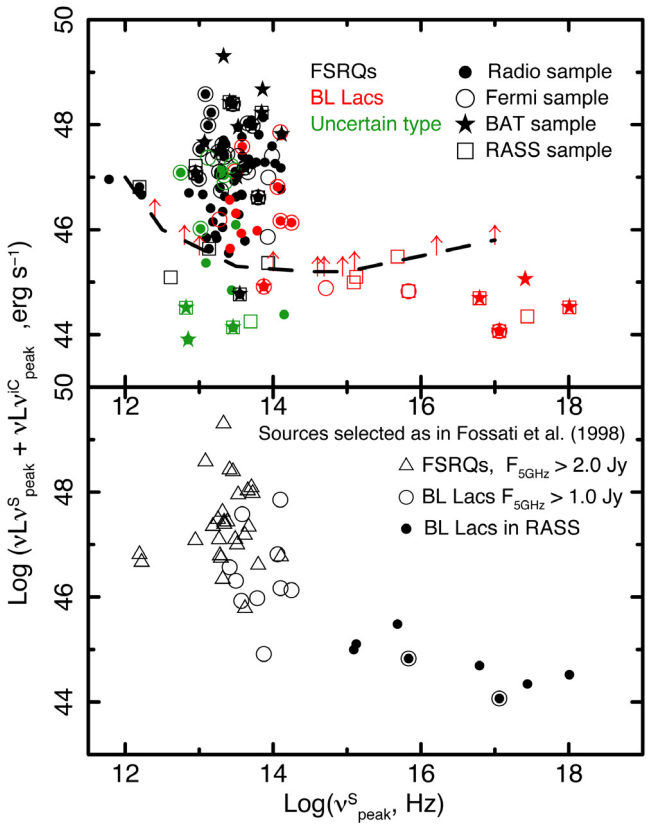

Fig. 23. *Top panel*: the bolometric luminosity (represented by the sum of synchrotron and inverse Compton peak luminosities) is plotted against ν^{S}_{peak}. The non-thermal optical light of blazars with no strong emission lines above the dashed line would be bright enough to swamp the emission from the host galaxy making the source appear featureless thus hampering any redshift measurement. The lower limits, representing BL Lacs with no known redshift, are estimated assuming that the non-thermal light is ten times brighter than that of a giant elliptical host galaxy (see text for details). The *bottom panel* shows the same plot for the subsample of sources satisfying the selection criteria of Fossati et al. (1998).

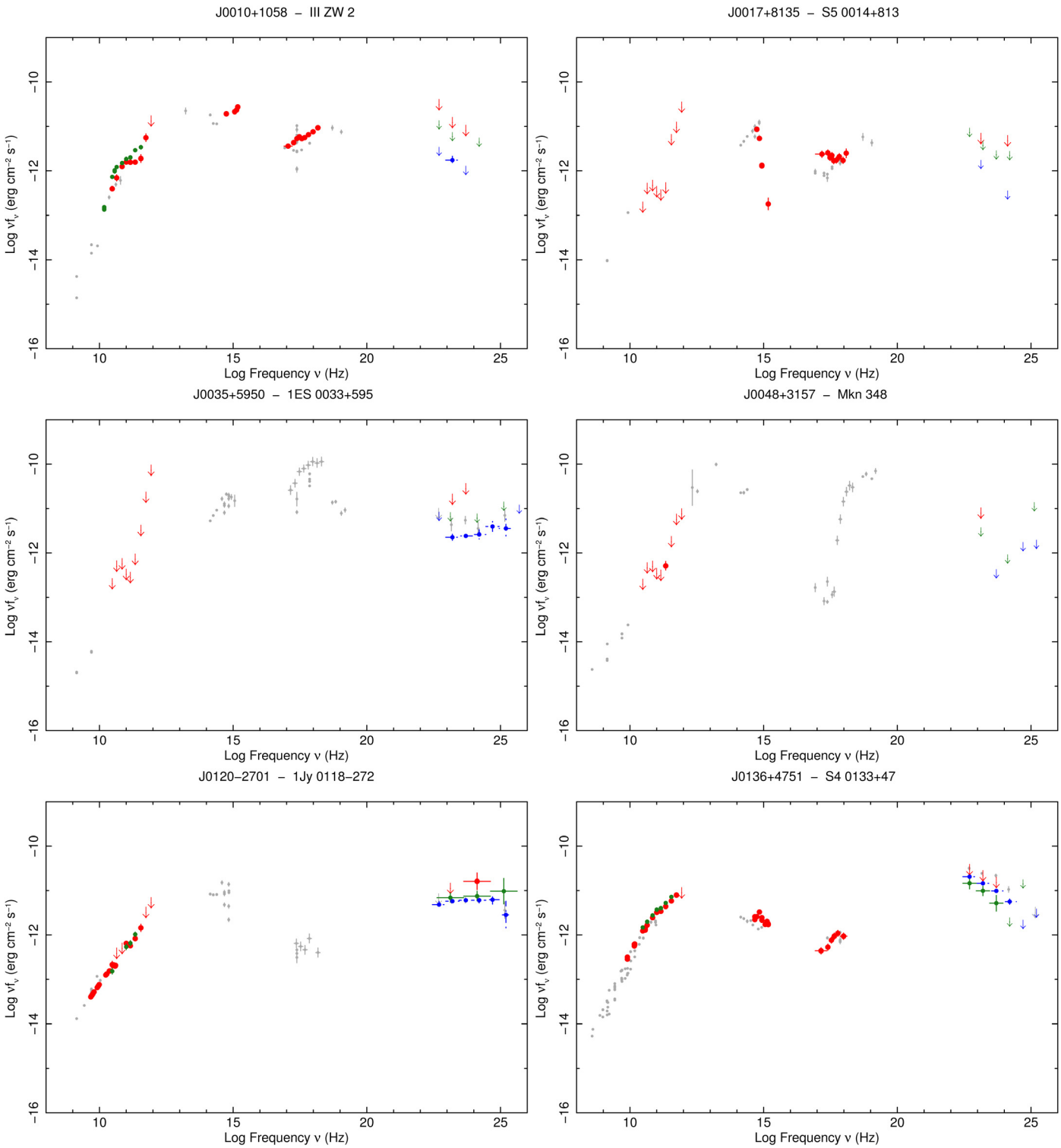

Fig. 24. The SED of III ZW 2 (J0010+1058, *top left*), S5 0014+813 (J0017+8135, *top right*), 1ES 0033+595 (J0035+5950, *middle left*), Mkn 348 (J0048+3157, *middle right*), 1Jy 0118−272 (J0120−2701, *bottom left*), and S4 0133+47 (J0136+4751, *bottom right*). Simultaneous data are shown in red; quasi-simultaneous data, i.e. *Fermi* data integrated over 2 months, *Planck* ERCSC and non-simultaneous ground based observations are shown in green; *Fermi* data integrated over 27 months are shown in blue; literature or archival data are shown in light gray.

of the CD distribution with low CD values. This is shown by the dotted red histogram, which also includes upper limits to the CD estimated as the ratio of the upper limit to $\nu^{\rm IC}_{\rm peak}F(\nu^{\rm IC}_{\rm peak})$ and $\nu^{\rm S}_{\rm peak}F(\nu^{\rm S}_{\rm peak})$ where limits to $\nu^{\rm IC}_{\rm peak}$ and $\nu^{\rm IC}_{\rm peak}F(\nu^{\rm IC}_{\rm peak})$ are obtained by fitting the X-ray data together with the 27-month *Fermi*-LAT upper limits as shown in Fig. 10.

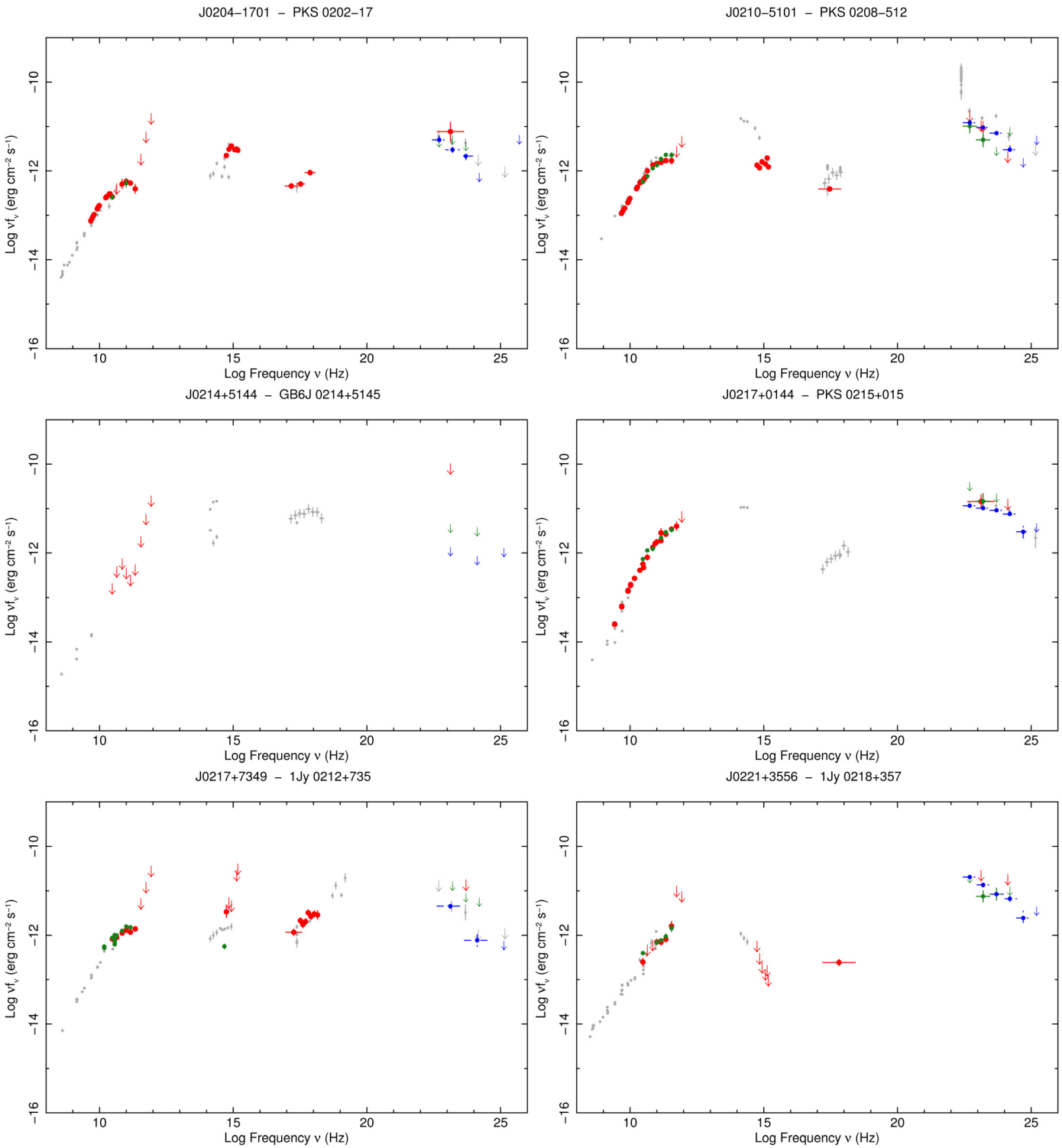

Fig. 25. The SED of PKS 0202−17 (J0204−1701, *top left*), PKS 0208−512 (J0210−5101, *top right*), GB6J 0214+5145 (J0214+5144, *middle left*), PKS 0215+015 (J0217+0144, *middle right*), 1Jy 0212+735 (J0217+7349, *bottom left*), and 1Jy 0218+357 (J0221+3556, *bottom right*). Simultaneous data are shown in red; quasi-simultaneous data, i.e. *Fermi* data integrated over 2 months, *Planck* ERCSC and non-simultaneous ground based observations are shown in green; *Fermi* data integrated over 27 months are shown in blue; literature or archival data are shown in light gray.

8.9. The blazar sequence

The top panel of Fig. 23 plots the logarithm of the bolometric power, represented by the sum of the synchrotron and inverse Compton peak luminosities [$L_{\rm Bol} \sim \nu^{\rm S}_{\rm peak} L(\nu^{\rm S}_{\rm peak}) + \nu^{\rm IC}_{\rm peak} L(\nu^{\rm IC}_{\rm peak})$] as a function of $\log(\nu^{\rm S}_{\rm peak})$ for all sources in the four samples considered in this paper and Planck Collaboration (2011e) for which an estimate of $\nu^{\rm S}_{\rm peak}$ and the bolometric luminosity was possible. We use this plot to test the relationship known as the *Blazar Sequence*, which is the strong anti-correlation between bolometric luminosity and $\nu^{\rm S}_{\rm peak}$ claimed by Fossati et al. (1998) and Ghisellini et al. (1998) that remains a subject of lively debate

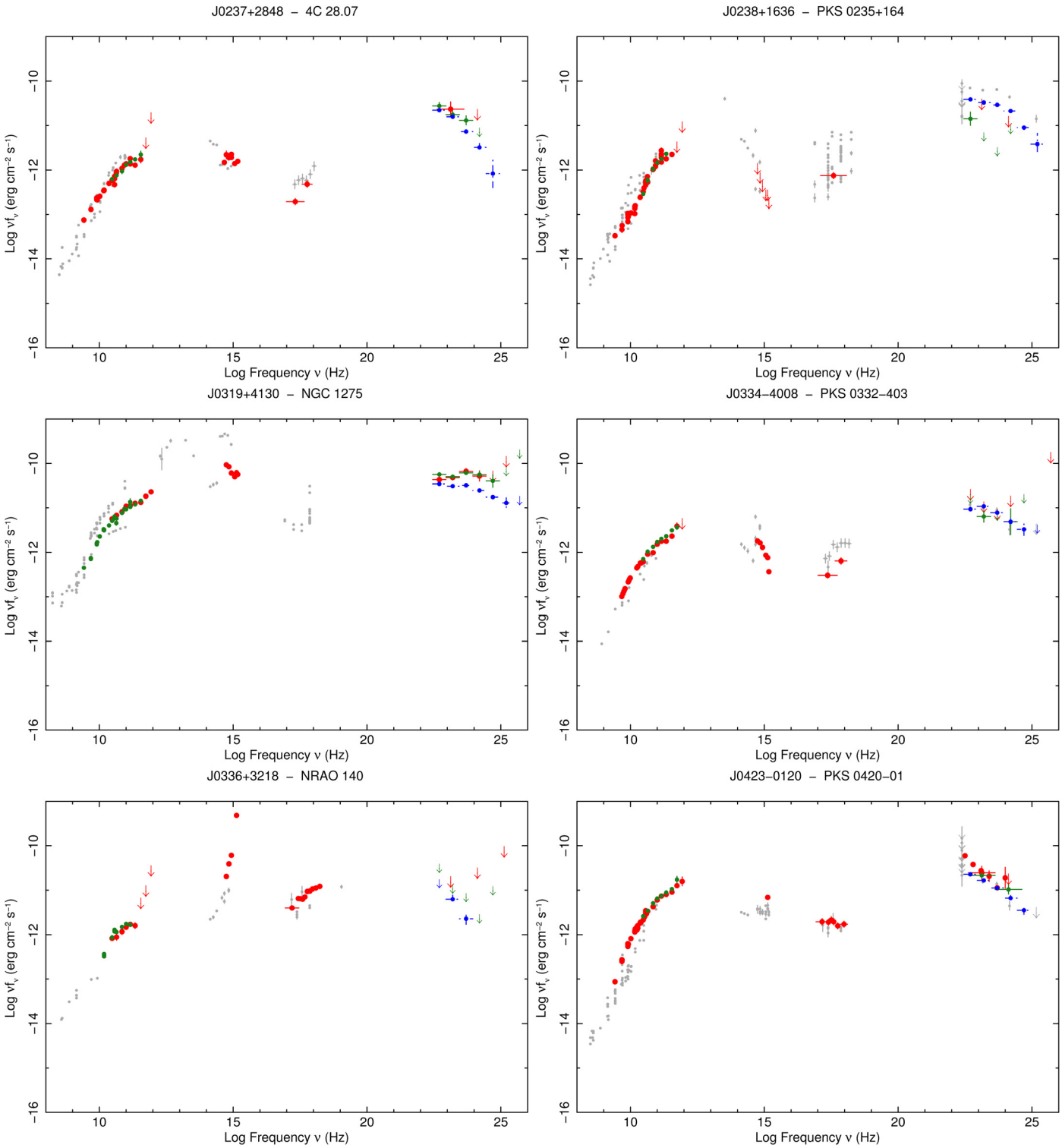

Fig. 26. The SED of 4C 28.07 (J0237+2848, *top left*), PKS 0235+164 (J0238+1636, *top right*), NGC 1275 (J0319+4130, *middle left*), PKS 0332−403 (J0334−4008, *middle right*), NRAO 140 (J0336+3218, *bottom left*) and PKS 0420−01 (J0423−0120, *bottom right*). Simultaneous data are shown in red; quasi-simultaneous data, i.e. *Fermi* data integrated over 2 months, *Planck* ERCSC and non-simultaneous ground based observations are shown in green; *Fermi* data integrated over 27 months are shown in blue; literature or archival data are shown in light gray.

(e.g., Giommi et al. 1999; Padovani et al. 2003; Caccianiga & Marchã 2004; Nieppola et al. 2006; Padovani 2007; Ghisellini & Tavecchio 2008).

We stress that to robustly test for the existence of such a relationship it is mandatory to use samples that are *unbiased*, that is selected in such a way that no particular part of the $L_{\rm Bol}$–$\nu^{\rm S}_{\rm peak}$ diagram is more likely than others to be selected. Although our samples are statistically well-defined, they are not unbiased from this viewpoint for the following reasons:

a) as shown in Figs. 17 and 18, the distribution of $\nu^{\rm S}_{\rm peak}$ strongly depends on the selection method; hence, for the various samples, we obtain different samplings of the parameter $\nu^{\rm S}_{\rm peak}$;

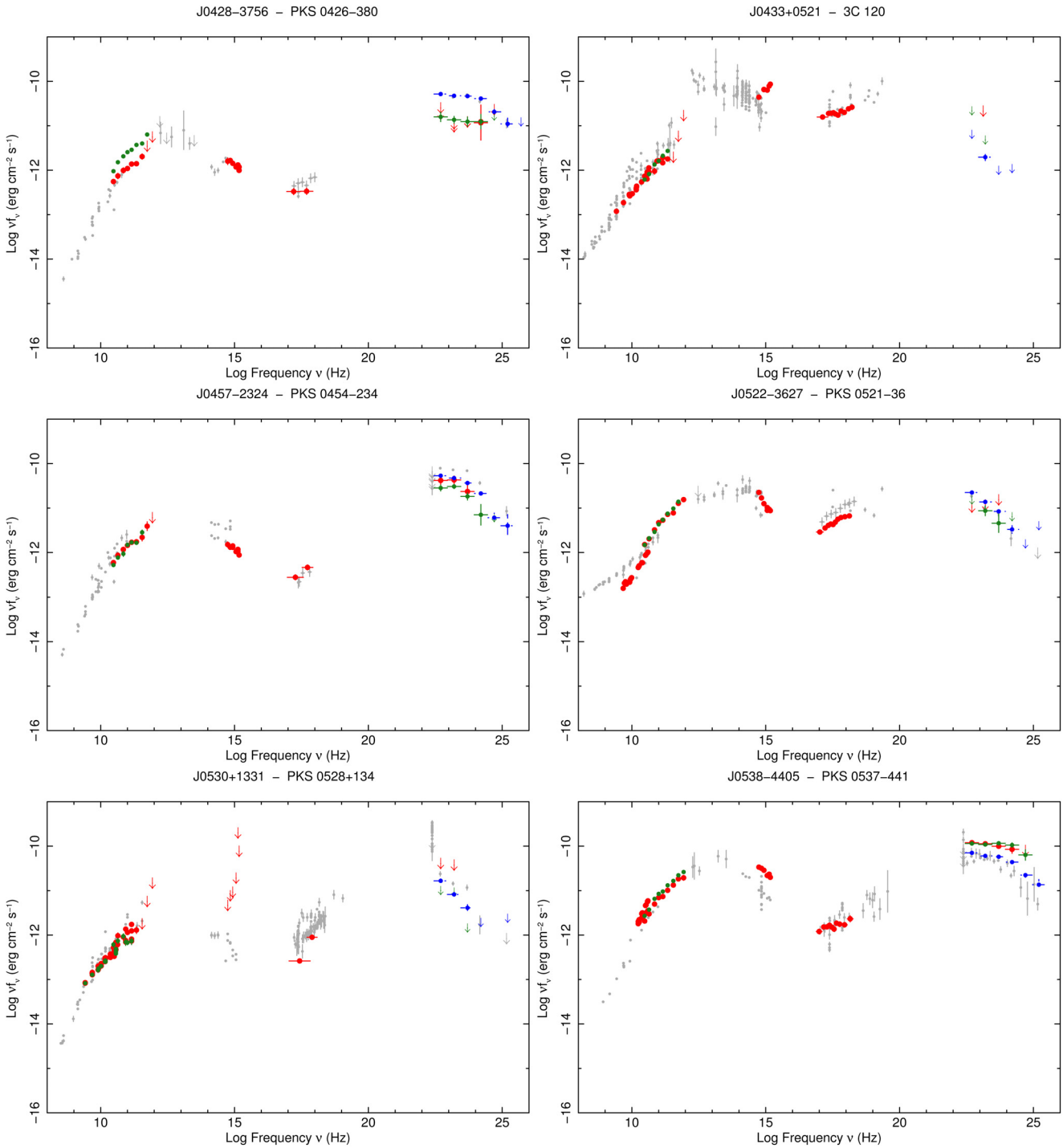

Fig. 27. The SED of PKS 0426−380 (J0428−3756, *top left*), 3C 120 (J0433+0521, *top right*), PKS 0454−234 (J0457−2324, *middle left*), PKS 0521−36 (J0522−3627, *middle right*), PKS 0528+134 (J0530+1331, *bottom left*), and PKS 0537−441 (J0538−4405, *bottom right*). Simultaneous data are shown in red; quasi-simultaneous data, i.e. *Fermi* data integrated over 2 months, *Planck* ERCSC and non-simultaneous ground based observations are shown in green; *Fermi* data integrated over 27 months are shown in blue; literature or archival data are shown in light gray.

b) the area above the dashed line, which represents the luminosity above which the non-thermal emission of a blazar completely dominates the observed optical flux[12], cannot be populated by blazars with no emission lines, such as BL Lacs, as in this case they would appear completely featureless and therefore their redshift could not be measured. In this respect, we note that over 40% of the BL Lacs in the BZCAT catalog, and an even larger fraction of the *Fermi*-LAT detected BL Lacs, still lack any redshift measurement (Massaro et al. 2010; Shaw et al. 2009, 2010). All the BL Lacs in our samples for which redshifts are unknown

[12] We assume a non-thermal luminosity one order of magnitude higher than that of the host giant-elliptical galaxy of luminosity equal to that found by Scarpa et al. (2000) and Urry et al. (2000) and verified by us to fit our SEDs.

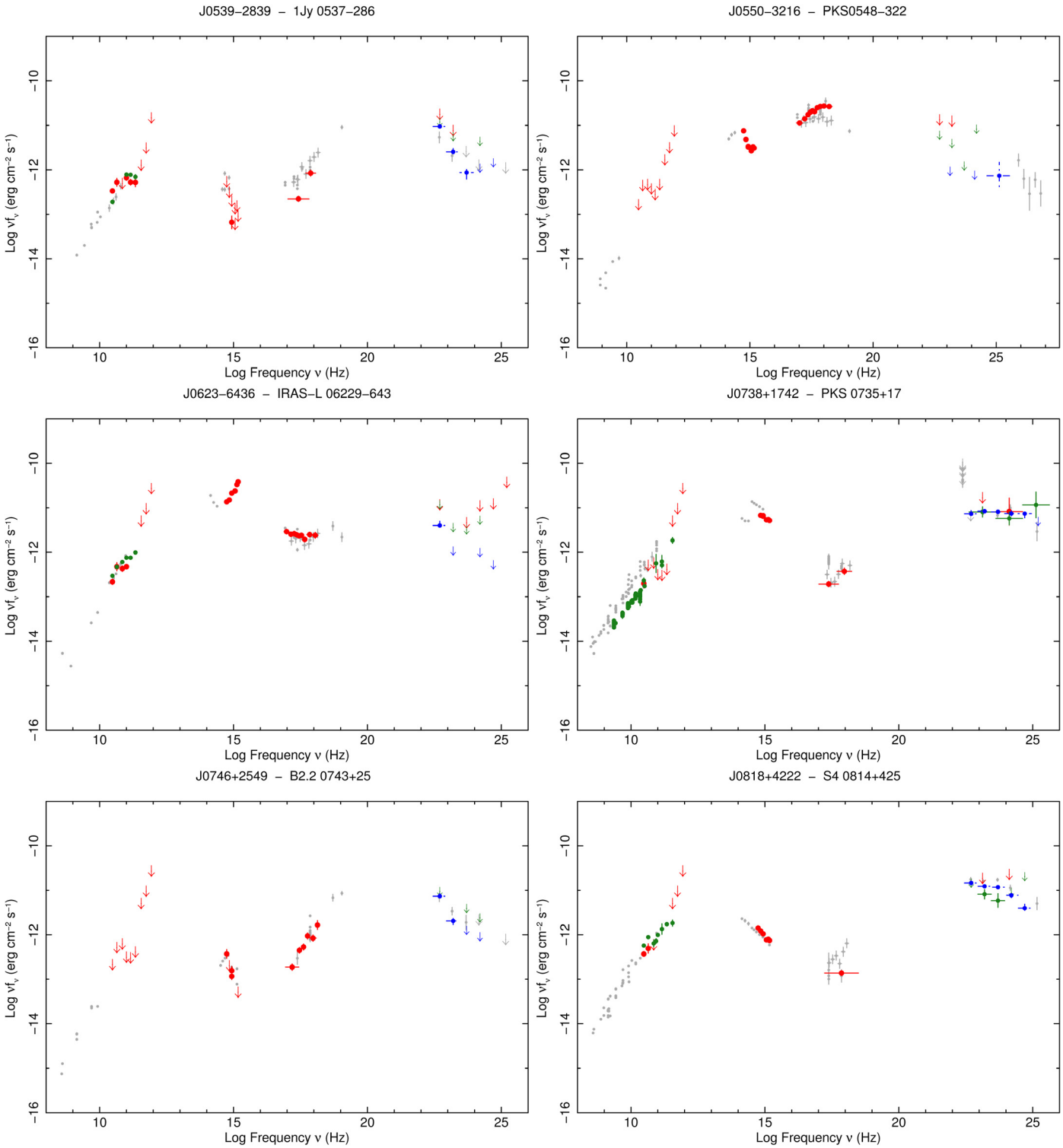

Fig. 28. The SED of 1Jy 0537−286 (J0539−2839, *top left*), PKS 0548−322 (J0550−3216, *top right*), IRAS-L 06229−643 (J0623−6436, *middle left*), PKS 0735+17 (J0738+1742, *middle right*), B2.2 0743+25 (J0746+2549, *bottom left*), and S4 0814+425 (J0818+4222, *bottom right*). Simultaneous data are shown in red; quasi-simultaneous data, i.e. *Fermi* data integrated over 2 months, *Planck* ERCSC and non-simultaneous ground based observations are shown in green; *Fermi* data integrated over 27 months are shown in blue; literature or archival data are shown in light gray.

are plotted in Fig. 23 as lower limits estimated assuming that their non-thermal light is ten times brighter than the optical light of the host galaxy. Some BL Lacs of known luminosity (red points in Fig. 23) are above the red line because their redshift was measured from emission lines with rest-frame equivalent widths below the 5 Å limit; they might be objects with properties in-between those of BL Lacs and FSRQs (see. e.g., Ghisellini et al. 2011);

c) the different radio flux-density cuts applied to our samples imply that different subsamples probe different parts of the

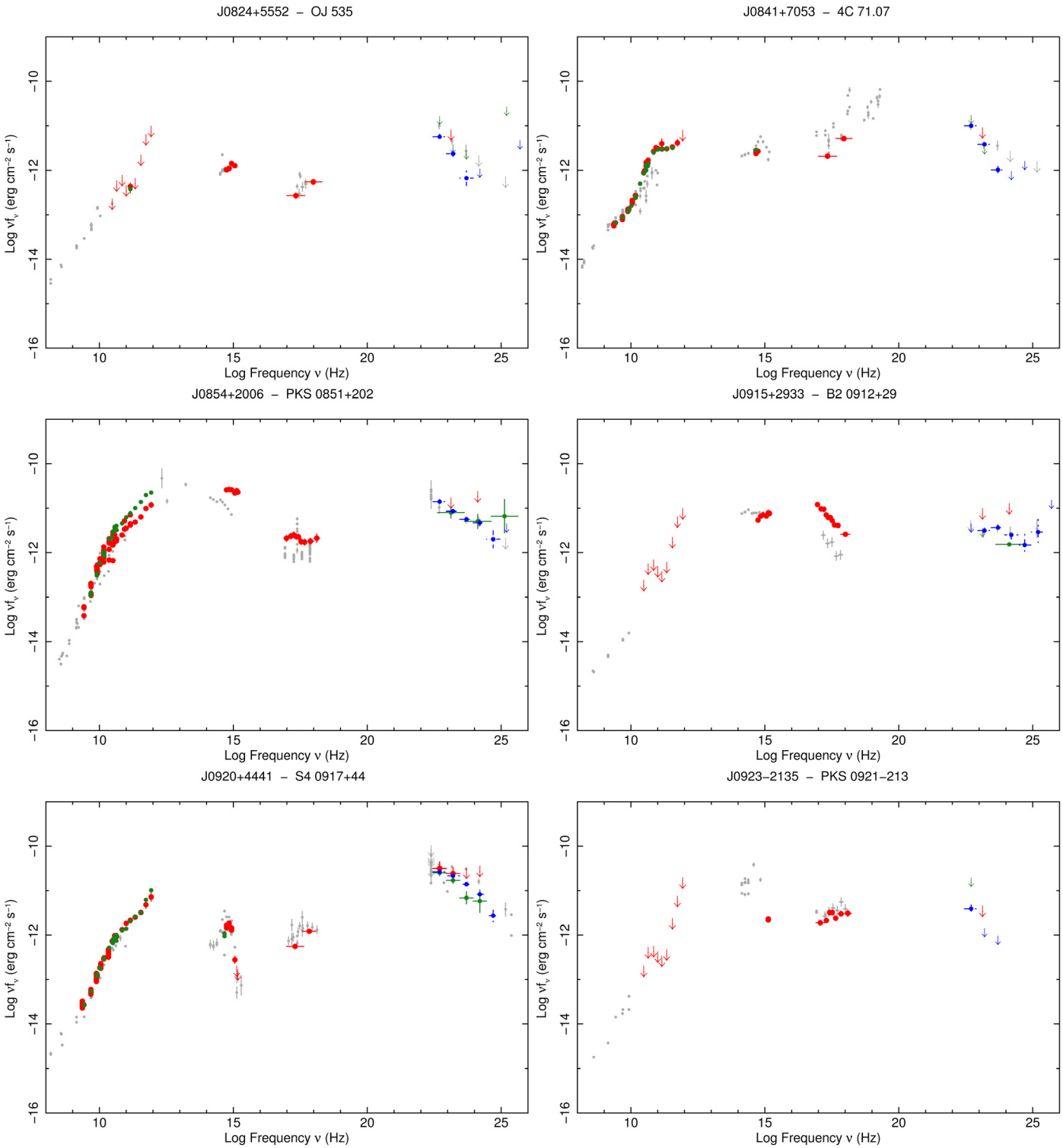

Fig. 29. The SED of OJ 535 (J0824+5552, *top left*), 4C 71.07 (J0841+7053, *top right*), PKS 0851+202 (J0854+2006, *middle left*), B2 0912+29 (J0915+2933, *middle right*), S4 0917+44 (J0920+4441, *bottom left*), and PKS 0921−213 (J0923−2135, *bottom right*). Simultaneous data are shown in red; quasi-simultaneous data, i.e. *Fermi* data integrated over 2 months, *Planck* ERCSC and non-simultaneous ground based observations are shown in green; *Fermi* data integrated over 27 months are shown in blue; literature or archival data are shown in light gray.

radio luminosity function. The radio and γ-ray selected samples, which are defined using a high radio flux limit ($S \geq 1$ Jy), probe the high-luminosity end of the radio luminosity function, which, for $\nu^{S}_{peak} = 10^{13}$ Hz and the observed redshift and CD distributions, translates into $L_{Bol} \gtrsim 10^{46}$ erg s^{-1}. The soft and hard X-ray selected samples have a radio flux density cut of $S = 0.1$–0.2 Jy, or about one order of magnitude fainter than that of the radio and *Fermi*-LAT samples, hence might include significantly less powerful sources, as faint as bolometric luminosities of the order of 10^{44} erg s^{-1}.

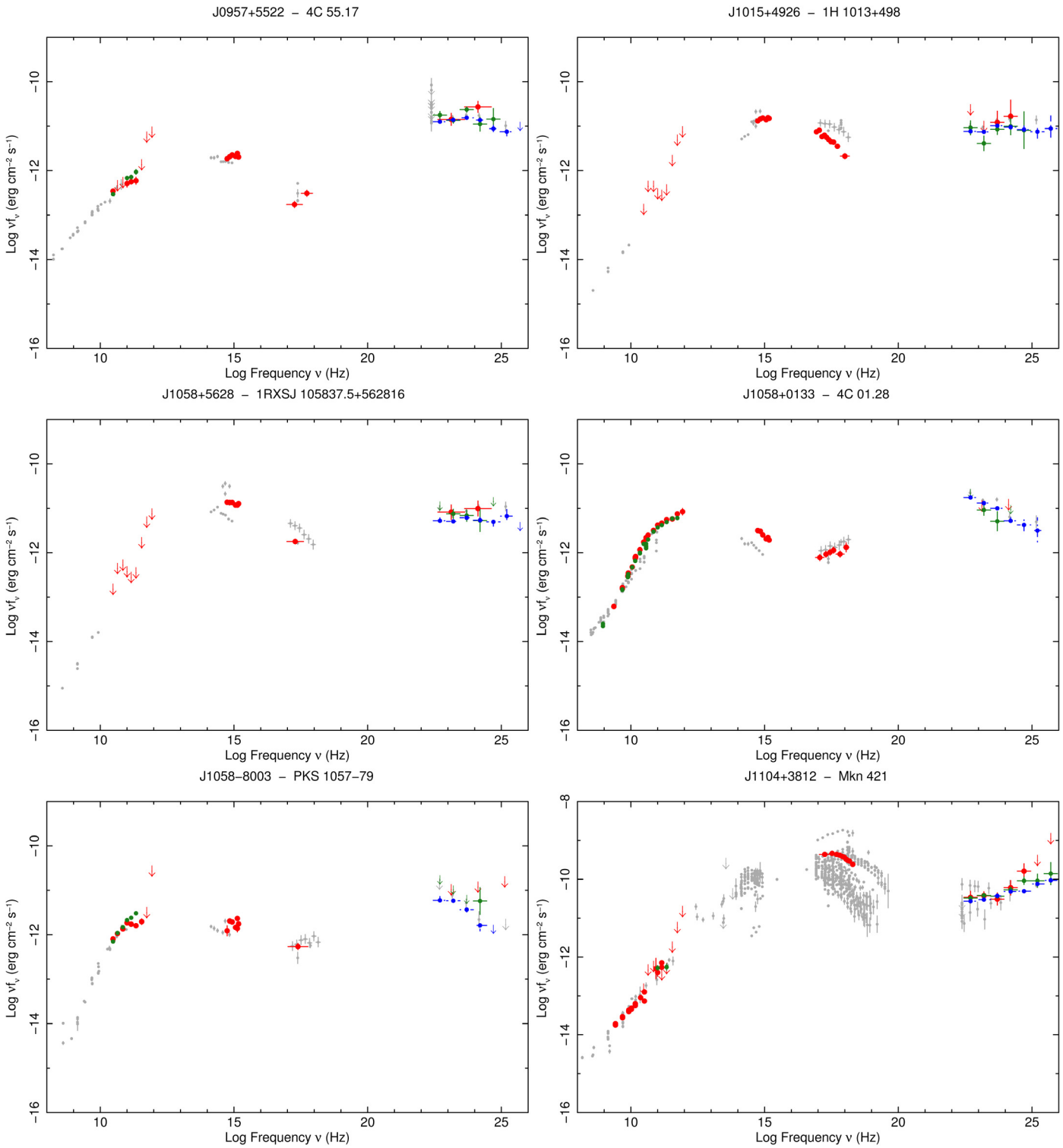

Fig. 30. The SED of 4C 55.17 (J0957+5522, *top left*), 1H 1013+498 (J1015+4926, *top right*), 1RXSJ 105837.5+562816 (J1058+5628, *middle left*), 4C 01.28 (J1058+0133, *middle right*), PKS 1057−79 (J1058−8003, *bottom left*), and Mkn 421 (J1104+3812, *bottom right*). Simultaneous data are shown in red; quasi-simultaneous data, i.e. *Fermi* data integrated over 2 months, *Planck* ERCSC and non-simultaneous ground based observations are shown in green; *Fermi* data integrated over 27 months are shown in blue; literature or archival data are shown in light gray.

If we remove the ν^{S}_{peak} dependence of the selection method by considering only FSRQs (which have the same ν^{S}_{peak} distributions as all samples), we see that the luminosity values span five orders of magnitude from $\sim 10^{44}$ to $\sim 10^{49}$ erg s^{-1} and show no trend with ν^{S}_{peak}, which only ranges between $\sim 10^{12.5}$ and $\sim 10^{14}$ Hz. No obvious correlation is present in each sample separately or in the union of the four samples. The L-shaped distribution that is apparent in Fig. 23, if lower limits are ignored, is

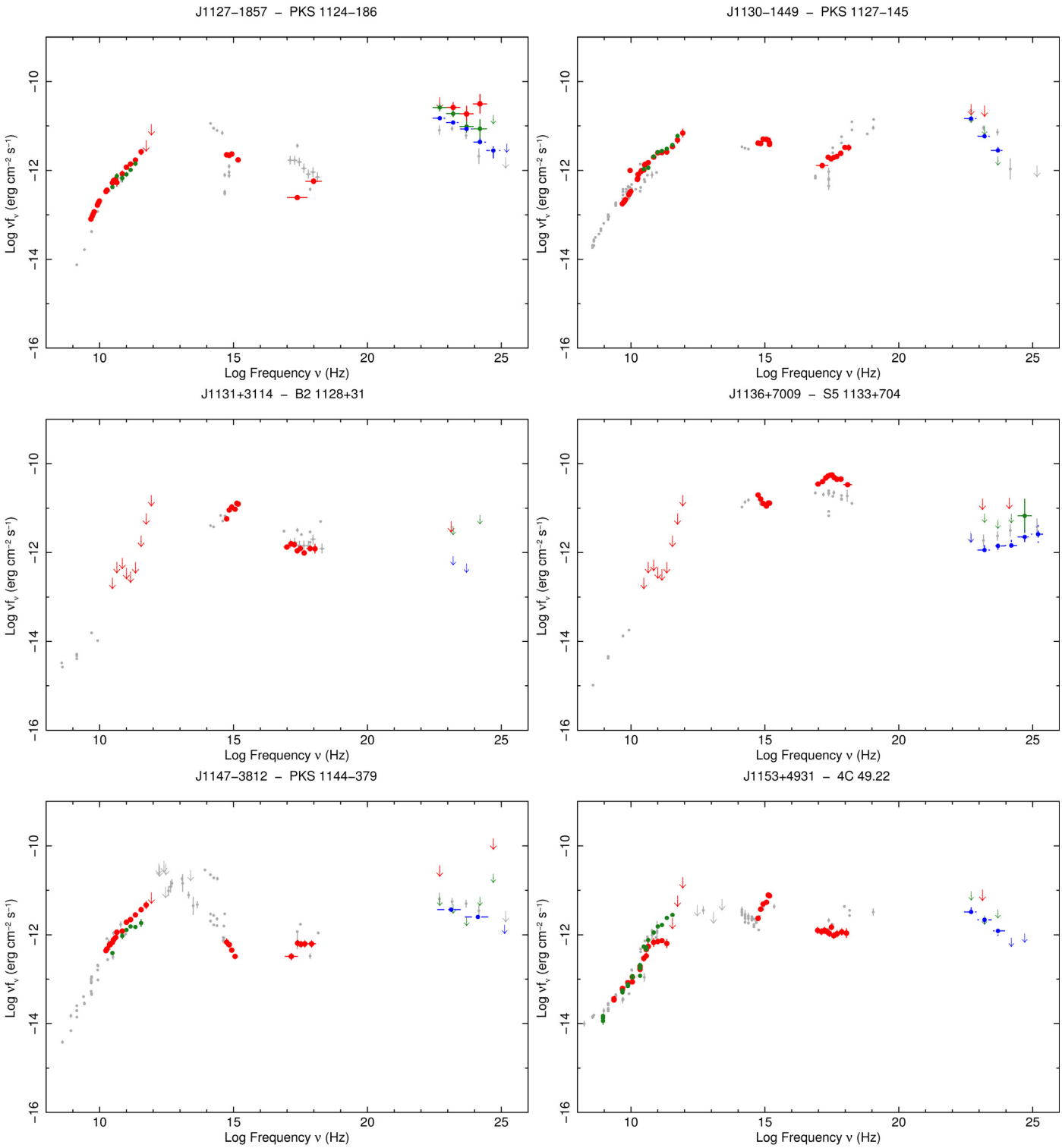

Fig. 31. The SED of PKS 1124−186 (J1127−1857, *top left*), PKS 1127−145 (J1130−1449, *top right*), B2 1128+31 (J1131+3114, *middle left*), S5 1133+704 (J1136+7009, *middle right*), PKS 1144−379 (J1147−3812, *bottom left*), and 4C 49.22 (J1153+4931, *bottom right*). Simultaneous data are shown in red; quasi-simultaneous data, i.e. *Fermi* data integrated over 2 months, *Planck* ERCSC and non-simultaneous ground based observations are shown in green; *Fermi* data integrated over 27 months are shown in blue; literature or archival data are shown in light gray.

similar to that found by Meyer et al. (2011) who estimated both the $\nu^{\rm S}_{\rm peak}$ and peak luminosities of a large sample of blazars using *non-simultaneous* multi-frequency data. These authors, however, instead of considering lower limits to the peak luminosities of blazars with unknown redshifts, assumed a luminosity corresponding to the redshift that the host galaxy would have for the observed blazar optical magnitude. Meyer et al. (2011) argued that the strong correlation predicted by the blazar sequence turns into a *blazar envelope* when partly misaligned blazars are included in the samples. However, Giommi et al. (2012), by

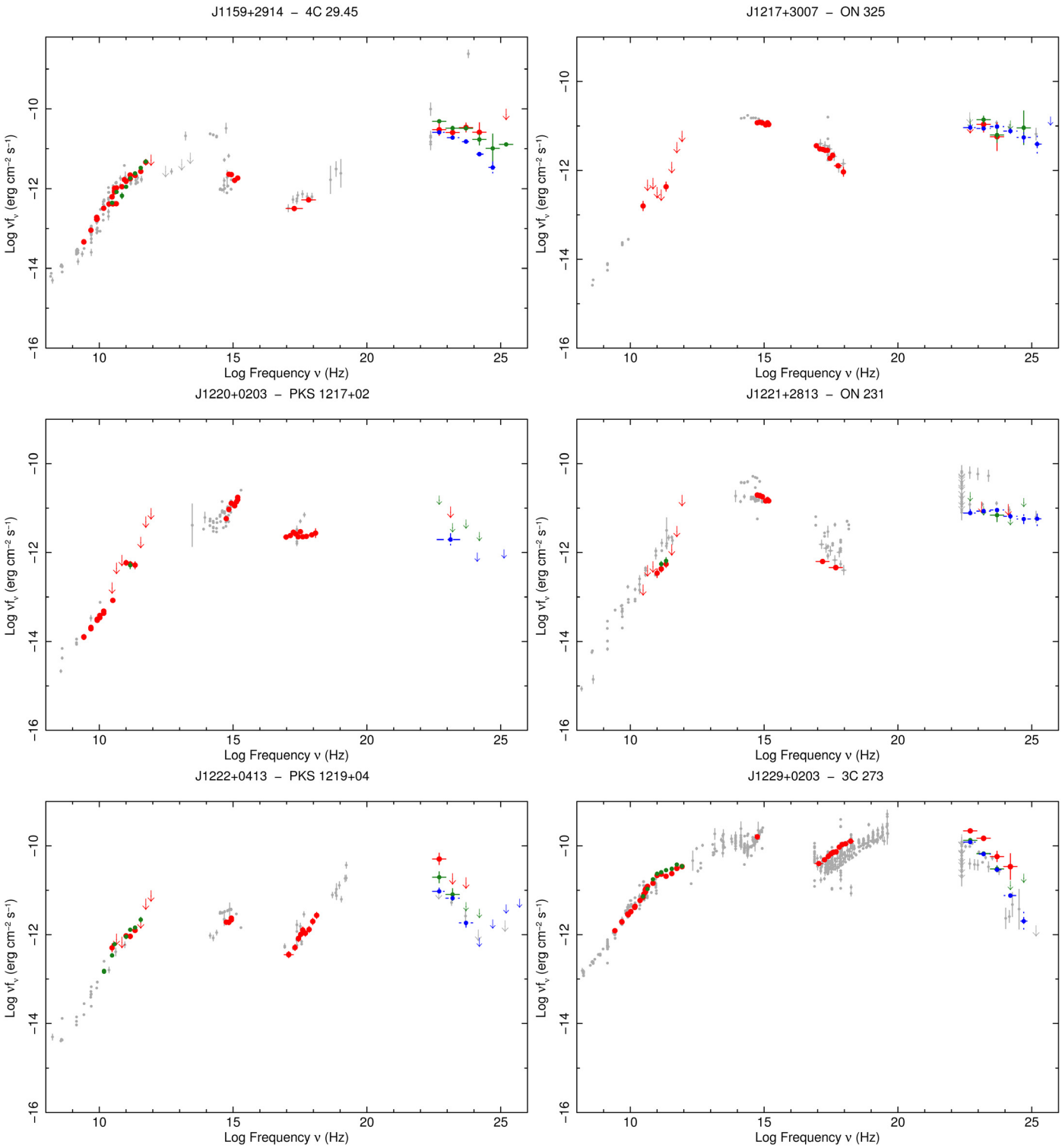

Fig. 32. The SED of 4C 29.45 (J1159+2914, *top left*), ON 325 (J1217+3007, *top right*), PKS 1217+02 (J1220+0203, *middle left*), ON 231 (J1221+2813, *middle right*), PKS 1219+04 (J1222+0413, *bottom left*), and 3C 273 (J1229+0203, *bottom right*). Simultaneous data are shown in red; quasi-simultaneous data, i.e. *Fermi* data integrated over 2 months, *Planck* ERCSC and non-simultaneous ground based observations are shown in green; *Fermi* data integrated over 27 months are shown in blue; literature or archival data are shown in light gray.

means of detailed Monte Carlo simulations, showed that this envelope, or L-shaped distribution, is expected when blazars with no redshift measurements are not properly taken into account.

Finally, we consider the subsample of sources that satisfy the *same conditions* as in Fossati et al. (1998), that is $S_{5\,\mathrm{GHz}} > 2$ Jy for FSRQs, $S_{5\,\mathrm{GHz}} > 1$ Jy for radio-selected BL Lacs, no restrictions for X-ray selected BL Lacs, and the exclusion of all BL Lacs with no redshift information. This case is illustrated in Fig. 23 (bottom panel), which shows a trend very similar to that presented in Fossati et al. (1998).

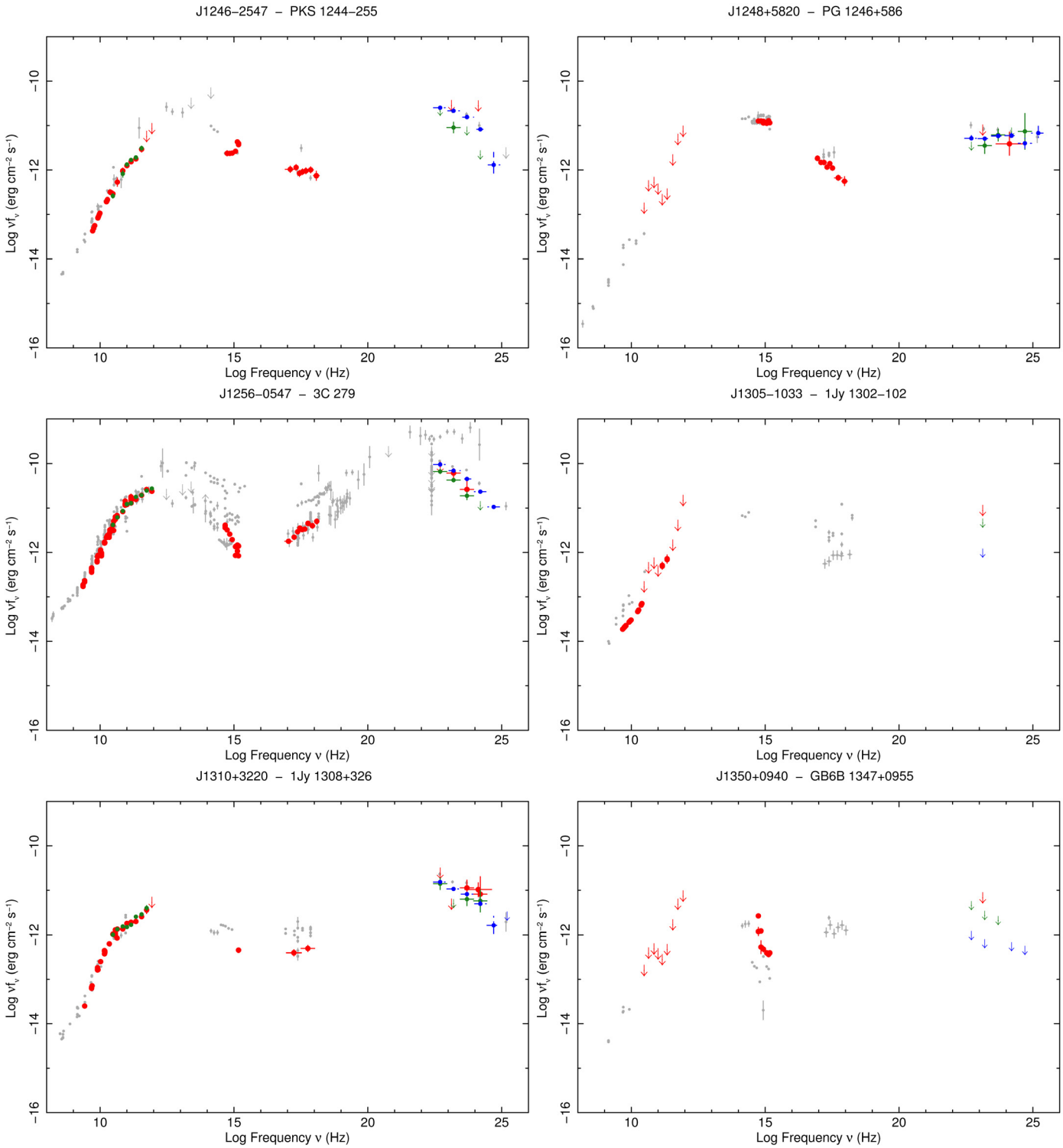

Fig. 33. The SED of PKS 1244−255 (J1246−2547, *top left*), PG 1246+586 (J1248+5820, *top right*). 3C 279 (J1256−0547, *middle left*), 1Jy 1302−102 (J1305−1033, *middle right*), 1Jy 1308+326 (J1310+3220, *bottom left*), and GB6B 1347+0955 (J1350+0940, *bottom right*). Simultaneous data are shown in red; quasi-simultaneous data, i.e. *Fermi* data integrated over 2 months, *Planck* ERCSC and non-simultaneous ground based observations are shown in green; *Fermi* data integrated over 27 months are shown in blue; literature or archival data are shown in light gray.

Taking into account all of the above, we conclude that our data do not show a correlation of the type predicted by Fossati et al. (1998), owing to the presence of low luminosity LSP objects and the difficulty in measuring the redshifts of likely high-luminosity HSP sources. That such a correlation becomes evident when the objects are selected by the criteria of Fossati et al. (1998) supports the hypothesis that the correlation might be the result of a selection effect.

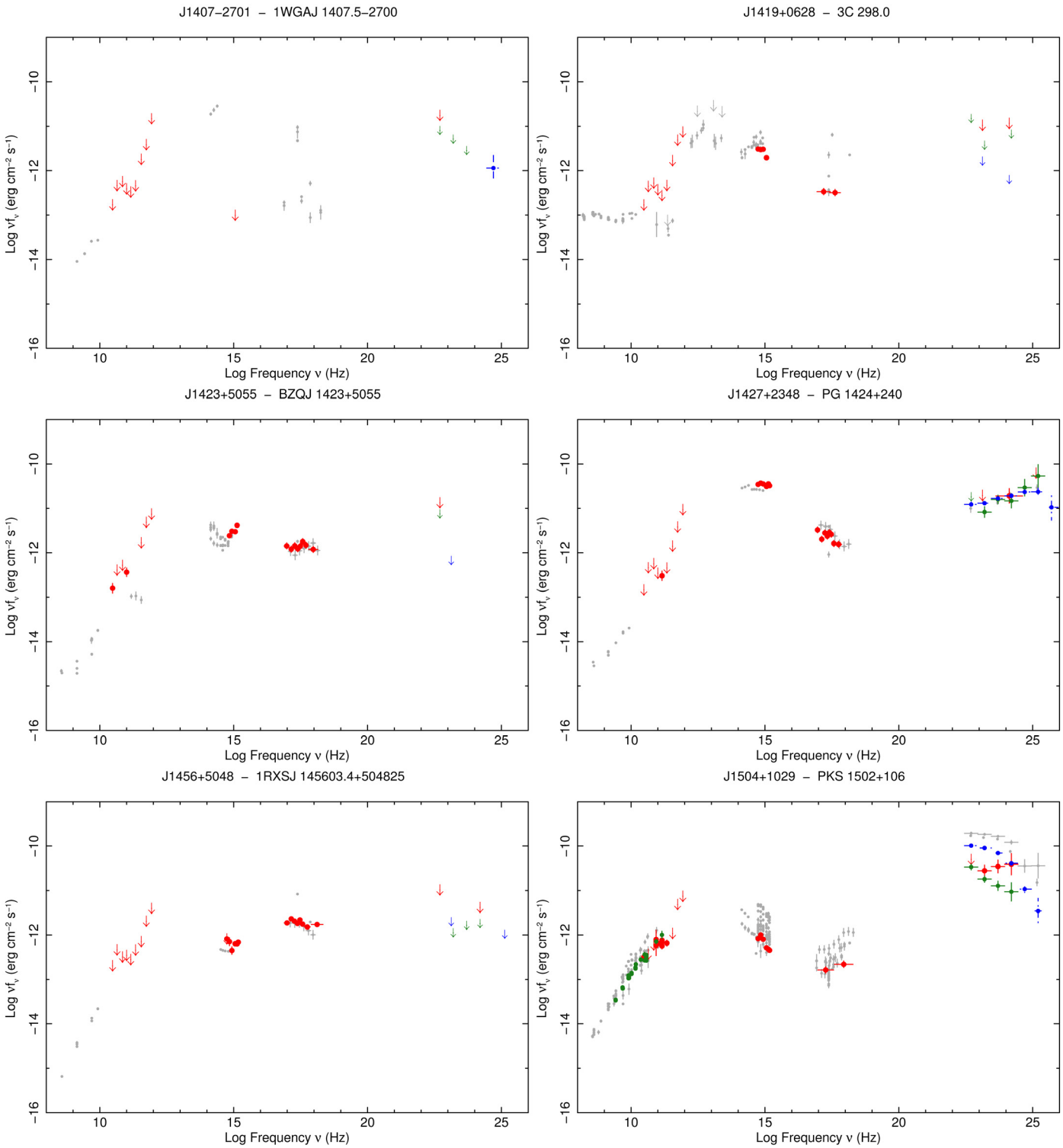

Fig. 34. The SED of 1WGAJ 1407.5−2700 (J1407−2701, *top left*) and of 3C 298.0 (J1419+0628, *top right*), CSO 643 (J1423+5055, *middle left*), of PG 1424+240 (J1427+2348, *middle right*), 1RXSJ 145603.4+504825 (J1456+5048, *bottom left*), and PKS 1502+106 (J1504+1029, *bottom right*). Simultaneous data are shown in red; quasi-simultaneous data, i.e. *Fermi* data integrated over 2 months, *Planck* ERCSC and non-simultaneous ground based observations are shown in green; *Fermi* data integrated over 27 months are shown in blue; literature or archival data are shown in light gray.

8.10. Selection effects and sample composition

Our decision to select flux-limited samples for widely different parts of the electromagnetic spectrum (radio, soft X-ray, hard X-ray, and γ-ray) has allowed us to demonstrate the strong selection biases that can affect important physical parameters, such as the peak energy of both the synchrotron and inverse Compton components (see Figs. 17 and 18) and the Compton dominance (see Fig. 22). Since FSRQs and BL Lacs have significantly different ν^{S}_{peak} distributions, these selection biases also

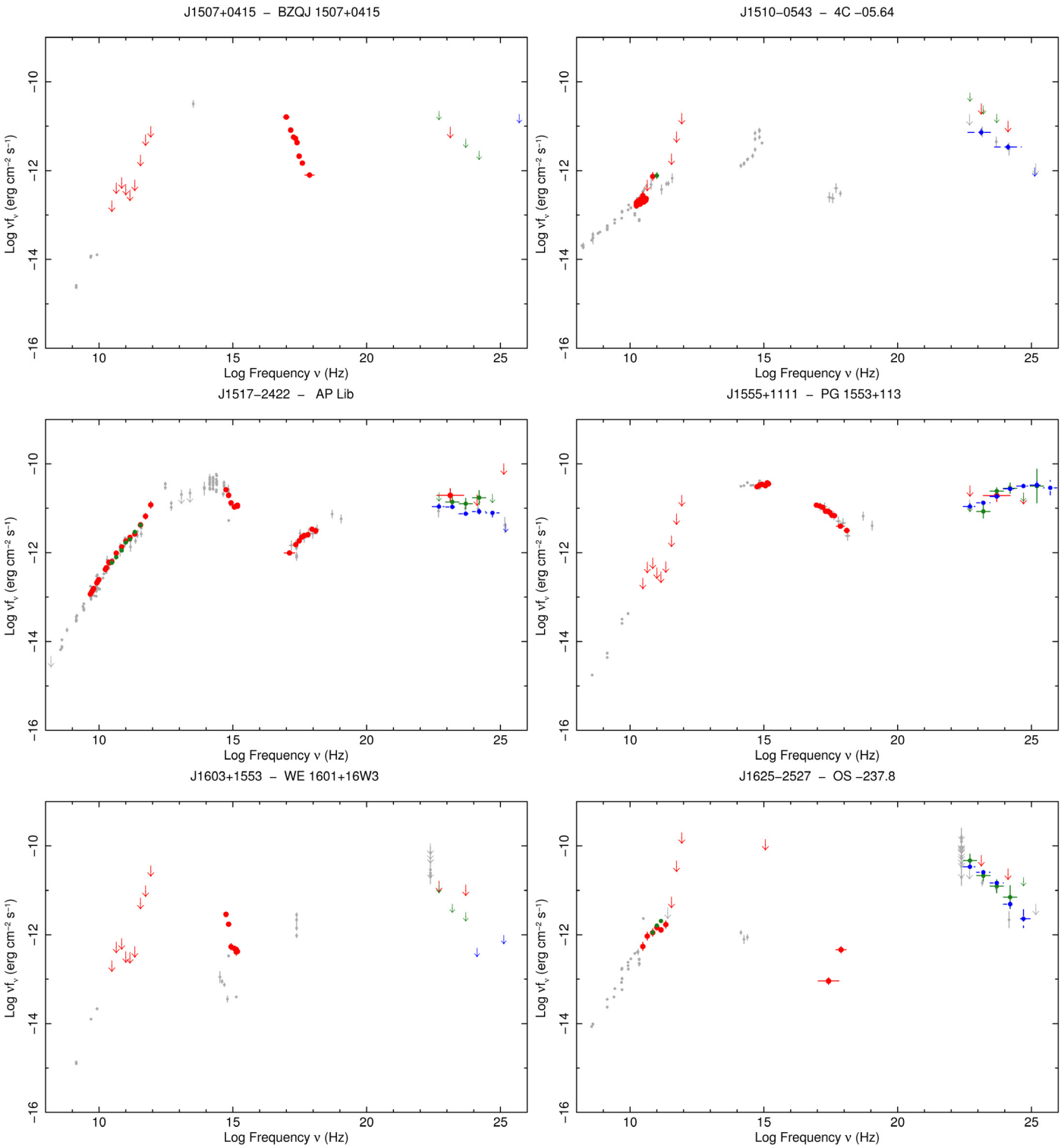

Fig. 35. The SED of BZQJ 1507+0415 (J1507+0415, *top left*), 4C −05.64 (J1510−0543, *top right*), AP Lib (J1517−2422, *middle left*), PG 1553+113 (J1555+1111, *middle right*), WE 1601+16W3 (J1603+1553, *bottom left*), and OS −237.8 (J1625−2527, *bottom right*). Simultaneous data are shown in red; quasi-simultaneous data, i.e. *Fermi* data integrated over 2 months, *Planck* ERCSC and non-simultaneous ground based observations are shown in green; *Fermi* data integrated over 27 months are shown in blue; literature or archival data are shown in light gray.

strongly affect the composition of the samples in terms of the relative abundances of blazar subclasses (FSRQs vs. BL Lacs, LSPs vs. HSPs), as is apparent from Table 4.

Radio-selected samples include sources that are bright in the radio band. If there is no correlation between radio flux/luminosity and other parameters such as $\nu^S_{\rm peak}$ and Compton

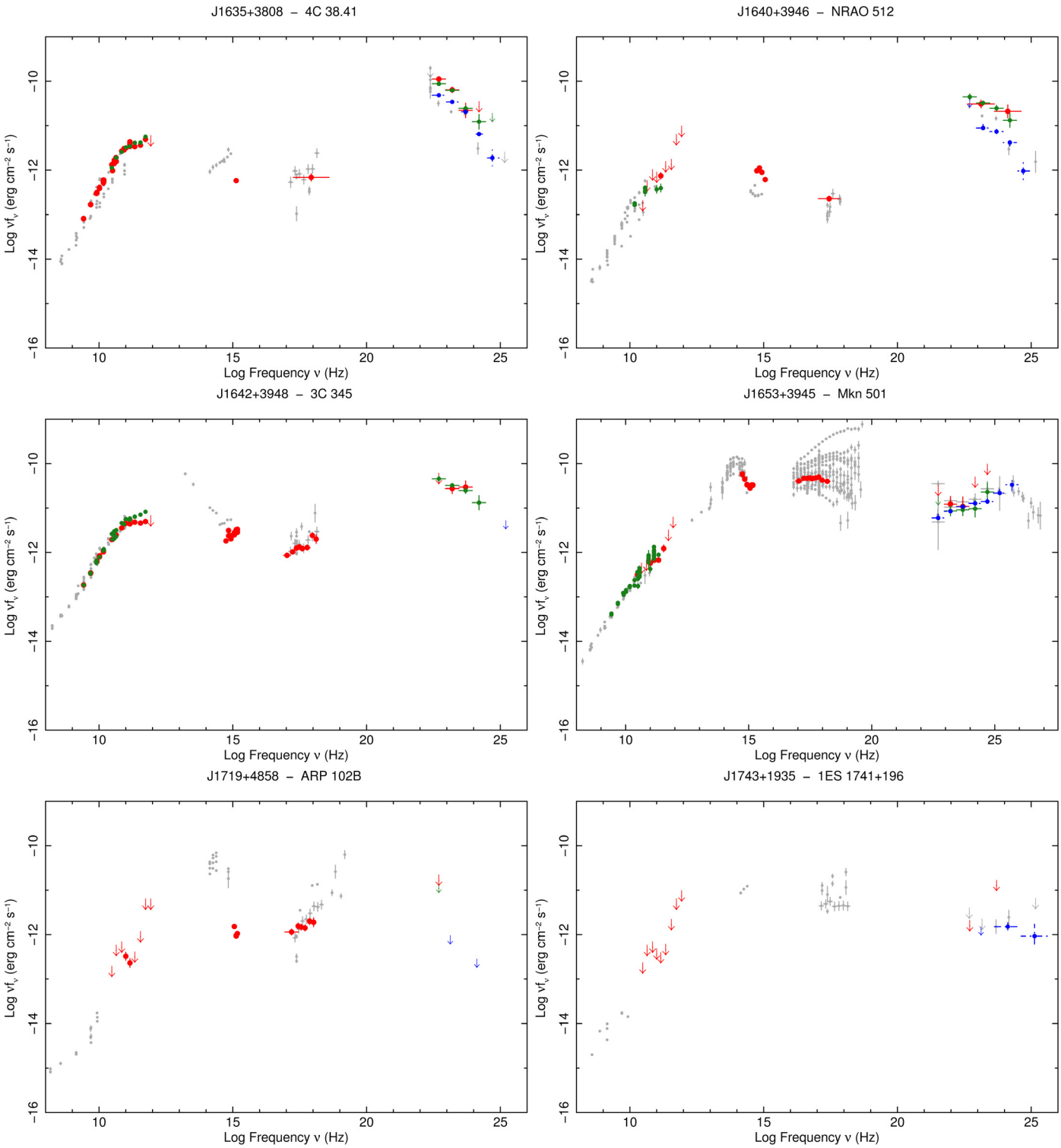

Fig. 36. The SED of 4C 38.41 (J1635+3808, *top left*), NRAO 512 (J1640+3946, *top right*), 3C 345 (J1642+3948, *middle left*), Mkn 501 (J1653+3945, *middle right*), ARP 102B (J1719+4858, *bottom left*), and 1ES 1741+196 (J1743+1935, *bottom right*). Simultaneous data are shown in red; quasi-simultaneous data, i.e. *Fermi* data integrated over 2 months, *Planck* ERCSC and non-simultaneous ground based observations are shown in green; *Fermi* data integrated over 27 months are shown in blue; literature or archival data are shown in light gray.

dominance, this is the best selection for measuring the distributions of these important physical parameters. If instead there is a strong correlation between radio luminosity and $\nu^{\rm S}_{\rm peak}$, then the distribution of $\nu^{\rm S}_{\rm peak}$ should strongly depend on the radio flux limit.

X-ray selection favors high $\nu^{\rm S}_{\rm peak}$ (and consequently high $\nu^{\rm IC}_{\rm peak}$) sources, which are much brighter at X-ray frequencies than low $\nu^{\rm S}_{\rm peak}$ for the same radio flux. X-ray flux-limited samples are therefore much richer in high $\nu^{\rm S}_{\rm peak}$ BL Lacs (HBLs or

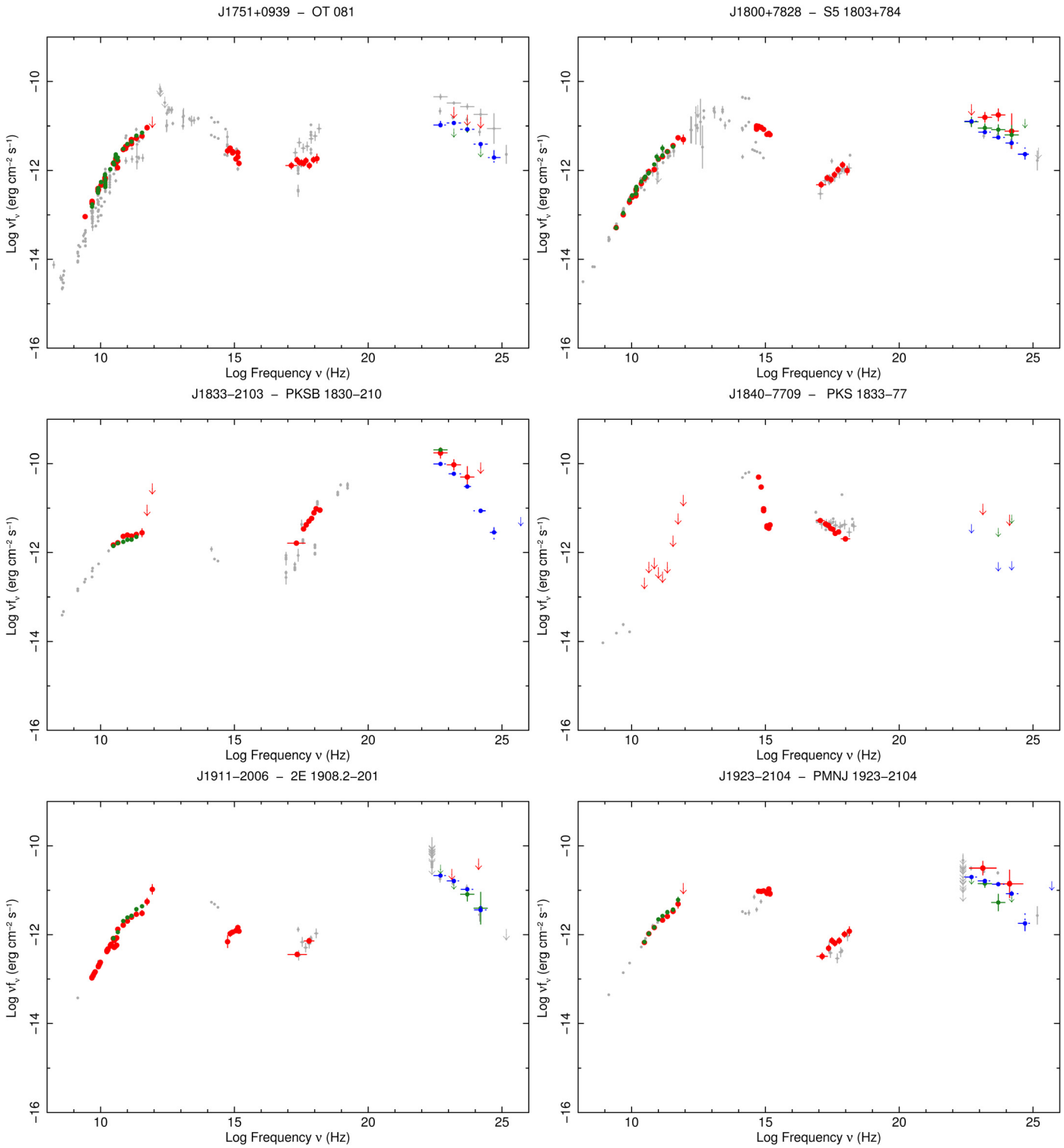

Fig. 37. The SED of OT 081 (J1751+0939, *top left*), S5 1803+784 (J1800+782, *top right*), PKSB 1830−210 (J1833−2103, *middle left*), PKS 1833−77 (J1840−7709, *middle right*), 2E 1908.2−201 (J1911−2006, *bottom left*), and PMNJ 1923−2104 (J1923−2104, *bottom right*). Simultaneous data are shown in red; quasi-simultaneous data, i.e. *Fermi* data integrated over 2 months, *Planck* ERCSC and non-simultaneous ground based observations are shown in green; *Fermi* data integrated over 27 months are shown in blue; literature or archival data are shown in light gray.

HSP sources) than radio-selected samples. This selection effect has been known since the first soft X-ray surveys became available.

Selection in the γ-ray band favors bright γ-ray objects and therefore highly Compton-dominated sources. *Fermi*-LAT TS-limited samples contain more sources with flat γ-ray spectral slopes or high $\nu^{\rm IC}_{\rm peak}$ sources. This explains the overabundance of HSP blazars (only BL Lacs) and high CD blazars (only FSRQs) in *Fermi*-LAT catalogs.

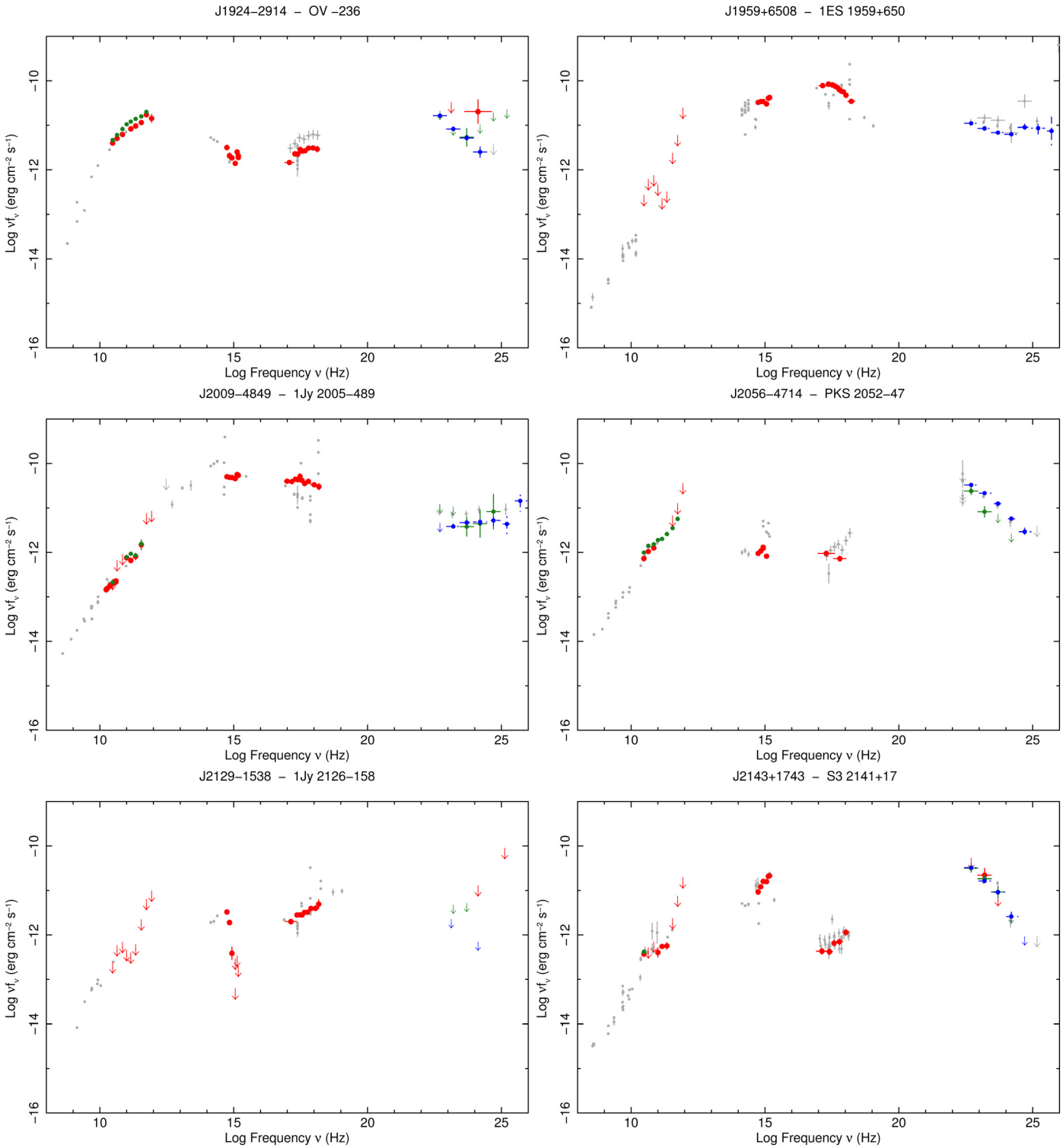

Fig. 38. The SED of OV−236 (J1924−2914, *top left*), 1ES 1959+650 (J1959+6508, *top right*), 1 Jy 2005−489 (J2009−4849, *middle left*), PKS 2052−47 (J2056−4714, *middle right*), 1 Jy 2126−158 (J2129−1538, *bottom left*), and S3 2141+17 (J2143+1743, *bottom right*). Simultaneous data are shown in red; quasi-simultaneous data, i.e. *Fermi* data integrated over 2 months, *Planck* ERCSC and non-simultaneous ground based observations are shown in green; *Fermi* data integrated over 27 months are shown in blue; literature or archival data are shown in light gray.

Acknowledgements. We thank the entire *Swift* team for the help and support and especially the Science Planners and Duty Scientists for their invaluable help and professional support with the planning and execution of a large number of ToOs. The *Planck* Collaboration acknowledges the support of: ESA; CNES and CNRS/INSU-IN2P3-INP (France); ASI, CNR, and INAF (Italy); NASA and DoE (USA); STFC and UKSA (UK); CSIC, MICINN and JA (Spain); Tekes, AoF and CSC (Finland); DLR and MPG (Germany); CSA (Canada); DTU Space (Denmark); SER/SSO (Switzerland); RCN (Norway); SFI (Ireland); FCT/MCTES (Portugal); and DEISA (EU). A full description of the *Planck* Collaboration and a list of its members, indicating which technical or scientific activities they have been involved in, can be found at http://www.rssd.esa.int/Planck. We thank the *Planck* team and in particular

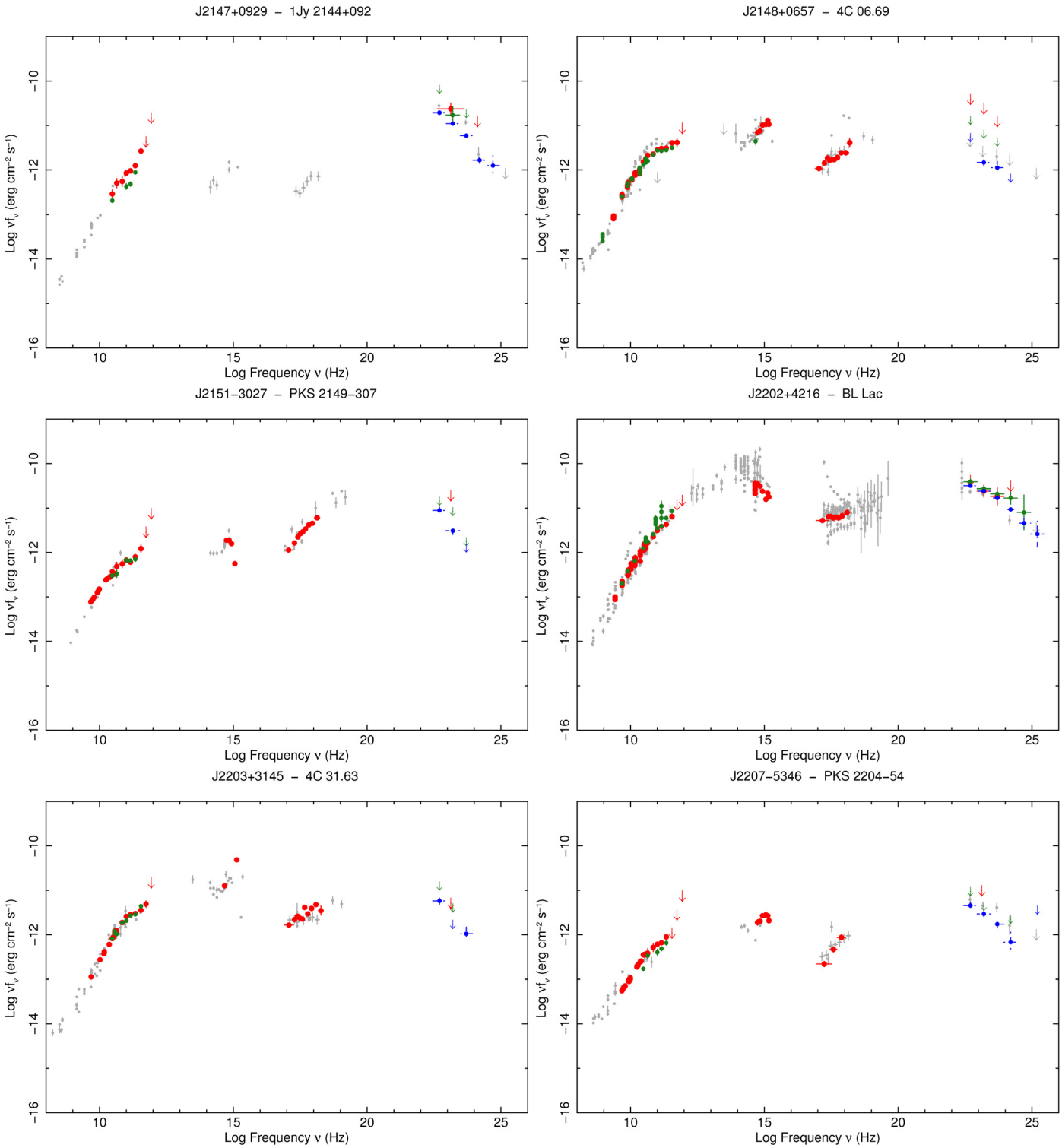

Fig. 39. The SED of 1Jy 2144+092 (J2147+0929, *top left*), 4C 06.69 (J2148+0657, *top right*), PKS 2149−307 (J2151−3027, *middle left*), BL Lac (J2202+4216, *middle right*), 4C 31.63 (J2203+3145, *botton left*), and PKS 2204−54 (J2207−5346, *botton right*). Simultaneous data are shown in red; quasi-simultaneous data, i.e. *Fermi* data integrated over 2 months, *Planck* ERCSC and non-simultaneous ground based observations are shown in green; *Fermi* data integrated over 27 months are shown in blue; literature or archival data are shown in light gray.

the members of the Data Processing Centers for their support in the reduction of LFI and HFI data carried out specifically for this work. The *Fermi*-LAT Collaboration acknowledges generous ongoing support from a number of agencies and institutes that have supported both the development and the operation of the LAT as well as scientific data analysis. These include the National Aeronautics and Space Administration and the Department of Energy in the United States, the Commissariat à l'Énergie Atomique and the Centre National de la Recherche Scientifique/Institut National de Physique Nucléaire et de Physique des Particules in France, the Agenzia Spaziale Italiana (ASI) and the Istituto Nazionale di Fisica Nucleare (INFN) in Italy, the Ministry of Education, Culture, Sports, Science and Technology (MEXT), High Energy Accelerator Research Organization (KEK) and Japan Aerospace Exploration Agency (JAXA) in Japan, and the K. A. Wallenberg Foundation, the Swedish Research Council and the Swedish National Space Board in Sweden. Additional

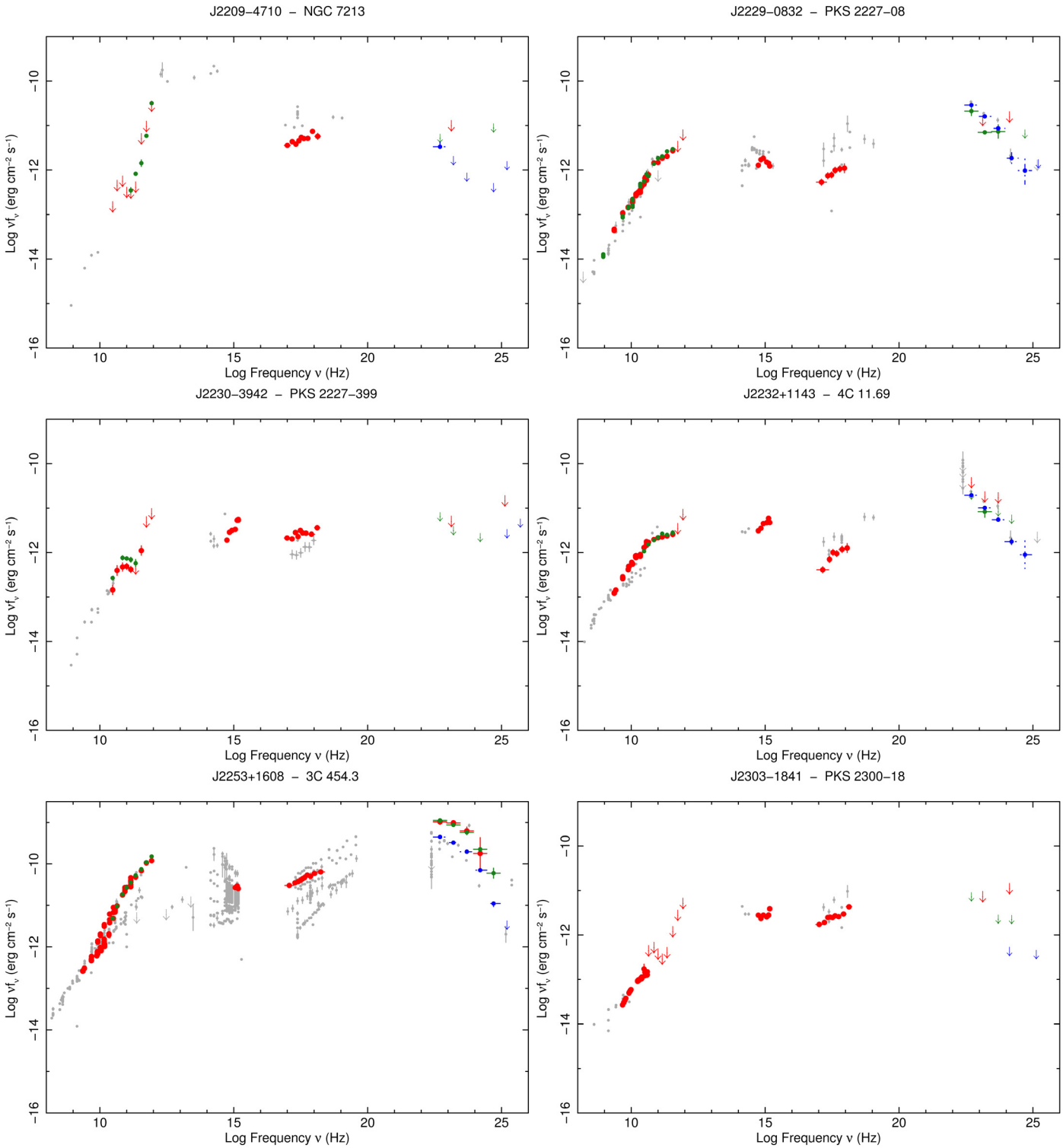

Fig. 40. The SED of NGC 7213 (J2209−4710, *top left*), PKS 2227−08 (J2229−0832, *top right*), PKS 2227−399 (J2230−3942, *middle left*), 4C 11.69 (J2232+1143, *middle right*), 3C 454.3 (J2253+1608, *bottom left*), and PKS 2300−18 (J2303−1841, *bottom right*). Simultaneous data are shown in red; quasi-simultaneous data, i.e. *Fermi* data integrated over 2 months, *Planck* ERCSC and non-simultaneous ground based observations are shown in green; *Fermi* data integrated over 27 months are shown in blue; literature or archival data are shown in light gray.

support for science analysis during the operations phase from the Istituto Nazionale di Astrofisica in Italy and the Centre National d'Études Spatiales in France is gratefully acknowledged. The Metsähovi team acknowledges the support from the Academy of Finland to our projects (numbers 212656, 210338, 121148, and others). This work was also supported by grants 127740 and 122352 of the Academy of Finland. UMRAO is supported by a series of grants from the NSF and NASA, and by the University of Michigan. This publication is partly based on data acquired with the Atacama Pathfinder Experiment (APEX). APEX is a collaboration between the Max-Planck-Institut für Radioastronomie, the European Southern Observatory, and the Onsala Space Observatory. This research is partly based on observations with the 100-m telescope of the MPIfR (Max-Planck-Institut für Radioastronomie) at Effelsberg, the IRAM 30-m telescope, and the Medicina (Noto) telescope operated by INAF – Istituto di Radioastronomia. J. Wu and X. Zhou are supported by the Chinese National Natural Science Foundation grants 10633020, 10778714, and 11073032, and by the National Basic Research Program of

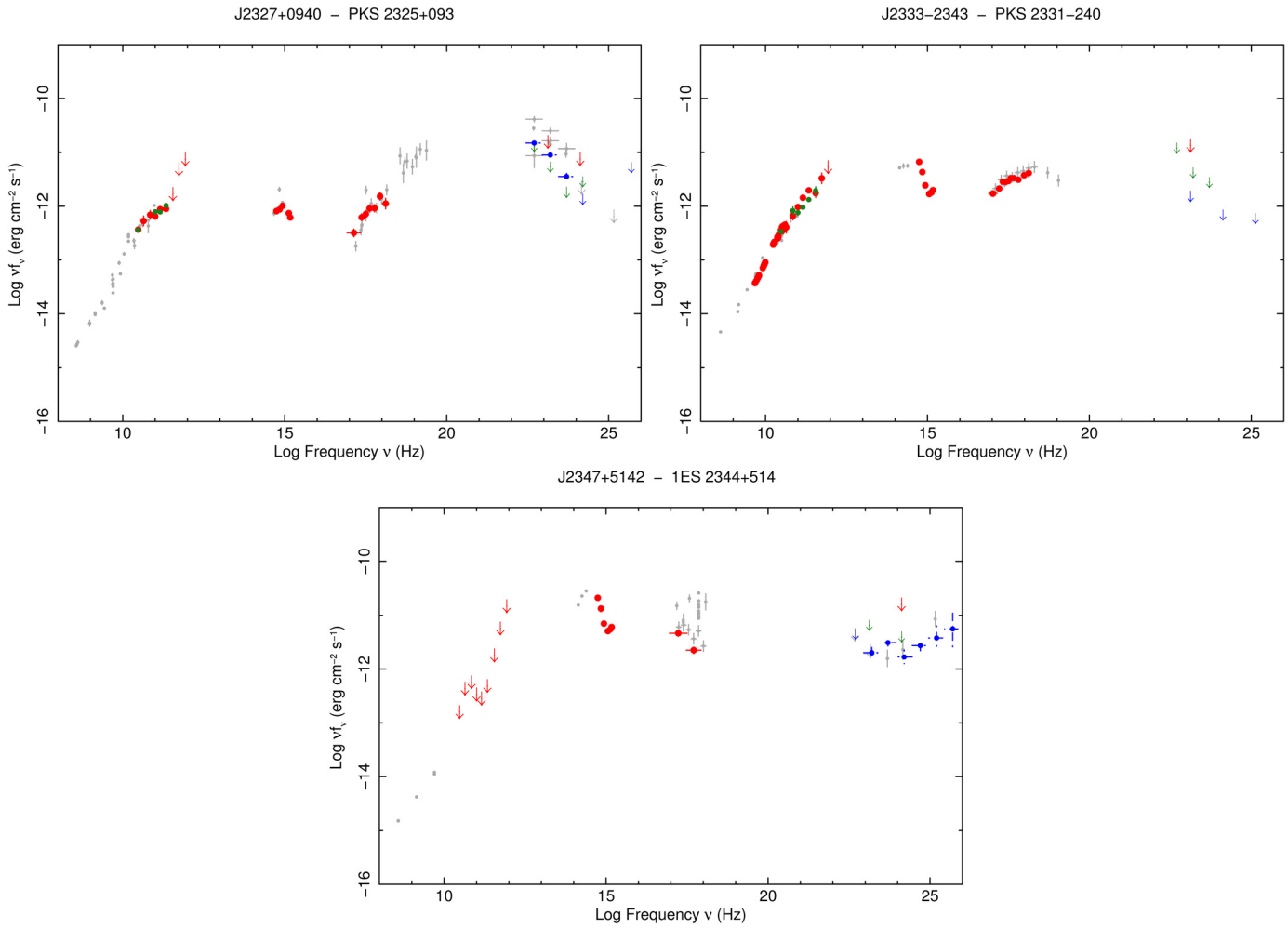

Fig. 41. The SED of PKS 2325+093 (J2327+0940, *top left*), PKS 2331−240 (J2333−2343, *top right*), and 1ES 2344+514 (J2347+5142, *middle*). Simultaneous data are shown in red; quasi-simultaneous data, i.e. *Fermi* data integrated over 2 months, *Planck* ERCSC and non-simultaneous ground based observations are shown in green; *Fermi* data integrated over 27 months are shown in blue; literature or archival data are shown in light gray.

China (973 Program) No. 2007CB815403. The OVRO 40-m monitoring program is supported in part by NASA grants NNX08AW31G and NNG06GG1G and NSF grant AST-0808050. O. G. King acknowledges the support of a Keck Institute for Space Studies Fellowship. W. Max-Moerbeck acknowledges support from a Fulbright-CONICYT scholarship. V. Pavlidou acknowledges support provided by NASA through Einstein Postdoctoral Fellowship grant number PF8-90060 awarded by the Chandra X-ray Center, which is operated by the Smithsonian Astrophysical Observatory for NASA under contract NAS8-03060. The Australia Telescope is funded by the Commonwealth of Australia for operation as a National Facility managed by CSIRO. This paper makes use of observations obtained at the Very Large Array (VLA) which is an instrument of the National Radio Astronomy Observatory (NRAO). The NRAO is a facility of the National Science Foundation operated under cooperative agreement by Associated Universities, Inc. We acknowledge the use of data and software facilities from the ASI Science Data Center (ASDC), managed by the Italian Space Agency (ASI). Part of this work is based on archival data and on bibliographic information obtained from the NASA/IPAC Extragalactic Database (NED) and from the Astrophysics Data System (ADS). We thank the anonymous referee for his/her useful and constructive comments.

References

Abdo, A. A., Ackermann, M., Ajello, M., et al. 2009a, ApJ, 699, 817
Abdo, A. A., Ackermann, M., Ajello, M., et al. 2009b, ApJ, 700, 597
Abdo, A. A., Ackermann, M., Agudo, I., et al. 2010a, ApJ, 716, 30
Abdo, A. A., Ackermann, M., Ajello, M., et al. 2010b, ApJ, 715, 429
Abdo, A. A., Ackermann, M., Ajello, M., et al. 2010c, ApJS, 188, 405
Abdo, A. A., Ackermann, M., Ajello, M., et al. 2010d, ApJS, 187, 460
Abdo, A. A., Ackermann, M., Ajello, M., et al. 2011, ApJ, 736, 131
Ackermann, M., Ajello, M., Allafort, A., et al. 2011, ApJ, 741, 30
Aharonian, F., Akhperjanian, A. G., Anton, G., et al. 2009, ApJ, 696, L150
Aliakberov, K. D., Mingaliev, M. G., Naugolnaya, M. N., et al. 1985, Astrofizicheskie Issledovaniia Izvestiya Spetsial'noj Astrofizicheskoj Observatorii, 19, 60
Aller, H. D., Aller, M. F., Latimer, G. E., & Hodge, P. E. 1985, ApJS, 59, 513
Angelakis, E., Fuhrmann, L., Marchili, N., Krichbaum, T. P., & Zensus, J. A. 2008, Mem. Astron. It., 79, 1042
Atwood, W. B., Abdo, A. A., Ackermann, M., et al. 2009, ApJ, 697, 1071
Avni, Y., & Tananbaum, H. 1986, ApJ, 305, 83
Baars, J. W. M., Genzel, R., Pauliny-Toth, I. I. K., & Witzel, A. 1977, A&A, 61, 99
Barthelmy, S. D., Barbier, L. M., Cummings, J. R., et al. 2005, Space Sci. Rev., 120, 143
Bennett, C. L., Hill, R. S., Hinshaw, G., et al. 2003, ApJS, 148, 97
Berlin, A., & Friedman, P. 1996, in 25th General Assembly of the International Union of Radio Science, 750
Bersanelli, M., Mandolesi, N., Butler, R. C., et al. 2010, A&A, 520, A4
Blandford, R. D., & Rees, M. J. 1978, in BL Lac Objects, ed. A. M. Wolfe, 328
Bonavera, L., Massardi, M., Bonaldi, A., et al. 2011, MNRAS, 1034
Burrows, D. N., Hill, J. E., Nousek, J. A., et al. 2005, Space Sci. Rev., 120, 165
Caccianiga, A., & Marchã, M. J. M. 2004, MNRAS, 348, 937
Capalbi, M., Perri, M., Saija, B., Tamburelli, F., & Angelini, L. 2005, http://heasarc.gsfc.nasa.gov/docs/swift/analysis/xrt_swguide_v1_2.eps
Colafrancesco, S., & Giommi, P. 2006, Chin. J. Astron. Astrophys. Suppl., 6, 010000

Condon, J. J., Cotton, W. D., Greisen, E. W., et al. 1998, AJ, 115, 1693
Corbett, E. A., Robinson, A., Axon, D. J., et al. 1996, MNRAS, 281, 737
Costamante, L., & Ghisellini, G. 2002, A&A, 384, 56
Cusumano, G., La Parola, V., Segreto, A., et al. 2010, A&A, 524, A64
Donnarumma, I., Vittorini, V., Vercellone, S., et al. 2009, ApJ, 691, L13
Fiorucci, M., & Tosti, G. 1996, A&AS, 116, 403
Fiorucci, M., Tosti, G., & Rizzi, N. 1998, PASP, 110, 105
Fitzpatrick, E. L. 1999, PASP, 111, 63
Fossati, G., Maraschi, L., Celotti, A., Comastri, A., & Ghisellini, G. 1998, MNRAS, 299, 433
Fuhrmann, L., Zensus, J. A., Krichbaum, T. P., Angelakis, E., & Readhead, A. C. S. 2007, in The First GLAST Symposium, ed. S. Ritz, P. Michelson, & C. A. Meegan, AIP Conf. Ser., 921, 249
Fuhrmann, L., Krichbaum, T. P., Witzel, A., et al. 2008, A&A, 490, 1019
Gehrels, N., Chincarini, G., Giommi, P., et al. 2004, ApJ, 611, 1005
Ghirlanda, G., Ghisellini, G., Tavecchio, F., & Foschini, L. 2010, MNRAS, 407, 791
Ghisellini, G., & Tavecchio, F. 2008, MNRAS, 387, 1669
Ghisellini, G., Celotti, A., Fossati, G., Maraschi, L., & Comastri, A. 1998, MNRAS, 301, 451
Ghisellini, G., Tavecchio, F., Foschini, L., & Ghirlanda, G. 2011, MNRAS, 627
Giommi, P., & Colafrancesco, S. 2004, A&A, 414, 7
Giommi, P., Ansari, S. G., & Micol, A. 1995, A&AS, 109, 267
Giommi, P., Menna, M. T., & Padovani, P. 1999, MNRAS, 310, 465
Giommi, P., Capalbi, M., Fiocchi, M., et al. 2002, in Blazar Astrophysics with BeppoSAX and Other Observatories, ed. P. Giommi, E. Massaro, & G. Palumbo, 63
Giommi, P., Piranomonte, S., Perri, M., & Padovani, P. 2005, A&A, 434, 385
Giommi, P., Blustin, A. J., Capalbi, M., et al. 2006, A&A, 456, 911
Giommi, P., Padovani, P., Polenta, G., et al. 2012, MNRAS, 420, 2899
Giroletti, M., Reimer, A., Fuhrmann, L., Pavlidou, V., & Richards, J. L. 2010 [arXiv:1001.5123]
Gold, B., Odegard, N., Weiland, J. L., et al. 2011, ApJS, 192, 15
González-Nuevo, J., Argüeso, F., López-Caniego, M., et al. 2006, MNRAS, 369, 1603
Górski, K. M., Hivon, E., Banday, A. J., et al. 2005, ApJ, 622, 759
Grupe, D., Komossa, S., Leighly, K. M., & Page, K. L. 2010, ApJS, 187, 64
Hartman, R. C., Bertsch, D. L., Bloom, S. D., et al. 1999, ApJS, 123, 79
Hill, J. E., Burrows, D. N., Nousek, J. A., et al. 2004, in SPIE Conf. Ser. 5165, ed. K. A. Flanagan, & O. H. W. Siegmund, 217
Isobe, T., Feigelson, E. D., & Nelson, P. I. 1986, ApJ, 306, 490
Kalberla, P. M. W., Burton, W. B., Hartmann, D., et al. 2005, A&A, 440, 775
Komatsu, E., Smith, K. M., Dunkley, J., et al. 2011, ApJS, 192, 18
Kotilainen, J. K., Falomo, R., & Scarpa, R. 1998, A&A, 332, 503
Kovalev, Y. Y., Aller, H. D., Aller, M. F., et al. 2009, ApJ, 696, L17
Lamarre, J., Puget, J., Ade, P. A. R., et al. 2010, A&A, 520, A9
Landt, H., Padovani, P., & Giommi, P. 2002, MNRAS, 336, 945
Landt, H., Padovani, P., Perlman, E. S., & Giommi, P. 2004, MNRAS, 351, 83
Lavalley, M., Isobe, T., & Feigelson, E. 1992, in Astronomical Data Analysis Software and Systems I, ed. D. M. Worrall, C. Biemesderfer, & J. Barnes, ASP Conf. Ser., 25, 245
Lawrence, C. R., Zucker, J. R., Readhead, A. C. S., et al. 1996, ApJS, 107, 541
Leahy, J. P., Bersanelli, M., D'Arcangelo, O., et al. 2010, A&A, 520, A8
León-Tavares, J., Valtaoja, E., Tornikoski, M., Lähteenmäki, A., & Nieppola, E. 2010, in Fermi meets Jansky: AGN in Radio and Gamma Rays, ed. T. Savolainen, E. Ros, R. W. Porcas, & J. A. Zensus, 93
León-Tavares, J., Valtaoja, E., Chavushyan, V. H., et al. 2011a, MNRAS, 411, 1127
León-Tavares, J., Valtaoja, E., Tornikoski, M., Lähteenmäki, A., & Nieppola, E. 2011b, A&A, 532, A146
Linford, J. D., Taylor, G. B., Romani, R. W., et al. 2011, ApJ, 726, 16
López-Caniego, M., Herranz, D., González-Nuevo, J., et al. 2006, MNRAS, 370, 2047
López-Caniego, M., González-Nuevo, J., Herranz, D., et al. 2007, ApJS, 170, 108
Mahony, E. K., Sadler, E. M., Murphy, T., et al. 2010, ApJ, 718, 587
Mandolesi, N., Bersanelli, M., Butler, R. C., et al. 2010, A&A, 520, A3
Mannucci, F., Basile, F., Poggianti, B. M., et al. 2001, MNRAS, 326, 745
Marcha, M. J. M., Browne, I. W. A., Impey, C. D., & Smith, P. S. 1996, MNRAS, 281, 425
Massardi, M., López-Caniego, M., González-Nuevo, J., et al. 2009, MNRAS, 392, 733
Massardi, M., Bonaldi, A., Bonavera, L., et al. 2011a, MNRAS, 415, 1597
Massardi, M., Ekers, R. D., Murphy, T., et al. 2011b, MNRAS, 412, 318
Massaro, E., Perri, M., Giommi, P., & Nesci, R. 2004, A&A, 413, 489
Massaro, E., Giommi, P., Leto, C., et al. 2009, A&A, 495, 691
Massaro, E., Giommi, P., Leto, C., et al. 2010 [arXiv:1006.0922]
Mattox, J. R., Bertsch, D. L., Chiang, J., et al. 1996, ApJ, 461, 396
Mauch, T., Murphy, T., Buttery, H. J., et al. 2003, MNRAS, 342, 1117
Mennella, A., Bersanelli, M., Butler, R. C., et al. 2011, A&A, 536, A3
Meyer, E. T., Fossati, G., Georganopoulos, M., & Lister, M. L. 2011, ApJ, 740, 98
Moretti, A., Campana, S., Mineo, T., et al. 2005, in SPIE Conf. Ser. 5898, ed. O. H. W. Siegmund, 360
Nieppola, E., Tornikoski, M., & Valtaoja, E. 2006, A&A, 445, 441
Nilsson, K., Pursimo, T., Heidt, J., et al. 2003, A&A, 400, 95
Nilsson, K., Pasanen, M., Takalo, L. O., et al. 2007, A&A, 475, 199
Padovani, P. 2007, Ap&SS, 309, 63
Padovani, P., & Giommi, P. 1995, ApJ, 444, 567
Padovani, P., Perlman, E. S., Landt, H., Giommi, P., & Perri, M. 2003, ApJ, 588, 128
Padovani, P., Giommi, P., Ábrahám, P., Csizmadia, S., & Moór, A. 2006, A&A, 456, 131
Parijskij, Y. N. 1993, IEEE Antennas Propagation Magazine, 35, 7
Peel, M. W., Gawroński, M. P., Battye, R. A., et al. 2011, MNRAS, 410, 2690
Perlman, E., Addison, B., Georganopoulos, M., Wingert, B., & Graff, P. 2008, in Blazar Variability across the Electromagnetic Spectrum, Proc. Science, BLAZARS2008, 009
Pian, E., Urry, C. M., Maraschi, L., et al. 1999, ApJ, 521, 112
Planck Collaboration 2011a, A&A, 536, A1
Planck Collaboration 2011b, A&A, 536, A2
Planck Collaboration 2011c, A&A, 536, A7
Planck Collaboration 2011d, A&A, 536, A13
Planck Collaboration 2011e, A&A, 536, A15
Planck HFI Core Team 2011a, A&A, 536, A4
Planck HFI Core Team 2011b, A&A, 536, A6
Poole, T. S., Breeveld, A. A., Page, M. J., et al. 2008, MNRAS, 383, 627
Procopio, P., Massardi, M., Righini, S., et al. 2011, MNRAS, 417, 1123
Raiteri, C. M., Villata, M., Lanteri, L., Cavallone, M., & Sobrito, G. 1998, A&AS, 130, 495
Raiteri, C. M., Villata, M., Capetti, A., et al. 2009, A&A, 507, 769
Richards, J. L., Max-Moerbeck, W., Pavlidou, V., et al. 2011, ApJS, 194, 29
Roming, P. W. A., Kennedy, T. E., Mason, K. O., et al. 2005, Space Sci. Rev., 120, 95
Rosset, C., Tristram, M., Ponthieu, N., et al. 2010, A&A, 520, A13
Sambruna, R. M., Maraschi, L., & Urry, C. M. 1996, ApJ, 463, 444
Scarpa, R., Urry, C. M., Falomo, R., Pesce, J. E., & Treves, A. 2000, ApJ, 532, 740
Schlegel, D. J., Finkbeiner, D. P., & Davis, M. 1998, ApJ, 500, 525
Shaw, M. S., Romani, R. W., Healey, S. E., et al. 2009, ApJ, 704, 477
Shaw, M. S., Romani, R. W., Cotter, G., et al. 2010, in BAAS, 42, AAS Meeting Abstracts, 215, 434.12
Stickel, M., Padovani, P., Urry, C. M., Fried, J. W., & Kuehr, H. 1991, ApJ, 374, 431
Stocke, J. T., Morris, S. L., Gioia, I. M., et al. 1991, ApJS, 76, 813
Stocke, J. T., Danforth, C. W., & Perlman, E. S. 2011, ApJ, 732, 113
Stratta, G., Capalbi, M., Giommi, P., et al. 2011 [arXiv:1103.0749]
Tauber, J. A., Mandolesi, N., Puget, J., et al. 2010, A&A, 520, A1
Teräsranta, H., Tornikoski, M., Mujunen, A., et al. 1998, A&AS, 132, 305
Toffolatti, L., Argueso Gomez, F., de Zotti, G., et al. 1998, MNRAS, 297, 117
Tramacere, A., Giommi, P., Perri, M., Verrecchia, F., & Tosti, G. 2009, A&A, 501, 879
Tucci, M., Toffolatti, L., de Zotti, G., & Martínez-González, E. 2011, A&A, 533, A57
Urry, C. M., & Padovani, P. 1995, PASP, 107, 803
Urry, C. M., Scarpa, R., O'Dowd, M., et al. 2000, ApJ, 532, 816
Vagnetti, F., Turriziani, S., Trevese, D., & Antonucci, M. 2010, A&A, 519, A17
Vanden Berk, D. E., Richards, G. T., Bauer, A., et al. 2001, AJ, 122, 549
Vercellone, S., Chen, A. W., Vittorini, V., et al. 2009, ApJ, 690, 1018
Verkhodanov, O. V. 1997, in Astronomical Data Analysis Software and Systems VI, ed. G. Hunt, & H. Payne, ASP Conf. Ser., 125, 46
Vermeulen, R. C., Ogle, P. M., Tran, H. D., et al. 1995, ApJ, 452, L5
Villata, M., Raiteri, C. M., Lanteri, L., Sobrito, G., & Cavallone, M. 1998, A&AS, 130, 305
Voges, W., Aschenbach, B., Boller, T., et al. 1999, A&A, 349, 389
von Montigny, C., Bertsch, D. L., Chiang, J., et al. 1995, ApJ, 440, 525
Weekes, T. C. 2008, in AIP Conf. Ser. 1085, ed. F. A. Aharonian, W. Hofmann, & F. Rieger, 3
Wright, E. L., Chen, X., Odegard, N., et al. 2009, ApJS, 180, 283
York, D. G., Adelman, J., Anderson, Jr., J. E., et al. 2000, AJ, 120, 1579
Zacchei, A., Maino, D., Baccigalupi, C., et al. 2011, A&A, 536, A5

[1] Aalto University Metsähovi Radio Observatory, Metsähovintie 114, 02540 Kylmälä, Finland
[2] Agenzia Spaziale Italiana Science Data Center, c/o ESRIN, via Galileo Galilei, Frascati, Italy
e-mail: giommi@asdc.asi.it
[3] Agenzia Spaziale Italiana, Viale Liegi 26, Roma, Italy
[4] Astronomy Department, University of Michigan, 830 Dennison Building, 500 Church Street, Ann Arbor, Michigan 48109-1042, USA
[5] Astroparticle Physics Laboratory, NASA/Goddard Space Flight Center, Greenbelt, MD 20771, USA
[6] Astrophysics Group, Cavendish Laboratory, University of Cambridge, J J Thomson Avenue, Cambridge CB3 0HE, UK
[7] Australia Telescope National Facility, CSIRO, PO Box 76, Epping, NSW 1710, Australia
[8] California Institute of Technology, Pasadena, California, USA
[9] Departamento de Física, Universidad de Oviedo, Avda. Calvo Sotelo s/n, Oviedo, Spain
[10] Department of Astronomy and Astrophysics, Pennsylvania State University, 525 Davey Lab, University Park, PA 16802, USA
[11] Department of Physics and Astronomy, Tufts University, Medford, MA 02155, USA
[12] Department of Physics, Gustaf Hällströmin katu 2a, University of Helsinki, Helsinki, Finland
[13] Dipartimento di Fisica G. Galilei, Università degli Studi di Padova, via Marzolo 8, 35131 Padova, Italy
[14] Dipartimento di Fisica M. Merlin dell'Università e del Politecnico di Bari, 70126 Bari, Italy
[15] Dipartimento di Fisica, Università degli Studi di Perugia, 06123 Perugia, Italy
[16] Dipartimento di Fisica, Università di Ferrara, via Saragat 1, 44122 Ferrara, Italy
[17] Finnish Centre for Astronomy with ESO (FINCA), University of Turku, Väisäläntie 20, 21500 Piikkiö, Finland
[18] Haverford College Astronomy Department, 370 Lancaster Avenue, Haverford, Pennsylvania, USA
[19] Helsinki Institute of Physics, Gustaf Hällströmin katu 2, University of Helsinki, Helsinki, Finland
[20] INAF – Osservatorio Astrofisico di Catania, via S. Sofia 78, Catania, Italy
[21] INAF – Osservatorio Astronomico di Brera, via E. Bianchi 46, 23807, Merate (LC), Italy
[22] INAF – Osservatorio Astronomico di Padova, Vicolo dell'Osservatorio 5, Padova, Italy
[23] INAF – Osservatorio Astronomico di Roma, via di Frascati 33, Monte Porzio Catone, Italy
[24] INAF – Osservatorio Astronomico di Trieste, via G.B. Tiepolo 11, Trieste, Italy
[25] INAF Istituto di Radioastronomia, via P. Gobetti 101, 40129 Bologna, Italy
[26] INAF/IASF Bologna, via Gobetti 101, Bologna, Italy
[27] INAF/IASF, Sezione di Palermo, via Ugo La Malfa 153, 90146 Palermo, Italy
[28] ISDC Data Centre for Astrophysics, University of Geneva, Ch. d'Ecogia 16, Versoix, Switzerland
[29] Infrared Processing and Analysis Center, California Institute of Technology, Pasadena, CA 91125, USA
[30] Institut de Radioastronomie Millimétrique (IRAM), Avenida Divina Pastora 7, Local 20, 18012 Granada, Spain
[31] Institute für Astro- und Teilchenphysik and Institut für Theoretische Physik, Leopold-Franzens-Universität Innsbruck, 6020 Innsbruck, Austria
[32] Instituto de Física de Cantabria (CSIC-Universidad de Cantabria), Avda. de los Castros s/n, Santander, Spain
[33] Istituto Nazionale di Fisica Nucleare, Sezione di Bari, 70126 Bari, Italy
[34] Istituto Nazionale di Fisica Nucleare, Sezione di Padova, 35131 Padova, Italy
[35] Istituto Nazionale di Fisica Nucleare, Sezione di Perugia, 06123 Perugia, Italy
[36] Jet Propulsion Laboratory, California Institute of Technology, 4800 Oak Grove Drive, Pasadena, California, USA
[37] Jodrell Bank Centre for Astrophysics, Alan Turing Building, School of Physics and Astronomy, The University of Manchester, Oxford Road, Manchester, M13 9PL, UK
[38] Kavli Institute for Cosmology Cambridge, Madingley Road, Cambridge, CB3 0HA, UK
[39] Key Laboratory of Optical Astronomy, National Astronomical Observatories, Chinese Academy of Sciences, 20A Datun Road, Chaoyang District, 100012 Beijing, PR China
[40] Max-Planck-Institut für Astrophysik, Karl-Schwarzschild-Str. 1, 85741 Garching, Germany
[41] Max-Planck-Institut für Radioastronomie, Auf dem Hügel 69, 53121 Bonn, Germany
[42] Owens Valley Radio Observatory, Mail code 249-17, California Institute of Technology, 1200 E California Blvd, Pasadena, CA 91125, USA
[43] SISSA, Astrophysics Sector, via Bonomea 265, 34136, Trieste, Italy
[44] Special Astrophysical Observatory, Russian Academy of Sciences, Nizhnij Arkhyz, Zelenchukskiy region, Karachai-Cherkessian Republic, 369167, Russia
[45] Tuorla Observatory, Department of Physics and Astronomy, University of Turku, Väisäläntie 20, 21500 Piikkiö, Finland
[46] Università degli studi di Milano-Bicocca, Dipartimento di Fisica, Piazza delle Scienze 3, 20126 Milano, Italy
[47] W. W. Hansen Experimental Physics Laboratory, Kavli Institute for Particle Astrophysics and Cosmology, Department of Physics and SLAC National Accelerator Laboratory, Stanford University, Stanford, CA 94305, USA